

Design, Simulation, and Fabrication of a Lightweight Magneto Rheological Damper

By

Soroush Sefidkar-Dezfouli

B.Sc., Azad University, 2009

Thesis Submitted in Partial Fulfilment
of the Requirements for the Degree of
Master of Applied Science

In the
School of Mechatronic Systems Engineering
Faculty of Applied Sciences

©Soroush Sefidkar-Dezfouli 2014

SIMON FRASER UNIVERSITY

Spring 2014

All rights reserved.

However, in accordance with the *Copyright Act of Canada*, this work may be reproduced, without authorization, under the conditions for "Fair Dealing." Therefore, limited reproduction of this work for the purposes of private study, research, criticism, review and news reporting is likely to be in accordance with the law, particularly if cited appropriately.

Approval

Name: Soroush Sefidkar-Dezfouli
Degree: Master of Applied Science (Engineering)
Title of Thesis: *Design, Simulation, and Fabrication of a Lightweight Magneto Rheological Damper*
Examining Committee: Chair: Dr.Gary Wang
Professor

Dr.Mehrdad Moallem
Senior Supervisor
Professor

Dr. Siamak Arzanpour
Supervisor
Associate Professor

Dr. Shahram Payandeh
Internal examiner
Professor

Date Defended/Approved: March 5, 2014

Partial Copyright License



The author, whose copyright is declared on the title page of this work, has granted to Simon Fraser University the non-exclusive, royalty-free right to include a digital copy of this thesis, project or extended essay[s] and associated supplemental files (“Work”) (title[s] below) in Summit, the Institutional Research Repository at SFU. SFU may also make copies of the Work for purposes of a scholarly or research nature; for users of the SFU Library; or in response to a request from another library, or educational institution, on SFU’s own behalf or for one of its users. Distribution may be in any form.

The author has further agreed that SFU may keep more than one copy of the Work for purposes of back-up and security; and that SFU may, without changing the content, translate, if technically possible, the Work to any medium or format for the purpose of preserving the Work and facilitating the exercise of SFU’s rights under this licence.

It is understood that copying, publication, or public performance of the Work for commercial purposes shall not be allowed without the author’s written permission.

While granting the above uses to SFU, the author retains copyright ownership and moral rights in the Work, and may deal with the copyright in the Work in any way consistent with the terms of this licence, including the right to change the Work for subsequent purposes, including editing and publishing the Work in whole or in part, and licensing the content to other parties as the author may desire.

The author represents and warrants that he/she has the right to grant the rights contained in this licence and that the Work does not, to the best of the author’s knowledge, infringe upon anyone’s copyright. The author has obtained written copyright permission, where required, for the use of any third-party copyrighted material contained in the Work. The author represents and warrants that the Work is his/her own original work and that he/she has not previously assigned or relinquished the rights conferred in this licence.

Simon Fraser University Library
Burnaby, British Columbia, Canada

revised Fall 2013

Abstract

Mountain biking has significantly evolved recently, thanks to utilizing cutting-edge technologies in mountain bicycle design and fabrication. In this research we study development of a semi-active suspension system using magneto-rheological (MR) fluid dampers instead of conventional oil based shocks. MR dampers are devices with magnetic field dependent damping characteristics. Low power consumption, high controllability, quick response, and high durability are among the major features of MR dampers.

In this work we first investigate the damping characteristics of MR dampers to find out if characteristics comparable to the conventional shocks used in mountain bikes can be achieved. To this end, experimental tests were performed on an off-the-shelf MR damper. The results indicate that damping characteristics similar to the ones used in mountain bikes can in fact be achieved using MR technology. However, requirements such as small weight and wide dynamic range have to be addressed in designing a MR damper for mountain bikes. These considerations are studied in this thesis by formulating a simple design followed by a constrained optimization problem and designing the damper accordingly. Utilizing Finite element modeling and simulation tools are further utilized to fine tune and optimize the design. A prototype MR damper is fabricated after the above design steps are carried out.

Keywords: Magneto-rheological fluid; MR damper; mountain bicycle shocks; fabrication; optimization; simulation

Dedication

To my family; without their unconditional support and inspiration, none of this could be possible.

Acknowledgements

I want to thank my supervisor, Dr.Mehrdad Moallem, for his kind guidance and encouragement, throughout my studies at SFU; he was truly supportive and understanding. Also, I want to thank my co-supervisor, Dr.Siamak Arzanpour, for his valuable guidance and timely directions. I want to thank Dr.Shahram payandeh for agreeing to be my examiner, and Dr.Gary Wang for both his presence as chairman on my MSc defence, and his enthusiasm in teaching optimization course.I want to acknowledge all other personals at SFU that helped me during my studies.

Additionally, I want to acknowledge NSERC Canada for their support, and thank Rocky Mountain Bicycles for their interest and investment in project, as well as, their support and cooperation.

I also want to thank my former college Ehsan Asadi, whom I start working on my research with, for familiarizing me with this subject. Similarly, I want to thank my college Mehdi Naseri, for his assistance in final stages of project. Additionally, I want to thank my friends at SFU, who helped, and supported me in process, and made my studies more joyful; Pouya Amid, Amir Maravandi, Ashkan Mirnabavi, Farshad Roudposhti, Yaser Mohammadian, Ali ShagerdMootab, Farzad Hamidi, Rasoul Milasi, Sepehr Attarchi, and others.

Finally, I want to specially thank my family Sedigheh Rahmansetayesh, Alireza Sefidkar, and Saman Sefidkar; for their unconditional love and support in all stages of my life. I am forever grateful.

Table of Contents

Approval.....	ii
Partial Copyright License	iii
Abstract.....	iv
Dedication.....	v
Acknowledgements.....	vi
Table of Contents.....	vii
List of Tables.....	x
List of Figures.....	xi

Chapter 1. Introduction.....	1
1.1. Mountain bicycle rear suspension system	2
1.1.1. Conventional shocks.....	3
1.1.2. Semi-active shocks.....	4
1.2. Research motivation and contributions.....	5
1.3. Fabrication and assembly of a prototype MR damper Thesis outline	6

Chapter 2. Review of MR Fluid and MR Damper Mechanism	7
2.1. MR Fluid.....	7
2.1.1. MR Fluid components and composition.....	8
2.1.2. MR fluid magnetic behaviour.....	10
Magnetic material.....	10
Concept of electromagnetism.....	13
MR Fluid magnetic properties	14
2.1.3. Rheology of MR fluid.....	15
Basics of rheology.....	15
Rheological properties of MR fluid	18
MR fluid models	20
Bingham plastic model.....	21
Herschel-Bulkley plastic model	22
2.1.4. MR Fluid modes and applications	23
Valve mode.....	23
Shear mode	25
MR Brakes.....	26
Squeeze mode.....	27
MR fluid elastomer mount	28
2.2. MR Damper.....	29
2.2.1. MR damper components and designs.....	29
Cylinder structures	30
Monotube damper structure	30
Twin tube structure.....	31
Double-ended structure.....	32
Valve structure.....	33
Single coil valves.....	34
Multi coil valves	36
Perpendicular coil axis valve.....	36

Valve with both annular and radial flow channel	37
Fail-safe MR dampers	38
2.2.2. MR damper modeling	40
Quasi-static models	40
Axisymmetric models	41
Parallel plate model	42
Dynamic models	44
Parametric dynamic model	44
Bingham dynamic model	45
Bouc-wen and Spencer dynamic models	45
Non-parametric dynamic model	47
2.3. Conclusion	48
Chapter 3. Experimental comparison of MR and conventional dampers	49
3.1. Feasibility Testing	49
3.1.1. Test mechanism	50
3.1.2. Damper selection	52
3.1.3. Test procedure and guidelines	53
General Guidelines for testing all the dampers:	54
Guidelines for testing conventional dampers (D1, D2, and D3):	54
Guidelines for testing the MR damper	54
3.2. Analysis of results	56
3.2.1. Data acquisition and Performance evaluation	57
Effect of input stimuli amplitude on performance	57
Input stimuli frequency effect on performance	58
Rebound circuit and compression circuit effect on performance	59
Effect of the Input current on performance	61
Effect of the parallel coil spring on performance	61
3.2.2. Proof of feasibility	63
3.3. Conclusion	64
Chapter 4. Design, Simulation, and Optimization	65
4.1. Study of two commercial dampers	65
Fox Van R Downhill Shock absorber	65
Lord 8041 MR Damper	69
4.2. Optimal design of an MR damper	73
4.2.1. Material selection	73
4.2.2. Magnetic field analysis of MR damper	76
4.2.3. Finite element simulation	77
Approach and Assumptions	78
Output data	82
4.2.4. Optimization using finite element analysis	82
Optimization objectives	84
Design parameters and constraint selection	87
Genetic algorithm for optimum design	89
Results analysis	90
4.2.5. Coil wire selection	93

4.1. Conclusion	97
Chapter 5. Fabrication and testing of a prototype MR damper	98
5.1. Materials, sealing, CAD design, and prototyping	98
5.2. Experimental performance testing	103
5.2.1. Effect of displacement amplitude.....	103
5.2.2. Effect of displacement frequency	104
5.2.3. Effect of input current.....	105
5.2.4. Comparison of parallel plate model and experimental data	105
5.2.5. Comparison of Lord MR damper and prototype MR damper	106
5.3. Conclusion	107
Chapter 6. Summary and future works	108
6.1. Research summary	108
6.2. Recommendations for future work	110
References 112	
Appendix A. Experimental test results for four tested shocks	119
Appendix B SolidWorks drawings of prototype.	122
Appendix C MRF132DG Datasheet.....	124

List of Tables

Table 3.1 All performed tests, over a wide range of input displacement profiles.	55
Table 4.1 Material available for Cylinder body.	74
Table 4.2 Commercial MR fluid available.	75
Table 4.3 Design parameters of Lord MR damper.	82
Table 4.4 Constants and intermediate variables.	88
Table 4.5 Design variables and parameters constraints.	89
Table 4.6 Optimization results for design variables and main properties.	91
Table 4.7 AWG wire properties and calculated performance.	96
Table 5.1 List of components utilized in prototype.	99
Table 5.2 Parameter comparison of Lord MR damper and prototype.	106

List of Figures

Figure 2.1 (a) MRF in absence of a magnetic field, (b) MRF particle alignment under influence of magnetic field.	7
Figure 2.2 Powder metallurgy process main stages.	9
Figure 2.3 Typical hysteresis loop for a ferromagnetic material.	11
Figure 2.4 Comparison of soft and hard magnetic material hysteresis curve.	12
Figure 2.5 (a) Solenoid coil wounded around the air (b) Solenoid wounded around a soft magnetic core.	13
Figure 2.6 B-H curve of MRF132DG MR fluid by Lord Corp.	15
Figure 2.7 Shear force applied to a surface[30].	16
Figure 2.8 Rheological behavior of various viscous materials.	17
Figure 2.9 MRF132DG Lord Corp MR fluid (a) Shear stress Vs Shear rate (b) Yield stress Vs Magnetic field intensity.	19
Figure 2.10 (a) stress-strain of MR fluid (b) Bingham model of MR fluid.	21
Figure 2.11 Herschel-Bulkley model of MR fluid.	22
Figure 2.12 (a) concept of valve mode (b) Bingham velocity profile of MR fluid in valve mode [19](c) flow through a parallel duct [48].	24
Figure 2.13 (a) concept of direct shear mode [19] (b) Bingham velocity profile of MR fluid in shear mode [15].	25
Figure 2.14 Major MR-brake designs: (a) drum (b) inverted drum (c) T-shaped rotor(d) disk (e) multiple disks.	27
Figure 2.15 Concept of squeeze mode[19].	27
Figure 2.16 (a) Rubber puck shape vibration mount (b) new polyurethane membrane for vibration mount application[44].	29
Figure 2.17 Mono tube cylinder[8].	31
Figure 2.18 (a) conceptual structure of twin-tube[51] (b)foot valve sectional view [8] (c) section view of a twin tube damper[8].	32
Figure 2.19 Double-end MR damper[8].	33

Figure 2.20 (a) Typical control valve of MR damper[48] (b) MR damper with external stationary coil[17].....	35
Figure 2.21 (a) Single coil valve mode MR damper[88] (b) Single coil valve in shear mode (c) Single coil valve in valve mode.....	35
Figure 2.22 (a) Multi coil MR damper [42] (b) schematics of double coil MR damper.....	36
Figure 2.23 (a) Components of perpendicular coil axis configuration (b) core structure (c) Magnetic field path in perpendicular coil axis configuration [52].....	37
Figure 2.24 (a) Detailed schematics of valve with both annular and radial flow channel [59] (b) Flow path and magnetic field of damper [48].....	38
Figure 2.25 (a) Implementation of permanent magnets in poles of MR damper only(b) magnetic core structure with permanent magnet (c) fail-safe hybrid damper with permanent magnets inside core and poles [55].	39
Figure 2.26 Schematics of a valve mode MR damper piston with geometrical parameters.....	44
Figure 2.27 (a) Bingham model (b) Bingham body model (c)Bingham and Bingham body model Force-velocity curve.....	46
Figure 2.28 (a) Bouc-wen model for MR damper (b) Spencer model for MR damper [75].....	47
Figure3.1 (a) Hydraulic shaker, (b) Force transducer, (c) Digital controller.....	50
Figure 3.2 Fabricated connector to attach dampers to the hydraulic shaker.....	51
Figure 3.3 Test mechanism components, while testing MR damper in parallel with coil spring.	51
Figure 3.4 Tested Shocks: (a) Fox Van R (D1), (b) Fox Van RC (D2), (c) Cane Creek Double Barrel (D3), (d) Lord Corporation MR damper.....	53
Figure 3.5 Experimental results (a) the force-displacement curve for a conventional bicycle damper (b) the force-velocity curve for a conventional bicycle damper.	57
Figure 3.6 Force vs. Displacement in High Rebound (HR)- Low Compression (LR) with 2Hz frequency and different amplitudes: (a) D1 (b) D2 (c) D3 (d) MR damper.	58

Figure 3.7 (a) F-V curve of D3 damper for different frequencies at 23mm amplitude, (b) F-V curve of MR damper for different frequencies at 23mm amplitude.....	59
Figure 3.8 Comparison of the effect of knob adjustment: (a) F-D of D1 for LR and HR, (b) F-V of D1 for LR and HR, (c) F-D of D2 for LR and HR, (d) F-D of D2 for LR and HR, (e) F-D of D3 for LR and HR ,(f) F-D of D3 for LR and HR.....	60
Figure 3.9 MR damper characteristics for different input currents (6Hz, 23mm): (a) F-D curve, (b) F-V curve.	61
Figure 3.10 Results for MR with spring (current: 0.8 A; amplitude: 08 and 13 mm; frequency: 2 and 4 Hz): (a) F-D characteristic, (b) F-V characteristic. Comparison of MR characteristic with and without spring (current: 0.8 A; amplitude: 13 mm; frequency: 4 Hz): (c) F-D curve, (d) F-V curve.	62
Figure 3.11 Comparison of results for MR and D3 dampers (Without Spring; amplitude: 13 mm; frequency: 4 Hz): (a) F-D curve, (b) F-V curve.....	63
Figure 4.1 Detailed dissection of Fox Van R shock absorber.....	66
Figure 4.2 (a) Rod and rebound adjustment mechanism, (b) cylinder cap and bottom out bumper, (c) Piston and shim stacks, (d) compression and rebound valves, (e) cylinder and preload ring, (f) Coupler and compression adjustment knob, (g) gas chamber cylinder and pressure valve, (h) Floating piston.	68
Figure 4.3 Detailed dissection of Fox Van R shock absorber.....	70
Figure 4.4 Spectrometry result for cylinder material (peaks showing Fe, O, C).....	71
Figure 4.5 (a) Rod handle with bushing and wires, (b) Piston housing, wear strip, and guides, (c) Coil, (d) Magnetic pole and hallow core with coil slot, (e) Rubber diaphragm and cap, (f) MR fluid flow gap filled with MR. fluid.	72
Figure 4.6 MR valve magnetic links and magnetic path.....	77
Figure 4.7 (a) SolidWorks CAD model of the Lord 8041 MR damper, (b) Imported 3D model using LiveLink, (c) 2D model in Comsol.	78
Figure 4.8 MR damper selected design with DVs.	79
Figure 4.9 (a) HB curve of Comsol materials library, (b) MR fluid HB curve from Comsol obtained from datasheet.....	80
Figure 4.11 (a) 3D simulation to study x density for Lord MR damper, (b) 2D simulation of flux density for Lord MR damper.....	81

Figure 4.10 Customised meshing used for FEA simulation.....	81
Figure 4.12 Optimization procedure flow chart.	83
Figure 4.13 Optimization design variables and dependent parameters.	87
Figure 4.14 (a) Flux density distribution for initial values, (b) Flux density distribution for optimized values.	92
Figure 4.15 (a) The maximum damping force in optimization generations, (a) bottom weight values in different iterations (b) top Volume of MR used in damper in different generations (b) bottom, dynamic ratio in generations.	93
Figure 5.1 Detailed SolidWorks CAD design of proposed damper.....	100
Figure 5.2 Prototype (a) Cylinder and caps (b) Rod-end cylinder cap.....	100
Figure 5.3 Prototype (a) Gas chamber-end cylinder cap with high pressure valve (b) Floating piston.	101
Figure 5.4 Prototype (a) wounded coil (b) Assembled piston.....	102
Figure 5.5 Prototype MR damper (a) Assembled part without cylinder (b) Assembled MR damper.....	103
Figure 5.6 Magnetic core and poles design.	103
Figure 5.7 Amplitude change effect for prototype MR damper (a) FD curves (b) FV curves.....	104
Figure 5.8 Frequency effect for prototype MR damper (a) FD curves (b) FV curves.	104
Figure 5.9 Input current effect for prototype MR damper (a) FD curves (b) FV curves.	105
Figure 5.10 Comparison of max damping force for predicted model and experimental data (a) low velocity @ 0.018 (m/s) (b) high velocity @ 0.867 (m/s).	106
Figure 5.11 Comparison of Lord MR damper and prototype (a) FD curve showing passive force comparison (b) FV curve showing passive force comparison (c) FD curve showing total force comparison (d) FV curve showing total force comparison	107

Chapter 1. Introduction

Downhill biking is a popular off-road biking consisting of high speed descents with extended air time off jumps and obstacles such as logs and rocks. The hasty and stimulating nature of downhill biking has emboldened mountain bikers to push their limits and aim for riskier goals. In order to assist customers overcome much tougher terrains, mountain bicycle manufacturers are competitively looking for new technologies to help them reduce weight while improving safety, handling, durability, and comfort of their bicycles.

In order to withstand harsh terrains and rocky paths, exceptionally strong frame, durable tires, and a suspension system with high travel capability are required. A main feature of a full suspension mountain bicycle is that the rear wheel suspends using a combination of shock absorber and spring coil, which allows rear wheel to displace relative to the main frame; hence providing safer and more comfortable ride, higher handling ability, less net rolling resistance, and better braking performance due to a harder grip between tire and surface. The rear suspension travel of typical downhill bicycles are between 7-10 inches (180-250mm)[1].

Common shock absorbers utilized in mountain bicycles are air shocks and spring coil shocks. Application of Magneto-Rheological (MR) dampers in mountain bicycles has attracted attention in recent years. Magneto-Rheological (MR) dampers are a new generation of dampers, which use controllable Magneto -Rheological Fluid (MRF). MRF is a smart material consisting of micron size ferromagnetic particles floating in a water-based solvent. The rheology of MRF can be controlled using magnetic flux. The required magnetic flux density is produced using of copper wires wound around a ferromagnetic core. The main considerations in designing these dampers are weight, power consumption, and response time[2]–[4].

1.1. Mountain bicycle rear suspension system

Mountain biking has significantly evolved recently, thanks to utilizing cutting-edge technologies in mountain bicycle design and fabrication. One of the most important components in a high performance mountain bicycle is the suspension system. The suspension system protects riders from roughness of the road and provides them with comfort and safety. The optimum design of a suspension system is dependent on whether it is used for cross-country or downhill biking[5]. Each application has different parameters that need to be considered in suspension design, due to the nature of the forces in the suspension system.

The forces that need to be considered in suspension system design are rider-induced forces (pedal force, weight), interstice forces existing between bicycle components (chain tension, shock absorber force), and terrain associated forces (vertical normal force). Different suspension designs are proposed to achieve desirable performance such as reducing bob-pedal, bio-pacing and DISC effect[6]. These designs include single pivot, URT, strut, and four bar linkages[5].

Besides the geometrical design impact, a shock absorber has significant impact on performance of the suspension system. The choice of material to improve shock absorber performance was investigated in [5]. Magneto-rheological fluids, owing to characteristics such as semi-active controllability, high reliability, and fail-safe performance were discussed in[3], [7]. Several MR damper devices have been developed recently, for example, in seismic damping of structures, MR elastomers in vibration control, and shock absorbers in automotive industries [8].

Three types of suspension systems have been proposed and successfully implemented in mountain bicycles: passive, active, and semi-active. Although, the passive shock absorber, featuring oil damping, provides design simplicity and cost-effectiveness, performance limitations are inevitable due to the lack of damping force controllability. On the other hand, an active shock absorber can provide high control performance in a wide frequency range. However, this type of damper may require high power sources, a large number of sensors, and complex actuators such as servo valves. One way to resolve this issue is to use a semi-active suspension system [3]. Semi-active

control systems offer the reliability of passive devices but maintain the versatility and adaptability of active systems. A semi-active control device can be adjusted in real time, but cannot input energy into the system being controlled. The force delivered by the damper is inherently constrained to be proportional and opposite to the excitation speed of the damper [9]

1.1.1. Conventional shocks

Shock absorbers are made of elastic and viscous elements in parallel with each other. Each element can be separately adjusted. Common shock absorbers utilized in mountain bicycles are either equipped with pre-inflated air chamber, or a pre-loaded spring coil, as their elastic element. The viscous element is generally an oil-filled cylinder divided into two chambers using a piston. The pressure drop due to passage of oil across the piston provides damping [6]. Selection of an appropriate shock absorber is directly dependent on the amount of rear wheel travel. Air springs show nonlinear and thus less predictable behavior [10]. Besides, air shocks produce smaller amounts of damping force. Downhill bicycles usually suffer more significant hits; therefore, coil spring shocks are usually employed to provide effective downhill shock absorption [5].

Many shocks offer external damping adjuster knobs, called rebound circuit knob, while others can be adjusted internally. Internal adjustments include changing the oil weight and viscosity, changing the orifice size [5], implementing a series of thin shims to avoid the passage of oil flow [11]. Adjustment of the rebound circuit knob changes the amount of oil flowing back through the orifice and shims. It can therefore control the damping coefficient and the speed by which the shock will open after hitting an obstacle. Fast or small rebound can result in bouncing the wheel off the ground, throwing the rider off balance, or providing poor traction. A slow or greater rebound makes the shock not to respond to the next impact, resulting in a harsh ride [3]. Adjustments can be made to tune the damping so that the best possible performance is achieved based on the rider's weight and riding style.

Another adjustable knob is the compression circuit, which controls the speed at which the shock collapses, or compresses, as it encounters an obstacle. Fast or small compression damping makes the shock to go through all its travel on smaller sized

bumps and bottom out, whilst, too much compression damping will induce a harsh feeling and will not achieve full travel [5]. A detailed examination of a conventional shock absorber is provided in chapter 4.

Additionally, high end shock absorbers intended for more aggressive riding, have two external compression adjustments: high and low speed. High-speed compression damping controls the shaft motion during sharp, sudden impacts, and reduces bottom out. Furthermore, low-speed compression damping controls the shock during low velocity shaft movement such as braking and smaller bumps, reducing brake dive and loss of biker's energy while pedaling [5]. In addition, high-end shocks are heavier and more expensive.

1.1.2. Semi-active shocks

In conventional shock absorbers, the rider must adjust the settings for each riding scenario by dismounting the bicycle and manually adjusting the knobs to the desired configuration. This requires the rider to carry additional tools which may cause some discomfort if riding conditions change during a downhill travel. Besides, performance of a conventional shock absorber is highly affected by temperature changes during the course of each ride. Also, since in passive shocks the stiffness and damping are tuned for a specific design condition, one cannot provide optimal vibration isolation for various road conditions[12]. The above limitations of conventional shocks have motivated mountain bicycle manufacturers to seek alternative solutions. Semi-active, fail-safe controllable Magneto rheological (MR) dampers are amongst the proposed solutions.

A conventional MR damper consists of a cylinder divided into two chambers, filled with MR fluid, and separated by a piston head. The piston head contains a magnetic circuit and orifices. Whenever the rod moves; the MR fluid flows between chambers through the orifice, where the MR fluid is exposed to the applied magnetic field. A gas chamber is located in the lower chamber to compensate for the volume of rod, which occupies upper chamber. Note that a gas accumulator may be used inside the cylinder or an additional cylinder may be attached to the main body [3], [13].

MR dampers have a relatively small power consumption, are semi-actively controllable, and can respond quickly, Durability, wide dynamic range, and continuously variable damping are other desirable features of MR dampers. The above potential characteristics of MR dampers have lured shock absorber manufacturers to consider their utilization in mountain bicycle applications [11], [14].

1.2. Research motivation and contributions

MR dampers have been vastly utilized in auto industries lately. Cadillac ATS, Chevrolet Corvette, Ferrari 458 Italia, Audi TT, and R8 are amongst vehicles which are equipped with MR dampers, known as, MagneRide™. In this thesis we study the application of MR dampers for mountain bikes to address the following topics and contributions:

- A. Development of a test mechanism to perform compression and tension tests on existing MR dampers and selection of conventional shock absorbers.
- B. Analysis of the acquired data for comparing characteristics of various shocks and their comparison with MR-based solutions. This is a feasibility study for adopting MR dampers in mountain bicycles.
- C. Investigation of different types of MR dampers in terms of their relative behavior and determining efficient designs.
- D. Application of finite element analysis to simulate magnetic fields and calculation of the amount of magnetic flux.
- E. Contribute an optimization method to optimize the damper components including piston valve to minimize the weight while maximizing the value of damping.
- F. CAD design of prototype MR damper by considering manufacturing issues, material availability, and sealing.
- G. Fabrication of a lightweight MR damper for mountain bicycle application.
- H. Running of experimental tests to illustrate performance properties of prototyped damper.

1.3. Fabrication and assembly of a prototype MR damper

Thesis outline

This thesis is organized in seven chapters. Chapter 1 provides a brief introduction to the mountain bike rear suspension system various types of shock absorbers, and the motivation for this thesis. Chapter 2 discusses background information on MR fluids such as rheology, magnetism, modes, structure, and applications. Chapter 3 presents the test mechanism that was assembled to perform dynamic tests on several bike shock absorbers, and their comparison with an MR damper. Chapter 4 investigates structural design details by disassembling an MR damper and a Fox shock absorber. Based on a selected MR structure, an appropriate magnetic circuit is designed to provide damping. In this chapter, a finite element model of piston valve was utilized to achieve design accuracy. Chapter 5 combines the FEA model, previously developed, with optimization methods to achieve an optimised design for the piston valve. Chapter 6 covers further details in prototyping the damper including material selection, sealing process, CAD modeling, and fabrication of the MR damper. Conclusions are presented in chapter 7 along with suggestions for future work.

Chapter 2. Review of MR Fluid and MR Damper Mechanism

This chapter provides an introduction to MR fluids. Topics such as MR effect, composition and structure of MR fluid, rheological and magnetic properties, models for MR fluid, and modes of operation are presented.

2.1. MR Fluid

Smart materials are a class of materials which have one or more properties that effectively changes by external stimuli such as stress, temperature, electric, or magnetic field. For instance, Piezoelectric (electrical voltage to mechanical strain), Pyroelectrics (temperature to electric polarization), Electrorheological Materials (electric field to rheology change) and Magnetorheological Materials (magnetic field to rheology change) [3]. MR fluid is a type of smart material consisting of suspended microscopic magnetic

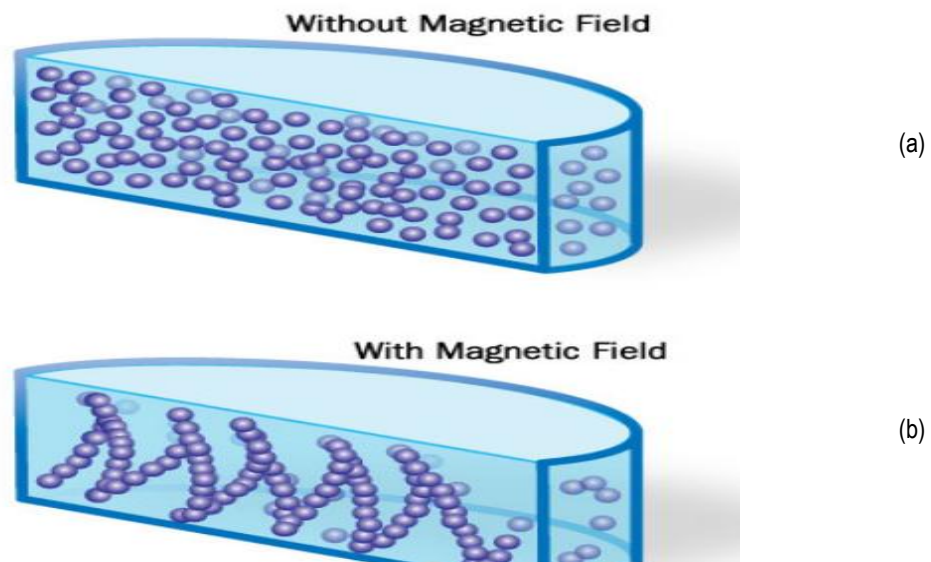


Figure 2.1 (a) MRF in absence of a magnetic field, (b) MRF particle alignment under influence of magnetic field.

particles in a base carrier fluid, which shows sudden changes in rheological properties in the presence of a magnetic field. MR fluid can be visualized as a very large number of macron-sized beads that are threaded onto a very thin string. This string is stretched between two magnetic poles alongside the magnetic field Figure 2.1[8].MR fluid changes state from free flowing fluid to a solid state. This process is reversible by eliminating the magnetic field. The early discovery of MR fluids can be accredited to Jacob Rabinow at the US National Bureau of Standards in the 1940s [3], [8], [15].

2.1.1. MR Fluid components and composition

Generally, there are three basic components in a conventional MR fluid.

Base fluid, solvent, or carrier oil is a non-magnetizable liquid which combines lubrication and damping features. To maximize the MR effect, the carrier oil should be low-viscous and insensitive to temperature changes, so that during the off-state the MR effect is the dominant factor in creating shear stress [16].There are various types of liquids which can be utilized including hydrocarbon, mineral, silicon, and hydraulic oils; silicone copolymers, polyester, polyether; halogenated organic liquids, diesters, polyoxyalkylenes, fluorinated silicones, glycols, and water [3], [13], [17]–[19].A combination of these fluids may also be used as the carrier component of the MR fluid [19].

Ferromagnetic particles: Alignment of these particles along path of magnetic field causes the MR effect [16]. The most common magnetic particles used are iron, iron/cobalt alloys, iron oxides, iron nitride, iron carbide, and carbonyl iron. These particles yield high magnetic saturation values in the order of 2.1 T[3], [16]. Magnetic materials can take as high as 50% of the total volume. Increasing the volume fraction of magnetic material and employing a rapid compression-assisted-aggregation process can force MR fluids to form a microstructure [3], [16], [20] and highly affect yield shear stress in MR fluids.

The additives: Few different additives can be used in MR fluids including surfactants, nanoparticles, nanomagnetizable, or coating magnetizable particles [19]. Additives are suspending compounds, with shear thinning property and ability to modify

friction which should be anti-corrosion/wear [16]. Thixotropic materials such as grease, metal soaps, lithium stearate, or sodium stearate have high viscosities in static conditions and become thin over time when shaken, agitated, or otherwise stressed. These materials are very effective in preventing caking or particle sedimentation and can alleviate the settling problem [10], [15]–[17]. Additives such as ferrous naphthanate or ferrous oleate can be used as dispersing agents to prevent clumping [21].

All three components of MR fluids above play a part in the Magneto-rheological behaviour of the MR fluid. The total density is a factor of particle volume fraction, and method of MR fluid composition. For a typical carbonyl iron based MR fluid, the value of volume fraction is approximately 3 to 5 g/cc , off-state viscosity is 0.1 to 0.3 ($Pa \cdot s^{-1}$ @ $25^\circ C$), the value of yield stress @ $1T$ is about 100 kPa , and size of magnetic particles are between 0.1 to 10 μm [3], [15]

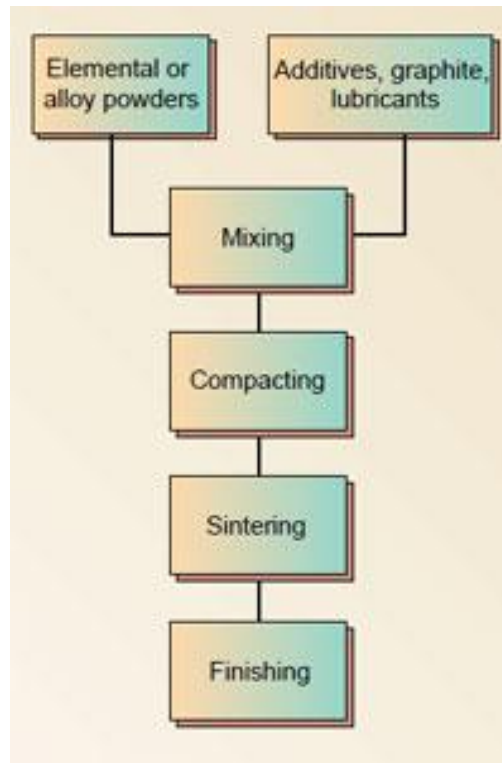


Figure 2.2 Powder metallurgy process main stages.

Powder metallurgy is a series of mechanical and chemical techniques, which are used to produce metallic powders [22], [23]. There are various methods for each stage Figure 2.2 illustrates three main stages of powder metallurgy consisting of mixing, compacting, and sintering [22]. Mixing is the process of combining metallic powder with binder and/or lubricant powder and additives. Mixing efficiency is dependent on shape and volume of the powder and rotation speed of the mixer. Powder flow can be hindered by high centrifugal forces that are created by rapid rotation. However, very slow rotation might prevent the mixing from happening [22]. Compacting forms a high density mass, provides shape, and generates dimensional control by applying external axial and isostatic pressure to mixed powder [22], [23]. Sintering is the process of bringing up the temperature of metal powders close to melting point. Duration and temperature of sintering have significant effects on properties of powder such as ductility, strength, fatigue life, electrical conductivity, and corrosion resistance [22], [23].

2.1.2. MR fluid magnetic behaviour

Magnetic material

Magnetic materials are categorised based on their magnetic behaviour, which is mainly determined by their electronic structures. The categories include diamagnetic, paramagnetic, ferromagnetic, ferromagnetic, and anti-ferromagnetic materials [3], [13]. Ferromagnetic materials have a large positive susceptibility to an external magnetic field, high magnetic permeability, and high magnetic saturation, when compared to other materials [3]. Ferromagnetic materials are able to retain their magnetic properties after the external field has been removed. A magnet is ferromagnetic material that attracts certain metals [13].

Three existing magnets can be categorized as permanent (hard) , temporary, and electromagnets[3], [13]. Loadstone, an iron oxide ore, excavated from magnetite is known to be one of the first magnets [22]. A permanent magnet holds on to its magnetic properties including high permeability, high coercivity, large hysteresis loop, and high remanence until demagnetized under certain circumstances [21]. Temporary magnets have the same properties as permanent magnets under the influence of a strong magnetic field. However, due to their low coercivity (narrow hysteresis), they magnetize

and demagnetize rapidly [13]. Electromagnets only magnetize in the presence of external magnetic fields. An example of these magnets is a solenoid wound around an iron core [3], [24].

The hysteresis curve, also known as the B-H curve, describes the ferromagnetic properties of materials. Coercivity H_c is a measure of the external magnetic field required to decrease the magnetization of a material to zero after it has reached saturation, which indicates the width of the hysteresis curve [3]. Remanence, residual magnetism, or residual flux B_r is the value of remaining magnetism, or remaining flux in a substance, after the external magnetic field is reduced to zero [13], [22]. It is the point that the hysteresis curve intersects the magnetic flux density B axis. The saturation flux density B_{Sat} , or B_{Max} , is the maximum flux density that a material can reach. After that point, increasing field intensity does not elevate the magnetic flux density [25]. Magnetic susceptibility, χ_m , is the extent of magnetization of a material in response to a magnetic field [3]. Magnetic permeability μ represents the ability of a material to achieve a high magnetization in a relatively small magnetic field [3], [13]. In other words, permeability is the ease of

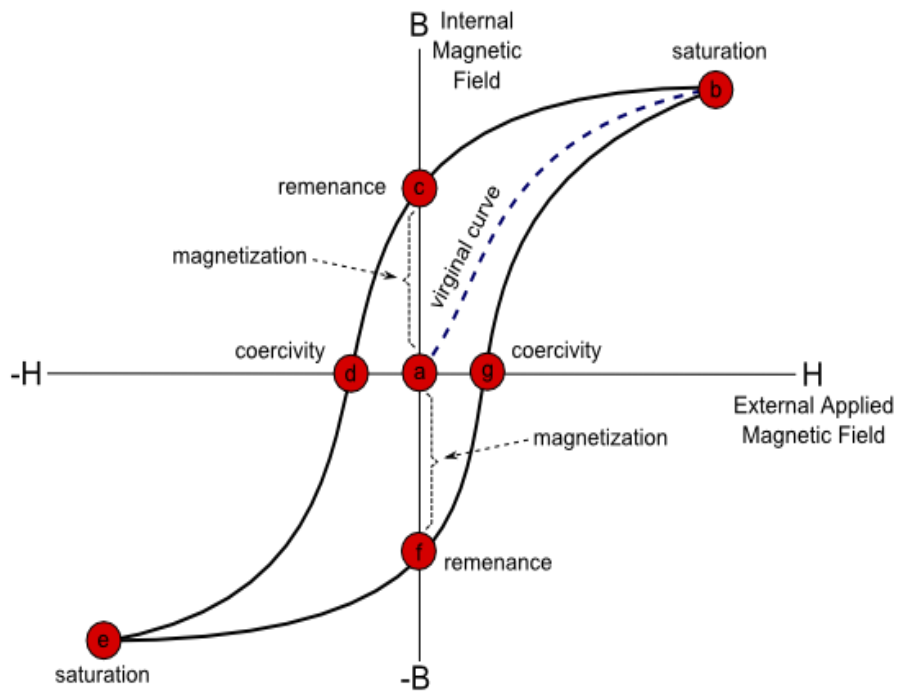


Figure 2.3 Typical hysteresis loop for a ferromagnetic material.

establishing a magnetic flux in the component [22]. Also, the slope of the linear section of hysteresis curve represents the permeability of a substance. Relative permeability μ_r indicates the ratio of permeability of a magnetic material to the permeability of vacuum, $4\pi * 10^{-7} H.m^{-1}$ [3]. Figure 2.3 exhibits a typical hysteresis curve for a ferromagnetic material.

In general, hard magnetic materials are more difficult to magnetize and demagnetize, whereas soft magnetic materials easily adopt magnetization and once the magnetizing field is removed, the flux density instantly goes to zero[3]. A soft magnetic material typically exhibits a high permeability and a small intrinsic coercivity of less than $100 Am^{-1}$. Hence, they are mainly used as magnetic cores to enhance and channel the flux produced by the electric current of a solenoid [22]. Permeability is a main consideration in selection of material in DC applications where saturation may be significant. In AC applications, energy loss is the most important factor in material selection, since the material is cycled around its hysteresis loop[3]. Figure 2.4 shows the soft and hard material hysteresis loops. The low coercivity and high saturation flux density of a soft magnetic material result in a narrow loop when compared to a hard material due to high coercivity.

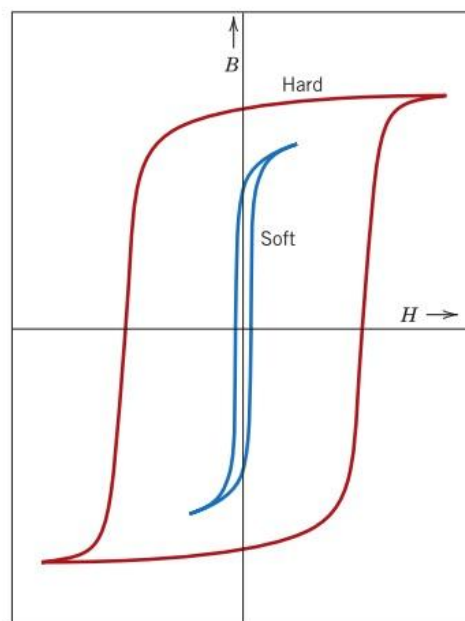


Figure 2.4 Comparison of soft and hard magnetic material hysteresis curve.

Concept of electromagnetism

The motion of electronic charges, such as electric current, generates magnetic fields. Solenoids or wounded coils are usually utilized to produce magnetic fields. Figure 2.5(a) exhibits a solenoid around an air core [3]. Soft magnetic cores propagate magnetic fields [13]. Figure 2.5 (b) shows a solenoid with a soft magnetic core and a magnetic flux path [22]. A solenoid with a soft magnetic core reacts like a simple magnet, in which one end of the coil is the North Pole, and the other end is the South Pole. The total magnetic field is obtained by superposing the magnetic fields due to all the turns [22].

For a solenoid, the magnetic flux density of center of core and magnetic field intensity can be calculated from [22], [26]:

$$B = \mu \cdot H \quad 2.1$$

$$H = \frac{NI}{\sqrt{4r^2 + l^2}} \quad 2.2$$

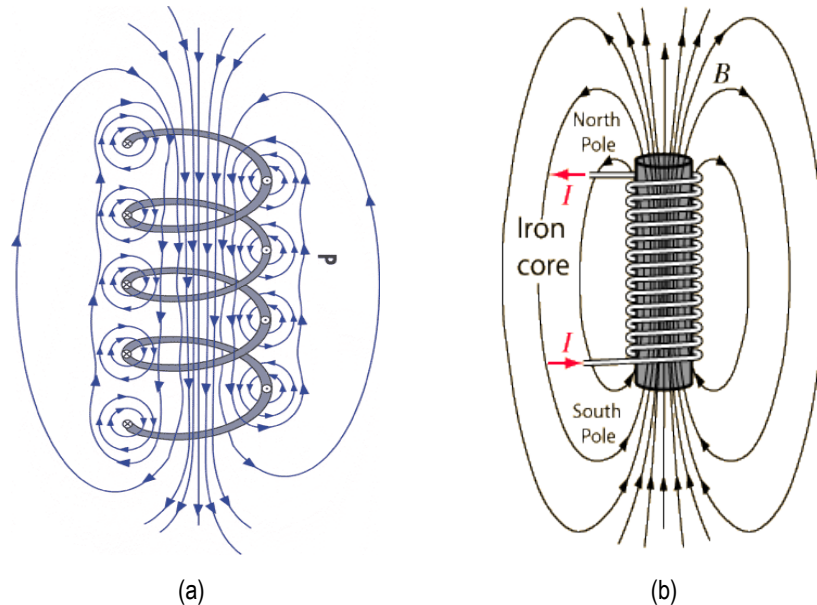


Figure 2.5 (a) Solenoid coil wound around the air (b) Solenoid wound around a soft magnetic core.

where B is magnetic flux density (*Tesla*), H is magnetic field strength (*Henries*), or intensity; μ is magnetic permeability constant, N is the number of loops or turns of windings, I is the current flow through the coil (*Ampere*), r is the effective radius of the coil (m), and l is the length of the coil (m).

The following relationship provides a formula between magnetic flux density, magnetic field intensity, and magnetization [3], [27]:

$$\mu = \mu_r \cdot \mu_0 \tag{2.3}$$

$$B = \mu_0 H + \mu_0 M \tag{2.4}$$

$$M = \chi_m \cdot H \tag{2.5}$$

$$\mu_r = 1 + \chi_m \tag{2.6}$$

where M is Magnetization, χ_m is magnetic susceptibility, μ_r is relative permeability of the soft magnetic material, and is used to extent of a material magnetization, and μ_0 is permeability of vacuum (H/m).

MR Fluid magnetic properties

Conceptually, the combination of applied flux density and the particle organizational state governs $\frac{dx}{dt}$ which is the rate of change of organizational state [28]. Magnetic properties of an MR fluid can be derived from its B-H and M-H hysteresis curves. That knowledge is essential in designing any MR device, since the response to an applied current can be predicted using the hysteresis loop [3]. There are various measurement methods to acquire the hysteresis loop such as vibrating sample magnetometer (VSM) [3], [29] and alternating gradient magnetometer (AGM) [3]. Figure 2.6 shows the B-H curve of a commercial MR fluid by Lord Corp.

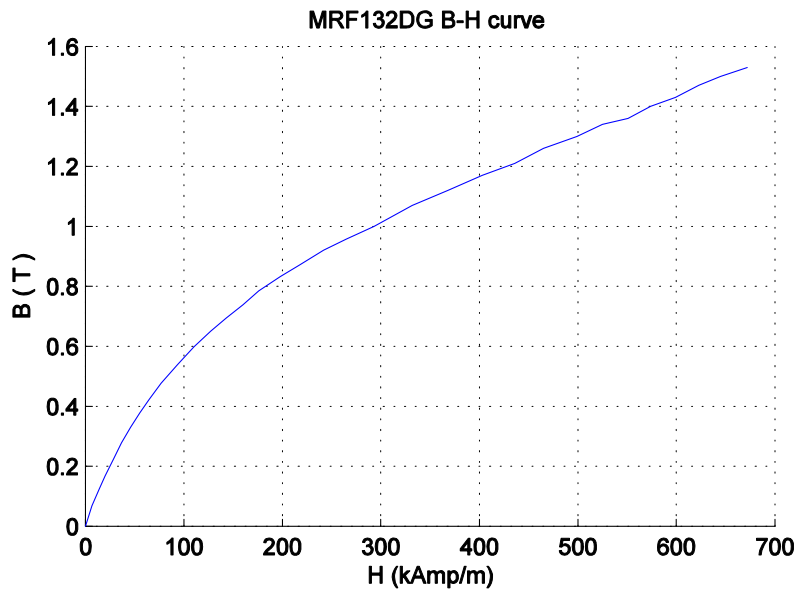


Figure 2.6 B-H curve of MRF132DG MR fluid by Lord Corp.

2.1.3. Rheology of MR fluid

Basics of rheology

Study of flow properties and response of a material to applied stress is called rheology [3]. Rheology for solids and liquids is the response of materials to applied stress, which is mainly concentrated on the relationship between shear stress and shear strain[30].Figure 2.7 shows the concept of shear stress when a force is applied onto the surface of a fluid element. When a shearing force F is applied at the top area A of the element, shear stress is calculated as follows:

$$\tau = \frac{F}{A} \quad 2.7$$

Which is the ratio of force over effective area which is equal to the force per unit area [3]. Relatively, shear stress generates a deformation, called shear strain. In fluids, shear strain might change depending on the rheological properties of that fluid and duration of time, while shear stress in applied [3].

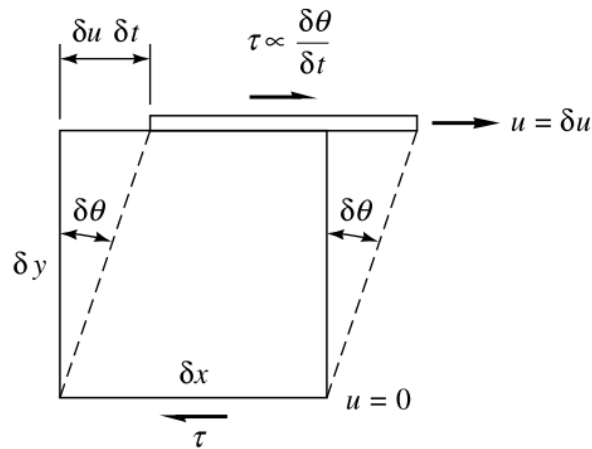


Figure 2.7 Shear force applied to a surface[30].

The shear strain angle $\delta\theta$ will continuously grow with time, as long as the stress τ is applied and the upper surface moving at speed δu larger than the lower. From the geometry of Figure 2.7, when a small particle moves $\delta u \delta t$ on the surface, small deformation known as shear strain is generated, due to shear stress. Shear strain can be written as:

$$\gamma = \tan \delta\theta = \frac{\delta u \delta t}{\delta y} \tag{2.8}$$

In the limit of infinitesimal changes, this becomes a relation between shear strain rate and velocity gradient $\frac{du}{dy}$:

$$\frac{d\theta}{dt} = \frac{du}{dy} \tag{2.9}$$

Shear stress is proportional to the rate of shear strain, as a result:

$$\tau = \text{Constaant} * \dot{\gamma} \tag{2.10}$$

When a fluid under shear stress, it begins to move at a strain rate inversely proportional to a property called its coefficient of viscosity [30]

Non-Newtonian fluids are a kind of Newtonian fluids with a different stress-strain relationship. Newtonian fluids have proportional shear strain rate changes to applied viscous stress. Equation 2.12 shows the main ruling formula over Newtonian fluid flow. On the contrary, non-Newtonian fluids significantly deviate from stress-strain behaviour. Equation 2.11 is the governing formula over non-Newtonian fluids [3], [30], [31].

$$\tau = \eta \cdot \frac{du}{dt} \quad 2.12$$

$$\tau = \tau_y + \eta \left(\frac{du}{dt} \right)^n \quad 2.11$$

where, τ is the shear stress (Pa), u velocity distribution ($\frac{m}{s}$), η is viscosity coefficient ($\frac{kg}{s.m}$), or dynamic viscosity, $\frac{du}{dt}$ is strain rate (s^{-1}), τ_y is yield stress (Pa), n is coefficient that varies for all types of Newtonian and non-Newtonian fluids.

Non-Newtonian fluids are categorized, based on their stress-deformation rate behavior. Resistance of Dilatant, or shear-thickening, is a condition in which the fluid raises with increasing the applied stress. Alternately, a Pseudo-plastic, or shear-thinning

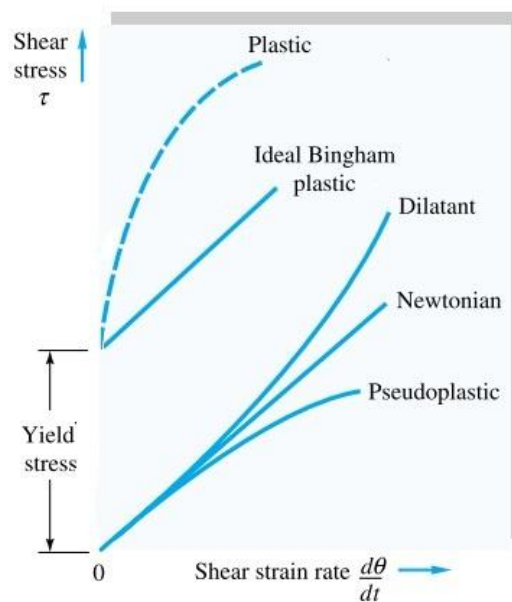


Figure 2.8 Rheological behavior of various viscous materials.

fluid decreases its resistance with increasing stress. If τ_y in Equation 2.11 equal zero, then $n > 1$ represents Dilatant fluid, and $n < 1$ represents pseudo-plastic fluid[3], [30]. A plastic material shows little or no deformation up to a certain level of stress, called the yield stress[31] in which the thinning effect is significant. The limiting case of a plastic substance is when the substance requires an initial yield stress before starting to flow. In other words, Bingham plastic behaves as a rigid body at low stresses but flows as a viscous fluid at high stress. Figure 2.8 shows various types of rheological behavior of viscous materials such as rheology behavior of the ideal Bingham plastic linear-flow is shown; noteworthy that in some substances post yield rheology behavior may be nonlinear[30]. Toothpaste is an example of a yielding fluid, which does flow out of the tube until the applied stress surpasses the yield stress[30].

Rheological properties of MR fluid

Unique rheological behaviour of MR fluids are as a result of various factors such as rapid liquid-to-solid transition, hydrodynamic forces, carrier oil viscosity, electrostatic forces, and size and shape of particles[3], [15]. MR fluids behave similar to a normal Newtonian fluid, in the absence of an external field[3], meaning that dynamic viscosity of Bingham plastics is regularly consistent [32]. MR fluids, appear to have similar apparent viscosities like the liquid paint ($0.1 - 1 \text{ Pa} \cdot \text{s}^{-1}$ at low shear rates), when operating in „off“ state [29], [33]

Figure 2.9 (a) shows the „off“ state behavior of an MR fluid. Although, a model such as the Bingham model proposes that stress less than yield stress results in no flow of MR fluid, in reality, the fluid reacts to stress as a viscoelastic solid. The shear stiffness of viscoelastic solid is often modeled by complex shear modulus G and strain γ . Equation 2.13 shows stress-strain relationship at viscoelastic domain[32]:

$$\tau = \gamma G \quad \tau < \tau_y \quad 2.13$$

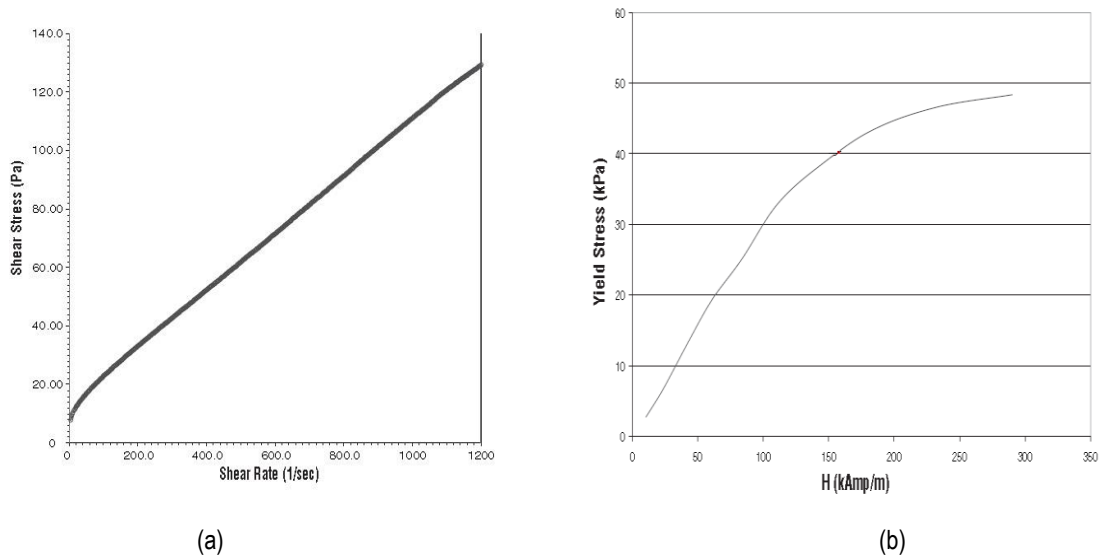


Figure 2.9 MRF132DG Lord Corp MR fluid (a) Shear stress Vs Shear rate (b) Yield stress Vs Magnetic field intensity.

Whenever an external magnetic field is applied, the static yield stress of MR fluid increases substantially [29]. Once aligned; the iron particles become magnetized and resist moving out of their respective magnetic field. Aligned magnets act as a barrier to an external force; therefore, a shear stress, or a pressure difference is necessary to break this structure[19]. At zero shear rate under stress, the fluid resists to flow. Meanwhile, the force causes a plastic deformation while there is no continuous movement. In this condition, the maximum stress, which can be applied without causing continuous movement, is the yield stress [16]. As mentioned before, the strength of MR Fluid known as static yield stress, increases the non-linearly by increasing the magnetic field intensity [3], [29]. Yield stress $\tau_y(H)$, which is a function of the magnetic field intensity, signifies the maximum of stress-strain curve. The particle chains will be breached when the stress has reached this maximum after which the MR fluid will start to flow even in „on“ state [3], [29], [34]. In other words, yield stress must be overcome to initiate gross material deformation or flow [18]. Equation 2.15 can be used to calculate the shear stress.

$$\tau = \tau_y(H) + \eta \dot{\gamma} \qquad \tau > \tau_y \qquad 2.15$$

where, τ is total shear stress, the field dependent yield stress is τ_y , and is produced by an applied magnetic field intensity H , $\dot{\gamma}$ is shear strain rate, and η is dynamic viscosity of fluid. Figure 2.9 (b) exhibits non-linearity of yield stress vs. magnetic field intensity curve.

An optimum MR fluid has minimum viscosity during „off“ state, while during „on“ state yield stress of the fluid is maximized. Both viscosities are very important in order to achieve a maximum MR effect. Turn-up ratio represents the dynamic range of MR fluid, which is the differences between off-state viscosity and on-state yield stress [3]. The MR fluid yield stress can be elevated using certain techniques such as increasing the volume fraction of MR particles, increasing the strength of the applied magnetic field [19], and using materials with higher saturation magnetization [29]. However, none of these techniques is efficient. A higher volume fraction of magnetic particles significantly increases the weight of the MR devices while increasing the viscosity of „off“ state of the material.

Furthermore, a higher magnetic field substantially increases the power consumption of the device[19]. Also, the cost and availability of material with high saturation magnetization is a limiting factor[29]. Generally speaking, MR fluids must have large saturation magnetization and small coercivity/remnant magnetization, be active over a wide temperature range, and be stable against settling, irreversible flocculation, chemical degradation and oxidation. The field-dependent mechanical strength of MR fluids depend on the composition, particle size, and volume fraction[3].

MR fluid models

The behaviour of MR fluids is characterized by a modified Bingham model, or a combination of Bingham model with other models such as viscous and coulomb friction[3]. An MR fluid shows nonlinear behavior when exposed to external magnetic fields. Materials rheology can be separated into distinct pre-yield and post-yield domains[19]. Various nonlinear models have been proposed to characterize MR fluids[19]. The Bingham plastic model is a widely used method to describe the MR behavior [3], [18], [19]. Other models have been proposed to better model complex behaviors of MR fluids. The Herschel–Bulkley model, considers the MR fluid’s shear thickening and thinning effects [19], [32]. A nonlinear bi-viscous model was presented in [35] which is based on an expanded version of the Bingham model. Another model,

called Buckingham model (Bingham modified), has been proposed by considering a nonlinear magnetic flux distribution across a small gap [35].

Bingham plastic model

The Bingham plastic model is commonly used to explain behavior of MR fluid, model consists of a variable plastic element in parallel with a Newtonian viscosity element. In the pre-yield region, shear stress is less than the dynamic yield[36]. Furthermore, shear stress is proportional to shear rate in the post-yield region in this model[37]. This model can be formulated as:

$$\tau = \tau_y(H)sgn(\dot{\gamma}) + \eta \dot{\gamma} \tag{2.17}$$

where τ is shear stress, η is dynamic viscosity, $\dot{\gamma}$ is strain rate (s^{-1}), τ_y is the field dependent yield stress, and $sgn(\cdot)$ is the signum function. The Bingham plastic shear stress-strain model is shown in Figure 2.10 (a), where γ_y is the pre-yield strain. The pre-yield region has a strong viscoelastic nature, whereas the post-yield region demonstrates a dominant viscous behaviour. The two rheological domains are separated

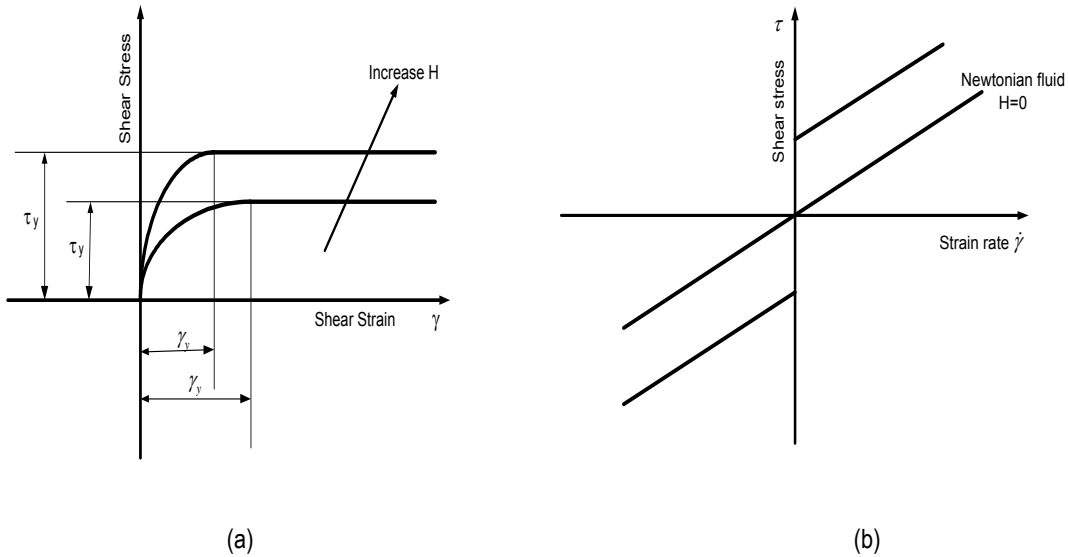


Figure 2.10 (a) stress-strain of MR fluid (b) Bingham model of MR fluid.

by a yield point which is determined by the applied magnetic field. In the post yield region, the shear stress versus the shear strain rate is close to a linear relationship. Figure 2.10 (b) shows shear stress-shear strain rate of Bingham model.

Herschel-Bulkley plastic model

Herschel-Bulkley fluids are materials that act like a rigid material in shear stresses below the yield stress. When the shear stress exceeds that limit, the material flows with a non-linear stress-strain rate relationship. This model is a modified version of Bingham plastic [38]. This model is more suitable for high shear stress regions, since it shows non-linear change of shear strain rate; therefore, it corrects overestimations made by Bingham model [19]. Model can be expressed as:

$$\tau = (\tau_y(H) \operatorname{sgn}(\dot{\gamma}) + K|\dot{\gamma}|^{\frac{1}{m}})\dot{\gamma} \quad 2.18$$

where K is the consistency parameter, and m is fluid behavior index of the MR fluid. For $m > 1$, Equation 2.18 expresses a shear thinning fluid, while shear thickening fluids

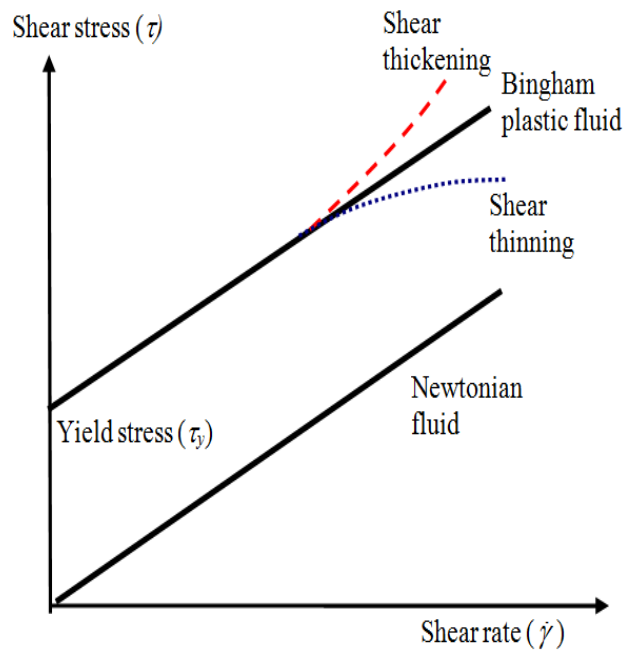


Figure 2.11 Herschel-Bulkley model of MR fluid.

are described by $m < 1$. Additionally, for $m = 1$ the Herschel–Bulkley model is similar to Bingham plastic model, Figure 2.11. Various other models have been proposed to estimate the behaviour of MR fluids more accurately. Bingham model is used throughout this thesis in the initial design stage.

2.1.4. MR Fluid modes and applications

Depending on the fluid flow, and rheological stress, there are three operational modes for MR fluids: The Valve mode, the Direct Shear mode, and the Squeeze mode. Devices can use each one of these modes, or various combinations of them, based on the target applications. It is important to know that more than one mode of MR fluid can be facilitated, in order to achieve greater force and more functionality [3].

Valve mode

In the valve mode, the fluid is located between a pair of stationary poles. Flow between two parallel plates is created by pressure drop [39]. The resistance to the fluid flow is controlled by changing the magnetic field intensity between the poles, in a direction perpendicular to the flow, Figure 2.12 (a). Devices using this mode of operation include servo-valves, dampers, shock absorbers and actuators.

The typical shear stress diagram and velocity profile of the Bingham plastic flow in a rectangular annular gap is shown in Figure 2.12(b). Two separate flow regions are indicated. The central plug region, Region 1, or pre-yield region; is characterized when the shear stress is less than the fluid yield stress, and the shear rate or velocity gradient is zero. Additionally, the plug thickness δ is the width of pre-yield region. The post-yield region, or Region 2, is where the local shear stress exceeds the yield stress of the fluid[19], [36]. Figure 2.12 (c) illustrates flow of MR in between the two parallel plates.

The pressure drop ΔP developed in the valve mode in a device can be divided into a field independent viscous component ΔP_{η} , and yield stress dependant component ΔP_{τ} . These components can be calculated with[15], [40]:

$$\Delta P = \Delta P\tau + \Delta P\eta . \quad 2.19$$

$$\Delta P\eta = \frac{12 \eta QL}{g^3 w} \quad 2.20$$

$$\Delta P\tau = \frac{c\tau(H)L}{g} \quad 2.21$$

where Q is the volumetric flow rate, η is the dynamic viscosity with no applied field and $\tau(H)$ is the field dependant yield stress, the parameter c ranges from a minimum value of 2 (for $\Delta P\tau/\Delta P\eta$ less than ~ 1) to a maximum value of 3 (for $\Delta P\tau/\Delta P\eta$ greater than ~ 100)[15], [16]. The most common application of valve mode is in dampers. MR dampers have utilized MR fluid both in valve mode and direct shear mode; but since 2002, GM / Delphi used valve mode in damper designs for automotive vehicle suspensions valve due to simplicity and functionality [16]. MR dampers are fully investigated in section 2.2.

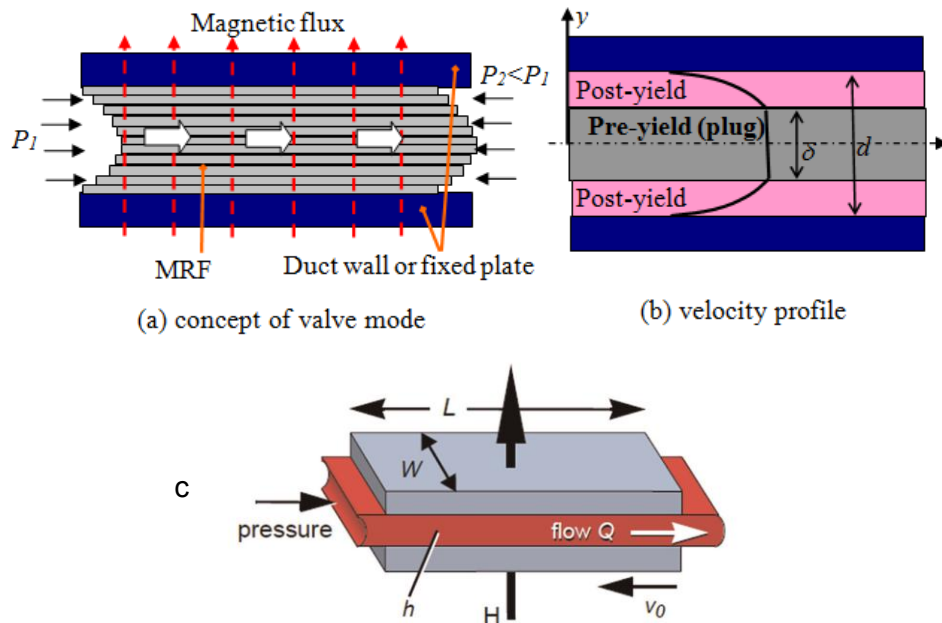


Figure 2.12 (a) concept of valve mode (b) Bingham velocity profile of MR fluid in valve mode [19](c) flow through a parallel duct [48].

Shear mode

In direct shear mode, MR fluid is situated between two surfaces; one of which is fixed and the other one slides or rotates with respect to the first surface. A magnetic field is applied perpendicular to the direction of motion of these shear surfaces[19]. Figure 2.13 (a) shows the concept of shear mode in MR fluid application.

Figure 2.13 (b) illustrates a typical shear stress diagram and velocity profile of the Bingham plastic shear flow in an annular. There are three different flow regions, Region C (pre-yield region) is where no flow happens, since shear stress is less than yield stress. The MR fluid flows in regions I & II (post-yield regions), due to exceeding of shear stress over yield stress. Boundaries of the regions are dependent on a plug thickness δ controlled by magnetic field intensity[41]. The pressure gradient, or pressure drop Δp , is given by equations of velocity profile, volume flow flux, and boundary conditions in three different flow regions[41], [42].

The total shear force developed by a device in shear mode is consist of viscous component F_η , and a magnetic field induced component F_τ [3], [15], [16]:

$$F = F_\eta + F_\tau \quad 2.22$$

$$F_\eta = \frac{\eta L w V}{g} \quad 2.23$$

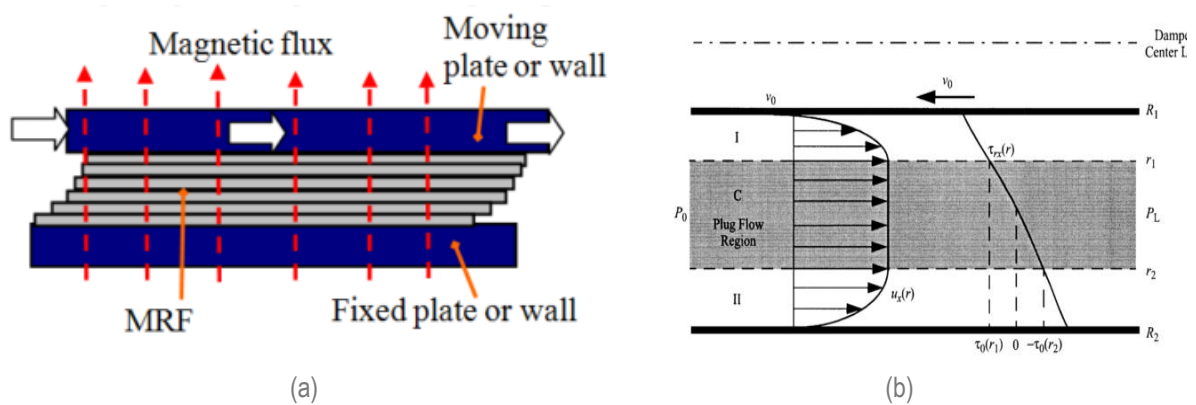


Figure 2.13 (a) concept of direct shear mode [19] (b) Bingham velocity profile of MR fluid in shear mode [15].

$$F_t = Lw\tau(H)$$

2.24

in this equation, η [Pa.s] is dynamic viscosity with no applied field, L ; w ; g [m], are length, width, and gap size of flow channel, relatively $A = Lw$ [m^2] is working interface area, $\tau(H)$ is yield stress developed by applied magnetic field, and V [m/s] is the relative speed of the pole plates [15], [41], [43]. The most important design consideration, when using shear mode operation, is controlling the ratio $\frac{F_t}{F_\eta}$, which indicates the range of intrinsic force that can be produced in the device. A large ratio indicates that the device is capable of enduring a major force variation from „off“ state to „on„ state [43]

Shear mode devices are the most popular operational modes after valve mode, due to extraordinary features of this mode such as simplicity, simple interface between electrical input and mechanical output, fast response, and controllability. These properties of the shear mode make MR fluid suitable for applications such as locking devices, dampers, breakaway devices, and structural composites [16], [41], [43].

MR Brakes

The direct shear mode of operation can be utilized in rotational power transfer devices such as rotary brakes and clutches. During the „off“ state, a negligible amount of shear force is produced by the MR fluid in a rotary brake, therefore it operates such as motor oil. Since there is no shear stress generated, the rotational pole plates can rotate easily with no force transmitted across the fluid. Once the magnetic field is applied perpendicular to flow direction, considerable shear stress is generated between the rotational disc and fixed plate. Hence, power can be transmitted from one plate to the other, and speed of the rotatory plate can be reduced or the plate can be stopped [43].

MR rotary brakes are highly controllable, generate high torque transfer in low speed, have low power requirements, and have fast response time (10-30 [ms]). Additionally, MR brakes have long-life, rugged construction, and are easily programmable [43]. Figure 2.14 exhibits different types of MR rotary brakes.

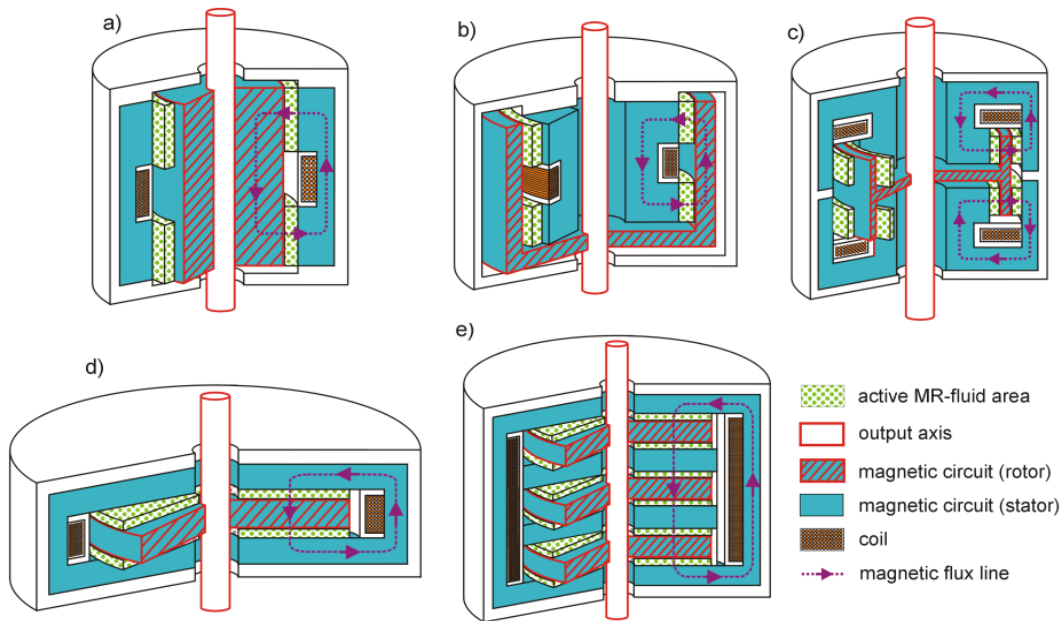


Figure 2.14 Major MR-brake designs: (a) drum (b) inverted drum (c) T-shaped rotor(d) disk (e) multiple disks.

Squeeze mode

In this mode, the fluid operates between a pair of moving magnetic poles. The relative displacement is perpendicular to the direction of the fluid flow as shown in Figure 2.15. The compression force applied to the fluid varies periodically. The displacements are small in comparison to other modes; however, resistive forces are considerably higher[44]. Alignment of magnetic particles in this mode is along the magnetic field,

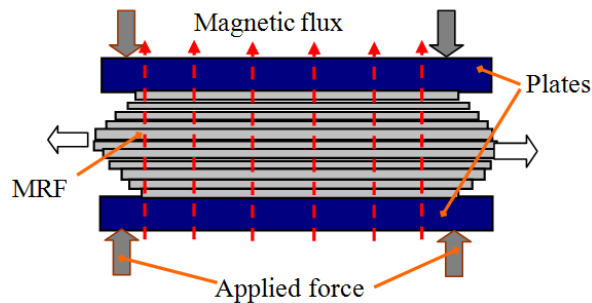


Figure 2.15 Concept of squeeze mode[19].

similar to other modes. When exposed to a magnetic field, the squeezing of MR fluid causes broken chains of particles to form shorter and more compact and strong chains[3], [45]. This behavior of MR fluid provides a wide range of controllable forces in comparison with other modes.

Three factors affect the amount of pressure produced in this operational mode, they are ongoing viscous forces, MR effect related forces, and pressure produced due to inertia of MR fluid. Since the amount of MR fluid is very small, inertia is negligible. A mathematical model is presented in [46] based on pressure sources. The squeeze mode has been explored for use in small amplitude vibration and impact dampers as discussed in [44]. Large structural vibration absorption systems, impact dampers, and engine mounts are examples of devices that can benefit from MR squeeze mode control[44].

MR fluid elastomer mount

Fluid filled elastomer vibration mount are made from rubber and MR fluid. Due to the reaction between MR fluid and rubber, the physical property of rubber changes by becoming softer and losing some elasticity. As a result, the shape of rubber changes [44]. The result is a hollow elastomer puck filled with MR fluid. The stiffness of this device can be adjusted using MR squeeze mode properties [43]. Figure 2.16(a) shows a MR squeeze mount. Changes in the shape and properties of rubber, due to relaxation of internal stresses, motivated researchers to find a substitute. A new polyurethane membrane was fabricated, tested, and validated [44]. Figure 2.16 (b) shows the structure of the new polyurethane membrane.

Typically, mechanical systems with a known operating frequency, such as constant RPM engines, use simple vibration isolators. Stiffness adjustable isolators are utilized in applications where the device might pass through a resonance zone such as start-up and shutdown of major scale steam turbines. These isolators can provide optimum vibration cancelation characteristics[43]. Other main applications are in squeeze mode rheometers, squeeze film damper, and haptic devices by which users can interact with virtual objects [3].

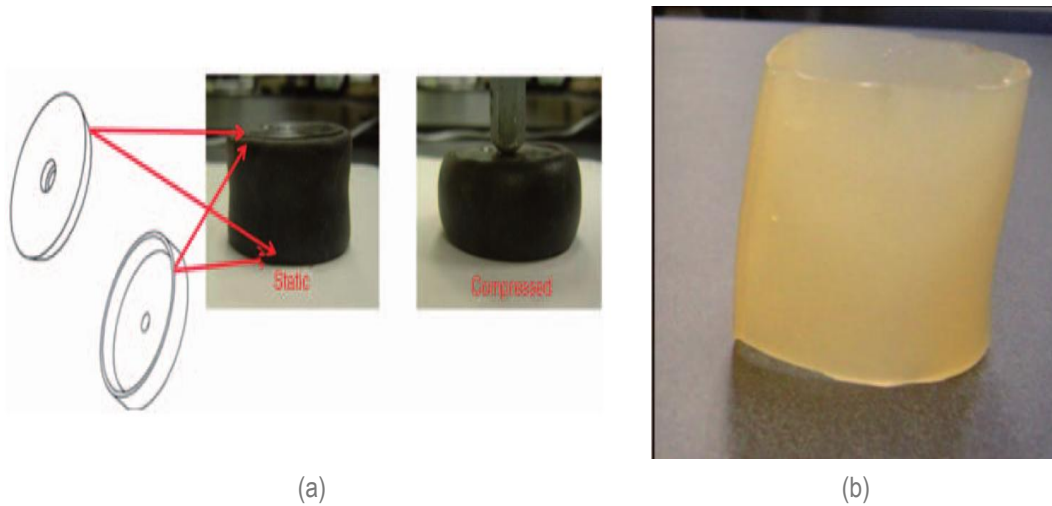


Figure 2.16 (a) Rubber puck shape vibration mount (b) new polyurethane membrane for vibration mount application[44].

2.2. MR Damper

MR Dampers are devices which employ MR fluid adjustable viscosity to reduce undesirable vibrations. High controllability, low power consumption, and durability of these devices have attracted a lot of attention recently. Applications include knee prosthesis, vibration dampers, active engine mounts, prop shaft mounts and seismic dampers for civil industry[3]. In automotive suspension systems and mountain bicycles linear MR dampers are used. The focus of this thesis is on linear MR dampers.

In this section, a review of the previous works is presented. First, various designs of MR damper components are studied; followed by models describing MR dampers properties. Finally, a review of previous works on the application of MR dampers in mountain bicycles suspension system is presented.

2.2.1. MR damper components and designs

MR damper consists of a hydraulic cylinder, containing MR fluid; and a magnetic control valve, which is implemented in a piston head and has the duty to produce the necessary magnetic field. MR fluid usually passes through the valve, under the influence of a magnetic field, and can reversibly change from a free-flowing linear viscous fluid to a

semisolid with controllable yield strength instantaneously [46]. Different designs have been proposed for cylinder and control valve of MR dampers. Some of these designs are investigated in this thesis as follows.

Cylinder structures

MR dampers may consist of various cylinder sizes and materials and utilize different modes of MR fluid, based on their application and configuration. In cases that cylinders are used as part of the magnetic flux loop, shear mode can be engaged and the cylinder needs to be fabricated from magnetic materials. In applications where the magnetic flux path is completed without engagement of the cylinder, the valve mode is usually engaged in which the materials can be non-magnetic. Since cylinders are usually under high pressure, in contact with highly corrosive MR fluid, the materials need to be appropriately selected.

Monotube damper structure

A basic type of MR damper cylinder is the monotube damper shown in Figure 2.17. The cylinder is divided into two chambers, called extension chamber and compression chamber, using a piston head which contains a control valve. The MR fluid flows between chambers through the orifice of the piston head, where MR fluid is exposed to the applied magnetic field [8], [47], [48]. A pressure differential is produced as a result of changes in the viscosity of MR fluid passing through the orifice, which is proportional to amount of induced magnetic field[48]. There exists an accumulator located at the compression chamber part of cylinder, which is a floating piston or a diaphragm, separating MR fluid from a compressible gas (Nitrogen). The accumulator accommodates volume change of incompressible MR fluid due to the shaft rod entering the cylinder. Moreover, it operates as an offset air spring force in addition to the damping force. It also prevents formation of cavities in low pressure side of the piston head[41], [49], [50].

Monotube designs are known to have simpler mechanical structures with fewer parts, resulting in less weight and lower manufacturing cost. On the other hand, monotube dampers are more vulnerable to impacts and need more gas be pressurized, which reduces the dynamic force range of the damper [48], [49].

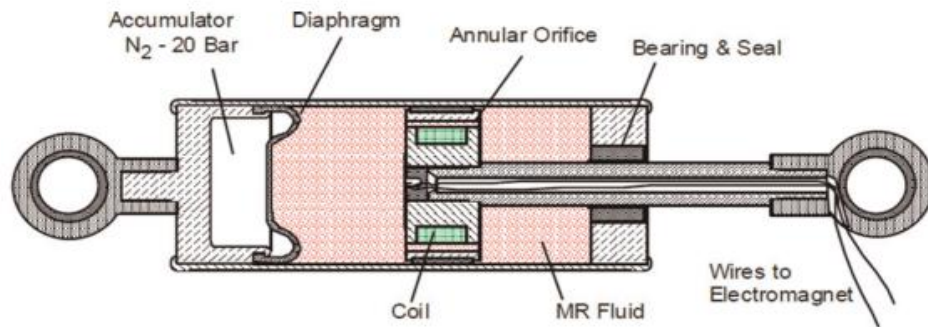


Figure 2.17 Mono tube cylinder[8].

Twin tube structure

The basic conceptual structure of a twin-tube MR damper is shown in Figure 2.18 (a). MR damper has an inner and an outer housing[8]. The inner housing is filled with MR fluid and acts as a mono-tube cylinder. The outer housing is partly filled with MRF and acts as a pneumatic accumulator in the mono-tube mechanism by accommodating volume changes produced by piston displacement. Figure 2.18 (b) exhibits a sectional view of a twin-tube damper. A regulating valve assembly attached to the bottom part of inner cylinder, called “foot valve”, is shown in Figure 2.18 (c). The foot valve is responsible for regulating the flow of MR fluid between two housings[8], [48]. During compression, the rod enters the extension chamber, which causes the MR fluid to flow to the outer housing through the foot valve. The volume of MR fluid displaced by the rod is the amount that flows into the outer piston. The process is reversed during extension of the shaft [51].

A main advantage of the twin-tube MR damper is that the gas pressure in gas accumulator is less than the mono-tube MR damper [8], [47], [52]. Another advantage of using the outer housing is that dissipated heat can easily be transferred to the outside environment and the inner mechanism of MR damper is protected by the outer cylinder[49]. However, complexity and higher weight makes this design unfavorable for mountain bicycle applications.

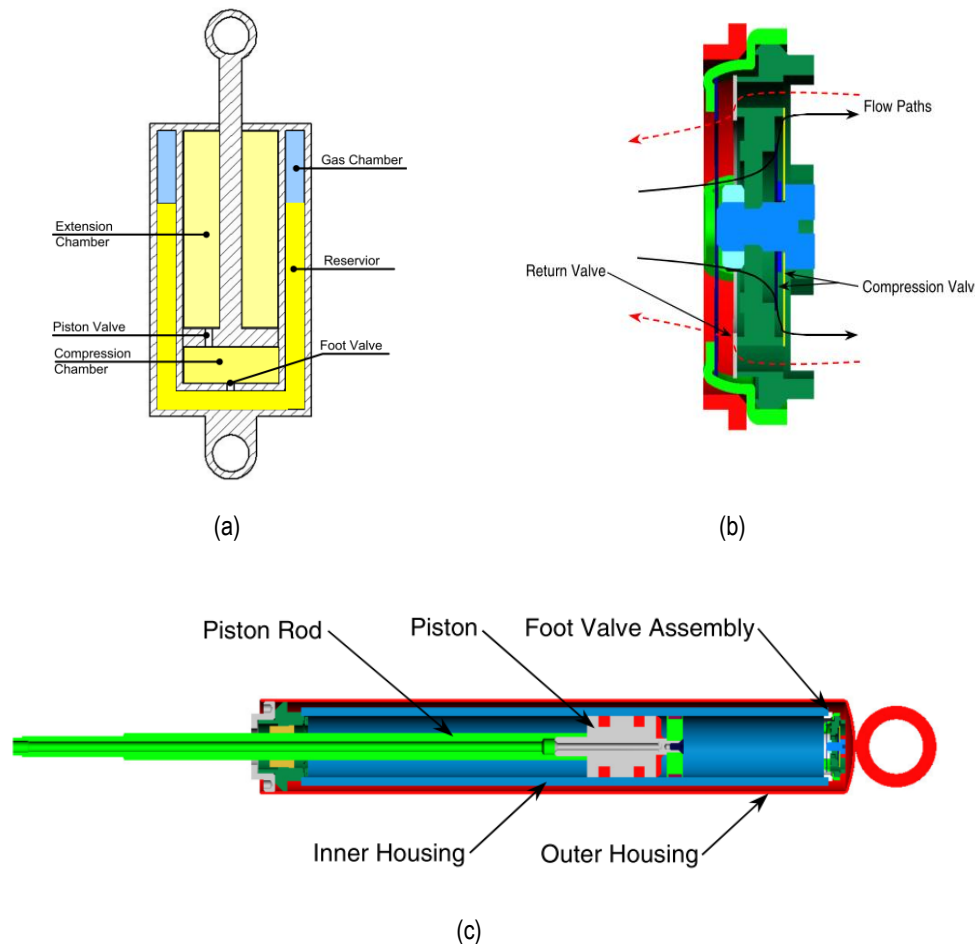


Figure 2.18 (a) conceptual structure of twin-tube[51] (b)foot valve sectional view [8] (c) section view of a twin tube damper[8].

Double-ended structure

Double-ended structure is a modification of the monotube MR damper. Figure 2.19 exhibits a double-ended MR damper. As shown in the Figure 2.19, the piston rod is extended from one end to the other with the same diameter, eliminating the need for a gas accumulator in the double-ended MR damper. As a result, the spring effect of the damper is removed. However, in some situations a compact accumulator might be used to compensate for thermal expansion of the fluid [8], [42], [53]. Some applications of this damper include gun recoil, and seismic dampers for protection in civil structures and bridges [8], [47].

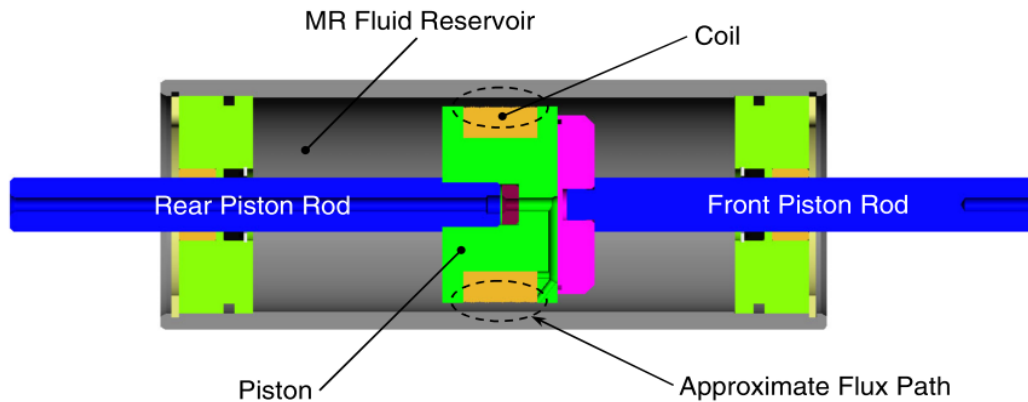


Figure 2.19 Double-end MR damper[8].

Valve structure

MR control valve is a component of MR damper that has the responsibility of generating the magnetic field, applying magnetic field to MR fluid, and control the damping force by controlling the input current. Figure 2.20 (a), (b) show a typical MR valve. Depending on the design of the valve, components may vary. In general, the valve consists of a magnetic core, a number of magnetic poles, induction coils, magnetic housing, non-magnetic bobbin, and MR fluid flow channels [48], [54]. A number of different valve configurations have been proposed in the literature which are out of scope of this review.

Application of input current to an electromagnetic coil generates an adjustable magnetic field throughout the magnetic closed path. The path consists of core, poles of MR fluid, and magnetic housing. As a result, dynamic yield stress of MR fluid can be varied; consequently, the damping force of MR damper can be altered through the input current. In the absence of the magnetic field, the damping force can be generated by viscous fluid flow through the channel [48], [55]. To achieve this, electromagnetic coils are placed inside the moving valve, known as internal coil Figure 2.20(a), or located on the outside of the cylinder, called external coil Figure 2.20(b). The direction of exposure of MR fluid to the applied magnetic field differs based on orientation of coils and MR channel. Higher dynamic pressure range, faster control response, and less leakage could be achieved using internal coil[17], [48]. Due to these advantages, only designs with internal coil are investigated in this report. In designing electromagnetic coils, the number of turns and wire gauge are important [56].

The magnetic core, poles, and housing are usually fabricated from materials with high magnetic permeability, to be able to amplify induced magnetic field; low coercivity, to achieve quick response time by dispersing magnetic field quickly; and high saturation magnetization, to allow achievement of greater magnetic flux density. Dimensions of core, poles, and housing; the number of poles and the number of coils, have significant effect on the amount of induced magnetic field [3], [48], [57].

Another main component of control valve is the MR flow channel, known as gap size. Certain designs with different number of coils and different configurations of the magnetic circuit have been presented in the literature. The gap size can be considerably change, both in the „off“ state and „on“ state. An increase in the gap size highly reduces the „off“ state force, or passive force; since an increase in the gap size means that MR fluid can easily flow through the channel. Therefore, in order to achieve a desired passive force, the gap size cannot be selected too large. Also, a large gap size reduces the maximum „on“ state force, or active force as well [56]. To maximize the effectiveness of the MR damper, the amount of active force, and hence the dynamic force range, should be large. Consequently, small gap sizes are required [42]. Very small gap sizes can result in plug of the orifice, due to film effect of the oil [58], [59]. In damper applications, gap sizes between 0.5~2 millimetres have been reported [3], [37], [48], [56].

In any procedure with hydraulics involvement, sealing plays an important role to contain fluid inside the damper. In order to prevent leakage, a set of non-corrosive, highly resistive O-rings and rod wipers should be utilized. Linear shaft bearings prevents any non-axial movement of the rod which aligns the piston head with the outer cylinder[60].

Single coil valves

A common commercial MR damper is shown in Figure 2.21(a). The valve consists of a magnetic core, two poles, and an internal coil between the two poles. The valve is placed inside the moving piston. Different modes of MR fluid can be employed here, valve mode or shear mode; if a magnetic field outside cylinder is used. Hence, the magnetic path is closed between magnetic core, poles, and cylinder. In this case, the shear mode of MR damper creates the pressure drop as shown in Figure 2.21(b). Another configuration of the valve utilizes a sliding magnetic tube inside the cylinder,

which is attached to the magnetic core and poles. The MR gap is constructed between magnetic poles and the magnetic tube in Figure 2.21(c). Since the tube and poles slide with the same velocity, MR fluid will flow similar to a valve. Lighter non-magnetic materials, such as aluminum, can be utilized instead of steel. Therefore, this configuration is more favorable in lightweight applications such as mountain bicycles.

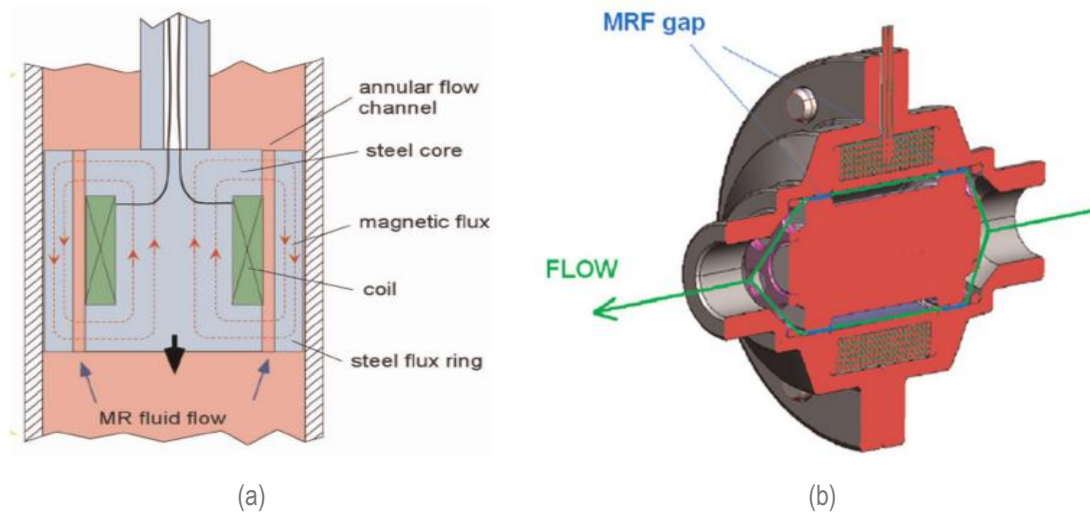


Figure 2.20 (a) Typical control valve of MR damper[48] (b) MR damper with external stationary coil[17].

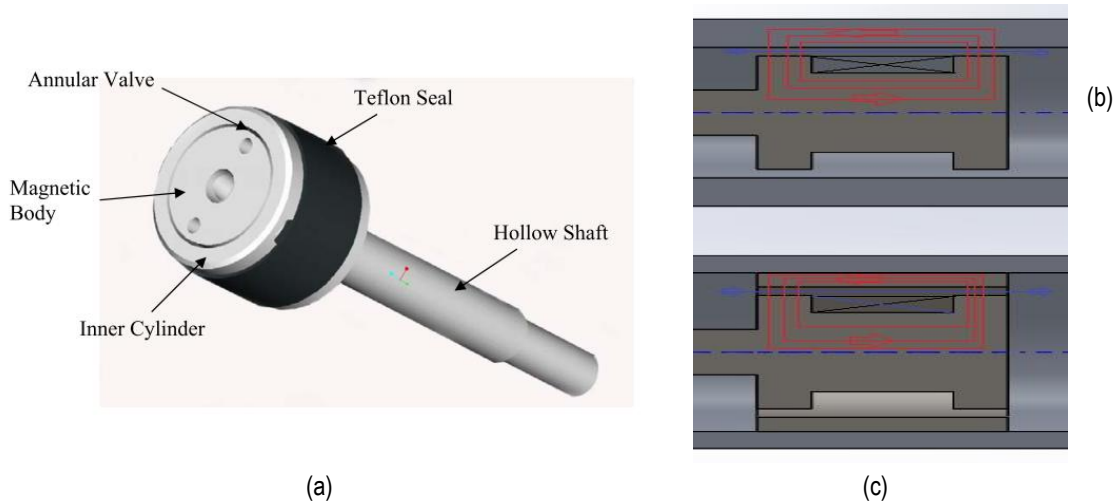


Figure 2.21 (a) Single coil valve mode MR damper[88] (b) Single coil valve in shear mode (c) Single coil valve in valve mode.

Multi coil valves

Active force or MR force is highly dependent on the area by which the MR fluid is under influence of the magnetic field, known as the active region or choking region. Multi-coil dampers have been developed [42] with longer active regions and relatively high damping forces as shown in Figure 2.22(a). As it can be seen in Figure 2.22(b), the total active area is dependent on $L_{pole (total)} = L_{pole (1)} + L_{pole (2)} + \dots$. Thus larger gap sizes can be designed, due to additional activation regions, which increases the controllability and dynamic range of the device [42], [56].

In the design of a multi-stage or multi-coil valve one should consider that, for the magnetic fields not to cancel each other, the coils should be alternately wound that their induced magnetic fields added up [8]. Another consideration is parallel connection of electromagnetic coils for achieving faster response times [42]. Finally, magnetic saturation should be considered [39]. Multi-stage or multi-coil valves are fairly heavier than single coil valves due to more magnetic material used in their structure.

Perpendicular coil axis valve

A novel MR fluid damper was presented in [53] which increases the choking region significantly, and consequently provides a higher yield stress. Figure 2.23(c), shows major components of this design. Coils are wound perpendicular to the flow axis, in contrary to other designs, around a magnetic core as shown in Figure 2.23(b). The magnetic path is completed between magnetic core and poles, outside cylinder as

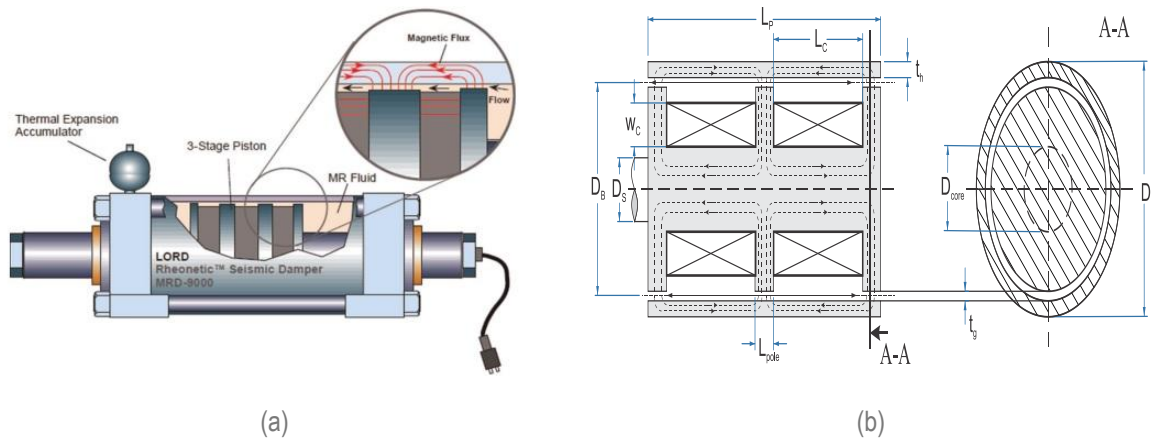


Figure 2.22 (a) Multi coil MR damper [42] (b) schematics of double coil MR damper.

shown in Figure 2.23 (a) [52]. The advantage of this coil alignment is that almost all the cylindrical orifice is exposed to the magnetic field instead of a small L_{pole} in other designs. The result is higher controllability, lower power consumption, and faster response time. Overall, the length of the piston can be reduced, since all length of piston is considered to be in the active region [48].

Different numbers of magnetic poles were proposed. The reported results indicate that four poles can increase the damping coefficient up to three times using 2 Amp currents. Furthermore, eight magnetic poles allow the damper to reach the same damping with 1 Amp current input. In fact, eight poles allow an optimum capacity in various frequencies [48]. In order to reduce the eddy current produced on the surface, core and poles are constructed from welding of numerous metal sheets and washers [52]. Complexity of the core and poles design makes them more costly. Furthermore, sealing is reported to be a major challenge due to complexity of the design [48], [52].

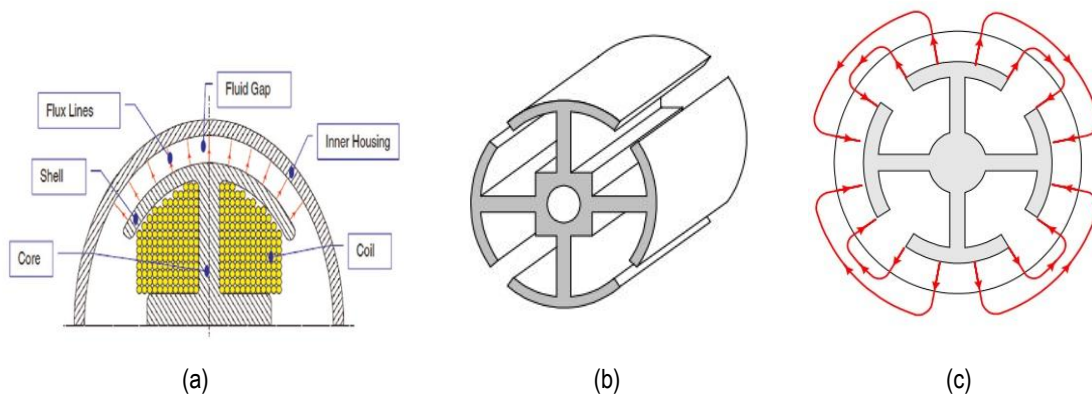


Figure 2.23 (a) Components of perpendicular coil axis configuration (b) core structure (c) Magnetic field path in perpendicular coil axis configuration [52].

Valve with both annular and radial flow channel

Increase in the input current and flow volume are the most common ways of increasing the damping force in MR dampers. In an innovative design, the authors in [59] proposed a damper with both annular and radial flow channels, to generate damping forces without changing power consumption or size of the flow channel. Figure 2.24(a) shows the schematics of this damper in which the fluid flow path is shown in Figure

2.24(b). By increasing the length of flow channel and increasing the active area, damping forces can be considerably elevated and made highly adjustable. Annular-radial designs reach saturation under larger induced flux through magnetic body when compared to annular dampers [54].

As it can be seen, the magnetic flux is applied normal to flow direction at all-time. The produced pressure drop is a summation of annular pressure drop, consisting of a viscous component and a field-dependent induced yield stress component; and radial pressure drop, due to conflux mode flow, headstream mode flow, and field dependant radial flow [10], [54], [59]. High force applications such as seismic systems in structural engineering usually utilize annular-radial dampers [48], [54].

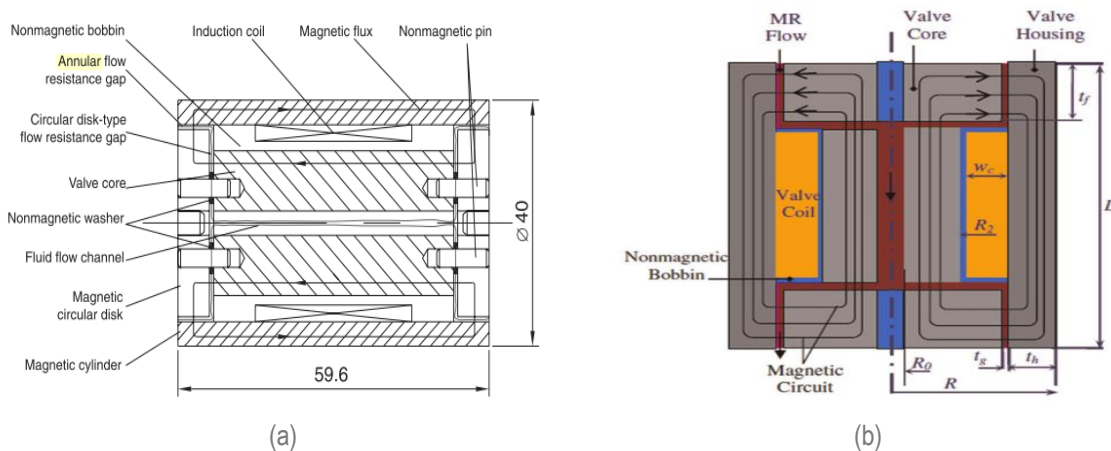


Figure 2.24 (a) Detailed schematics of valve with both annular and radial flow channel [59] (b) Flow path and magnetic field of damper [48].

Fail-safe MR dampers

Failure of electronics, electrical power loss, faulty electrical wires, and disrupted control circuits can cause MR dampers to fully lose input current. As a result, no magnetic field will be induced and the active portion of damping force will vanish. In typical MR dampers, the entire active force is generated by an electromagnetic coil. Therefore, any electrical failure, including no current or constant current lock, causes significant abnormalities in the damping coefficient. To overcome the above problems, innovative fail-safe designs have been proposed such as an inner bypass magneto-

rheological damper with magnetic bias [61], a bidirectional controllable MR fluid valve [62], and MR dampers with hybrid magnetic circuit designs [55].

Bose *et. Al* [55] designed and fabricated a hybrid damper by implementing a series of permanent magnets in three stages. In the first stage, a couple of rare earth permanent magnets, Neodymium was implemented at both ends of magnetic poles (dark areas in Figure 2.25(a)). The permanent magnet constantly generates a magnetic field to the MR fluid channel. In case of failure of the electromagnet, the shear stress that permanent magnet generates, prevents the system from failing. The electromagnet can strengthen or weaken the permanent magnet field. The components of magnetic system are then designed to even out the effect of the permanent magnet [48], [55].

In the second stage, an AlNiCo permanent magnet was implemented in the center of the magnetic core. AlNiCo has a high magnetic remanent flux, low temperature coefficients, and is low cost. However, it has a low coercive force and exhibits an extremely non-linear demagnetization curve. Magnetization of the AlNiCo can be changed by short pulses of the coil current; therefore, it works similar to a magnetic

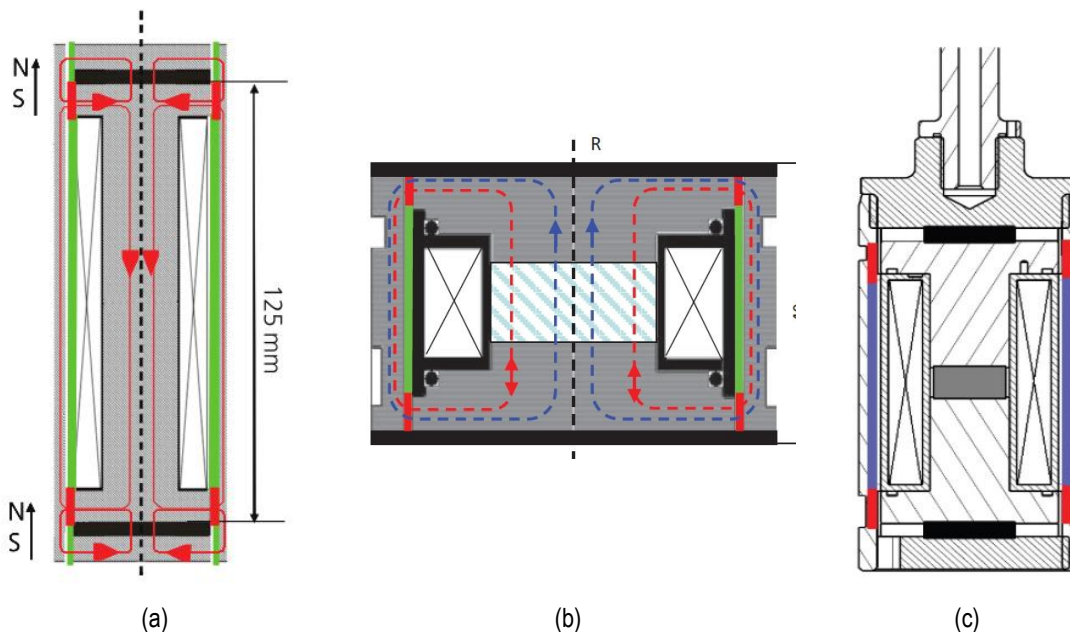


Figure 2.25 (a) Implementation of permanent magnets in poles of MR damper only (b) magnetic core structure with permanent magnet (c) fail-safe hybrid damper with permanent magnets inside core and poles [55].

latch, resulting in different magnetic flux densities and damping forces without permanent electric energy consumption[55]. Figure 2.25(b) displays this configuration and the relative magnetic field.

Another concept is the combination of the above three magnetic sub-circuits, such that all magnetic fluxes superpose in the MR fluid flow channel as depicted in Figure 2.25(c). Theoretical and experimental results indicate great improvements in terms of achieving a wide range of damping forces and significant reduction in power consumption [55].

2.2.2. MR damper modeling

MR dampers exhibit inherently hysteretic and highly nonlinear dynamics. Such behavior makes the modeling of MR dampers very challenging. In order to characterize the performance of MR dampers, several models have been proposed [63]. The proposed models must be accurate, meaning that the output of the predicted model and experimental data should converge. The model must also be simple to allow easy parameter identification and less complex controllers, and finally be reversible, meaning that different input and outputs can be selected [64].

.In general, models can be categorized according to the properties that they represent, such as velocity profile, shear stress of MR fluid, or according to modeling methods that describe the behavior of MR damper. Models based on the properties of MR dampers can be divided into two main categories: Quasi-static models and dynamic models. Another group of models are the ones that match the behavior of MR damper with physical or mathematical models, which can be categorized as parametric dynamic model and non-parametric dynamic models [64].

Quasi-static models

Quasi-static analysis of MR fluid flowing through an annular duct under a constant velocity and fully developed fluid flow is based on deriving a physical model [42], [48]. A relatively accurate model for predicting an MR damper behavior is the axisymmetric model. Approximate models such as parallel plate model and non-

dimensional parallel plate model have been proposed [48]. In order to predict the design concept prior to prototyping, non-dimensional models were presented in [65].

Axisymmetric models

The rheological models of field dependent MR fluids, or constitutive models, are employed in asymmetrical method. This method analyzes velocity dependent damping forces, due to the pressure drop through the flow gap, when force is applied to the shaft of the damper. Previously, Kamath *et al.*[66], and Gavin *et al.*[67] used quasi-static axisymmetric analysis to model a proposed damper. Gavin *et al.* assumed that yield stress satisfied an inverse power law[67]. Kamath *et al.* assumed constant yield stress in the annular gap when studying the MR fluid shear thinning/thickening effects [48]. Wang and Gordaninejad [68] proposed an axisymmetric model for a large scale MR damper, the using Herschel-Bulkley model of MR fluid [48].

The general force equilibrium, Navier-stoke, equation governing this mechanism is [66]:

$$\rho \frac{\partial u}{\partial t} + \frac{\partial \tau}{\partial r} + \frac{\tau}{r} = \frac{\partial p}{\partial z} \quad 2.25$$

where u is the velocity, τ is the shear stress, r is the radial coordinate, z is the longitudinal coordinate, and p is the developed pressure due to the piston head motion. The fluid density is denoted by ρ [66]. Since the analysis is quasi-static, the inertia term is neglected and it is assumed that pressure changes linearly along the length of the flow cap. Therefore, equation can be reduced to:

$$\frac{d\tau}{dr} + \frac{\tau}{r} = \frac{\Delta P}{L} \quad 2.26$$

where, ΔP is the pressure drop along flow channel, L is length of flow channel, and r is the gap size

Generally, we assume that MR fluid is resisting flow until shear stress level passes the controlled yield stress as described by Equation 2.15[42], [48]. For a

cylindrical piston with an annular orifice, using Bingham plastic model analysis and boundary conditions indifferent regions of Figure 2.12(b) and Figure 2.13 (b), the velocity profile and flux volume of each region can be obtained. The total volume flux of MR channel is obtained by adding volume flux of all flow regions. Since, the volume flux displaced by the piston is equal to the volume flux through the flow channel, the velocity of the piston v_0 can be determined using following:

$$v_0 = \frac{Q_p}{A_p}. \quad 2.27$$

where, Q_p is volume flux through piston, and A_p is cross section area of fluid before entering the flow channel. Finally, equivalent viscous damping C_{eq} can be expressed using damping force F and velocity of piston v_0 as [66]:

$$C_{eq} = \frac{F}{v_0} \quad 2.28$$

Following a similar procedure, different axisymmetric models can be developed, for different MR fluid models and geometrical configurations [56], [69], [70].

Parallel plate model

When the ratio between gap size and piston diameter is small, the axisymmetric model can be approximated by flow of MR fluid through two parallel duct [48], [65]. In general, an annular flow channel can be approximated by a rectangular duct with $2\pi R$ as width (R is average radius of the center of annular gap), L as length, and h as the thickness of equivalent rectangular duct [59]. A polynomial expression for pressure gradient in the flow of a Bingham fluid through a rectangular duct was initially developed by Philips [40], [42], [48]. Further simplifications for yield stress equations in the valve flow mode of MR damper results in [40], [59]:

$$\frac{dP}{dx} = \frac{dP\eta}{dx} + \frac{dP\tau}{dx} = \frac{12\eta Q}{\pi h^3 R} + \frac{c\tau_y}{h} \quad 2.29$$

where c is an empirical coefficient dependent on the velocity profile bounded to [2.07, 3.07]. The lower bound is related to no filed and higher bound to maximum current. If we integrate above equation over length of flow channel we obtain:

$$\Delta P = \Delta P_\eta + \Delta P_\tau = \frac{12 \eta Q L}{\pi h^3 R} + 2 \frac{c L_p \tau_y}{h} \quad 2.30$$

where L_p is pole length; By implementing $Q = A v_0$, $F = \Delta P A$ we can obtain [12], [47]:

$$F = F_\eta + F_\tau = \frac{12 \eta L v_0}{\pi h^3 R} A_p^2 + 2 \frac{c L_p \tau_y}{h} A_p \quad 2.32$$

For the MR damper in Figure 2.26, with given geometric parameters, the total damping force can be written as a combination of spring force induced by gas accumulator F_g , and forces due to MR effect F_τ and viscosity F_η [12], [47], [69] as follows:

$$F_g = A_s P_a = A_s P_0 \left(\frac{V_0}{V_0 + A_s x_p} \right)^\gamma \quad 2.31$$

In which P_0 and V_0 are the initial pressure and initial volume of the gas chamber, A_s is the cross sectional area of shaft, and P_a is the pressure due to gas accumulator, respectively. The parameter γ represents the coefficient of thermal expansion which varies between 1.4 and 1.7 [12]. By separating the viscose and field dependent parts, the total damping force is given by:

$$F = A_s P_a + \frac{12 \eta L}{\pi t_g^3 R_b} (A_p - A_s)^2 (x_p \dot{}) + 2c \frac{L_p}{t_g} \tau_y (A_p - A_s) \operatorname{sgn}(x_p \dot{}) \quad 2.33$$

where t_g is the gap size, $R_b = R_c + \frac{1}{2} t_g$ is the radius of an imaginary cylinder to the center of the gap, and $(x_p \dot{})$ is the piston velocity.

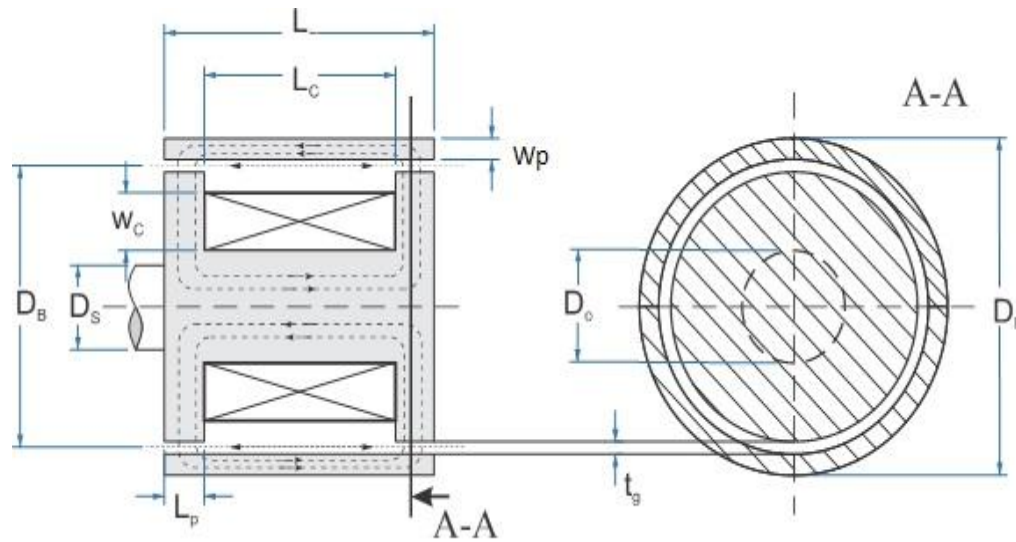


Figure 2.26 Schematics of a valve mode MR damper piston with geometrical parameters.

Dynamic models

In the initial stages of the design quasi-static models are very useful. However, they are not sufficient to explain the nonlinear behavior of MR dampers under dynamic loading [64]. Using the actual physical process analysis of MR fluids through an annular gap, various parametric and non-parametric models have been proposed [48]. Parametric modeling techniques characterize the MR damper behavior as a combination of physical elements, whereas the non-parametric modelling techniques describe MR damper test data as a series of mathematical functions [64], [71].

Parametric dynamic model

Parametric models use mechanical elements to simulate the behavior of MR damper. In order to create these models some assumptions need to be made. A series of dashpots, springs, and non-linear elements represent MR behavior. Using curve fitting techniques, the parameters of these elements can be determined [64], [72]. Several parametric models have been proposed including the Bingham model [73], [74], bi-viscous models [65], [73], viscoelastic-plastic models [65], [75], Bouc-wen hysteresis model [74], [76], and modified Bouc-wen (Spencer) model [74], [77]. In the following, some of these models are explained in further detail.

Bingham dynamic model

Bingham model for MR dampers was proposed by Stanway *et al.*[78], which consists of a Coulomb friction element f_c placed in parallel with a viscous dashpot c_0 , as shown in Figure 2.27(a). For nonzero piston velocities \dot{x}_p , damping force F_d can be calculated from [74]:

$$F_d = f_c \operatorname{sgn}(\dot{x}_p) + c_0 \dot{x}_p + f_0 \quad 2.34$$

In above formula, f_0 is the simplified force due to the presence of an accumulator. This simplification is if we neglect the spring effect of gas chamber. Bingham body model added this spring effect to Bingham model. This model is shown in Figure 2.27(b) The Bingham body model combines three elements: St. Venant (plastic body model), Newton (Newton flow model), and Hook's law (elastic body model). For low shear forces, the model works as solid body, when shear stress exceeds yield stress, MR shows liquid behavior. This behavior is shown In Figure 2.27(c)[79]. The damping force for Bingham body model can be expressed as:

$$F_d = \begin{cases} f_c \operatorname{sgn}(\dot{x}_p) + c_0 \dot{x}_p + f_0 & \text{for } |F_d| > f_c \\ k(x_2 - x_1) + f_0 & \text{for } |F_d| \leq f_c \end{cases} \quad 2.35$$

where the term k represents the stiffness of the elastic body.

Bouc-wen and Spencer dynamic models

The Bouc-Wen model is a differential hysteresis model commonly used to represent the damping force of MR dampers. The Bouc-Wen model is numerically tractable, extremely versatile, and adequately represents a wide variety of hysteretic behaviours. Spencer [75] has used the Bouc-Wen model, as shown in Figure 2.28(a), to analyze the nonlinear hysteresis behaviour of an MR damper.

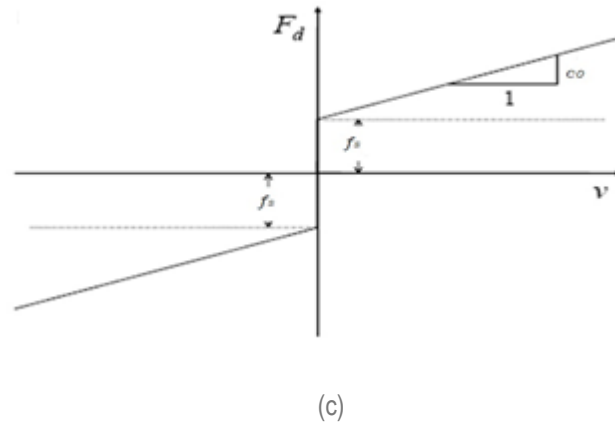
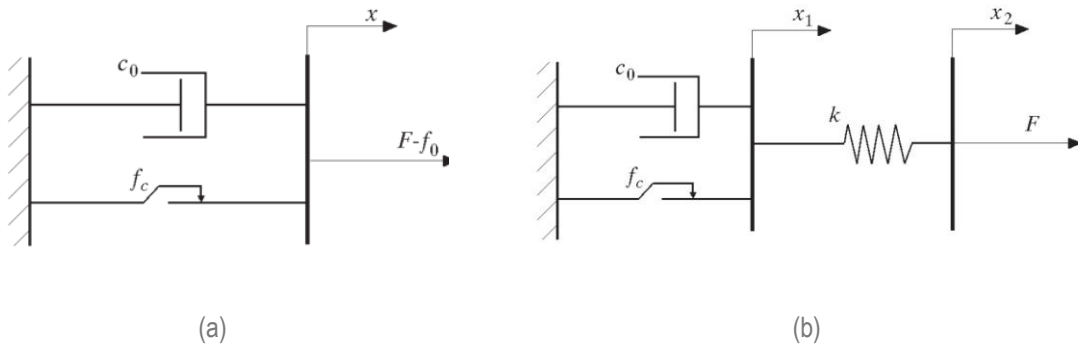


Figure 2.27 (a) Bingham model (b) Bingham body model (c) Bingham and Bingham body model Force-velocity curve.

The damping force is given by:

$$F_d = k_0 (x - x_0) + c_0 \dot{x} + \alpha z(t, x) \quad 2.36$$

$$\dot{z} = -\gamma |\dot{z}| z |z|^{n-1} - \beta \dot{x} |z|^n + A \dot{x} \quad 2.37$$

where F_d is the damping force provided by damper; force f_0 can be the corresponding force for an initial deflection x_0 of spring k_0 ; and $k_0, c_0, \alpha, \gamma, \beta, A$, are experimental parameters of the model, z is a rotational variable, x is the displacement of damper shaft; and \dot{x} is the velocity of the piston [47].

Spencer *et al.*[75] proposed a modified version of Bouc-wen model to describe the nonlinearities more clearly. The model was expanded by adding a dashpot, represented by c_1 , to exhibit the roll-off at low velocities and a spring k_1 to compensate for the effect of the gas chamber [72], [75]. Figure 2.28 (b) represents the Spencer model. The damping force of Spencer model can be calculated using:

$$\begin{cases} \dot{z} = -\gamma|\dot{x} - \dot{y}|z|z|^{n-1} - \beta(\dot{x} - \dot{y})|z|^n + A(\dot{x} - \dot{y}) \\ \dot{y} = \frac{1}{c_0 + c_1}\{k_0(x - y) + c_0\dot{x} + \alpha z(t, x)\} \\ F_d = c_1\dot{y} + k_1(x - x_0) \end{cases} \quad 2.38$$

where, k_0 is used to control the stiffness at larger velocities, and x_0 is the initial displacement of spring k_1 associated with the nominal damper due to the accumulator. Furthermore, z is a revolute variable and F_d is the predicted damping force.

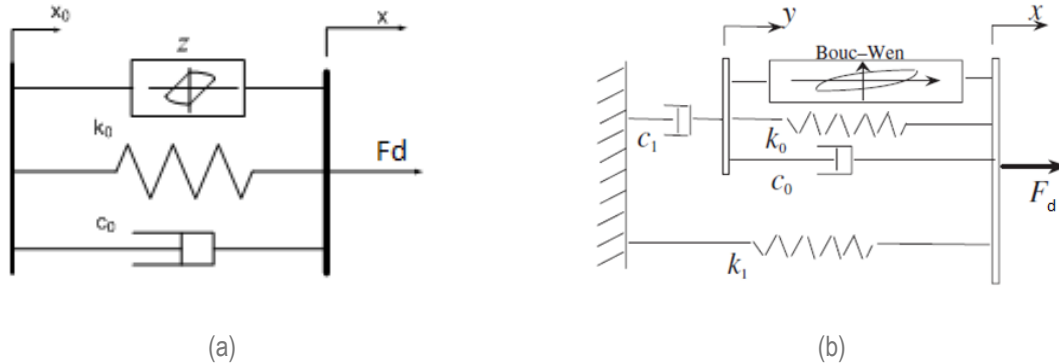


Figure 2.28 (a) Bouc-wen model for MR damper (b) Spencer model for MR damper [75].

Non-parametric dynamic model

Unlike parametric models, non-parametric models do not describe the MR damper behavior based on input/output relationship of the system. Basically, non-parametric models use analytical expressions to express the behavior of MR dampers. These models consider both experimental data and device physics [65], [73].

Non-parametric models can be categorized as interpolation techniques and neural-based methods [73]. The various models developed include polynomial [80], multi-function [72], black-box [78], neural network [81], and fuzzy [82].

2.3. Conclusion

In this chapter we studied characteristics of MR fluid along with its modeling techniques and its application in MR damper designs. To this end, rheology basics and rheology properties of MR fluids were discussed followed by MR fluid models and modes of operation. Models for MR dampers were studied along with their applicability to damper design.

Chapter 3. Experimental comparison of MR and conventional dampers

To investigate the feasibility of using MR dampers in mountain bicycle applications, a series of comparisons were performed between using an MR damper and conventional dampers. In downhill biking, the shock absorber should be tuned to provide a smooth ride over a high frequency range with low amplitude bumps. In this process, the bicycle should not lose traction. Furthermore, the bicycle should handle situations when a large bump is encountered or "bottom out" of the shock absorber. The shock absorber should also recover fast enough to quickly absorb high frequency bumps and prevent loss of traction. Consequently, controllability and low power consumption of MR damper combined along with comfort and safety are important issues to consider in the design of the suspension. In this chapter we study if the damping levels expected in a typical mountain bike can be achieved using a MR damper.

3.1. Feasibility Testing

To be able to perform high force, and high precision tests on dampers, a hydraulic shaker is utilized. The dampers are connected to a hydraulic shaker using a suitable attachment setup built in our lab. Tests were performed on both systems and the acquired data was used to obtain the force vs. displacement and force vs. velocity plots. By comparing the performances of MR damper with conventional dampers in different operating modes, it is proven that MR dampers are a potential candidate to be used in downhill bicycles. The test mechanism structure, data acquisition process, and result analysis are explained in subsequent sections.

3.1.1. Test mechanism

To evaluate the feasibility of using MR dampers in mountain bicycle suspension systems, we need to compare their performances with the conventional bicycle shocks. For this purpose, the same set of vertical displacement inputs have to be applied to MR dampers and conventional bicycle shocks followed by a measurement of force response for different velocity and displacement profiles. The test mechanism should be powerful enough to provide high speed excitations. In this work, we used a MTS 248.03s hydraulic actuator shown in Figure3.1(a) available at Simon Fraser University Mechatronics department. This system is originally designed to simulate road conditions for mid-size vehicle suspension systems. Its main actuator can apply up to 25kN (25000 Newton) and is equipped with an internal LVDT sensor to record the displacement data. The hydraulic shaker is highly accurate and controllable in terms of displacement, applied force, acceleration, and applied torque. A MTS 661.19f-04 force transducer shown in Figure3.1 (b) was also utilized in series with the shocks to capture the force response. The actuator is controlled by a MTS FlexTest 40 digital controller machine shown in Figure3.1(c), which can work in either displacement control or force control modes. Based on the application, different types of force or displacement excitations can be implemented. Profiles including ramp, sinusoidal, triangular, or even a set of data representing the road profile can be generated using this powerful controller.



(a)



(b)



(c)

Figure3.1 (a) Hydraulic shaker, (b) Force transducer, (c) Digital controller.

The required adaptors and connectors were designed and fabricated so that each shock can be easily connected to the hydraulic actuator. Furthermore, the shocks can be substituted for different testing procedures. Figure 3.2 shows the fabricated setup

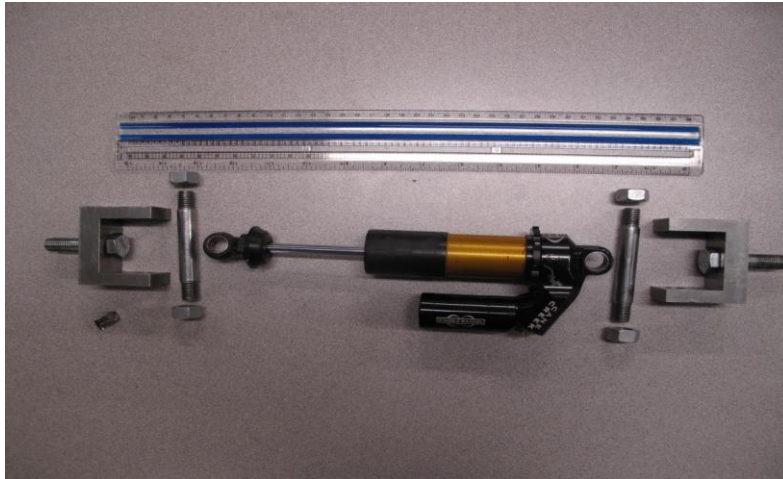


Figure 3.2 Fabricated connector to attach dampers to the hydraulic shaker.

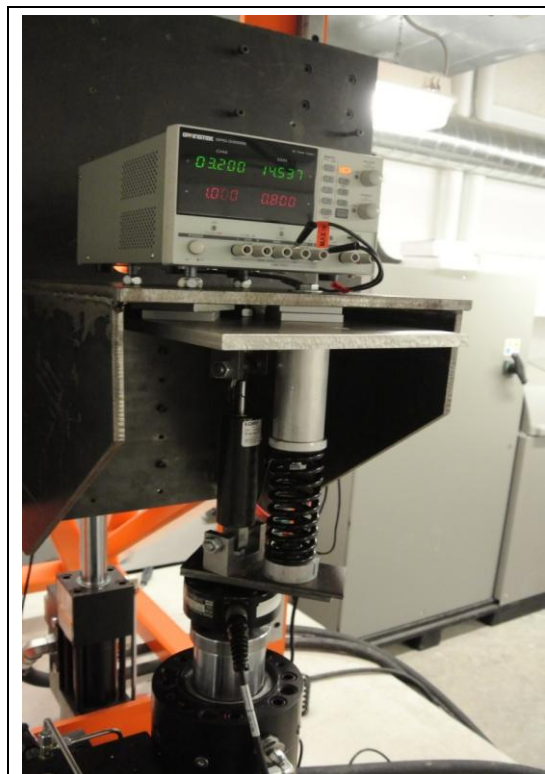


Figure 3.3 Test mechanism components, while testing MR damper in parallel with coil spring.

to connect dampers to the hydraulic shaker. All parts are made of cast steel for high tensile stress and durability.

Figure 3.3 exhibits the components of the designed test mechanism during a test procedure. The top parts of the shocks are fixed to the ground and the lower part is excited using the hydraulic actuator. A coil spring is located parallel to the MR damper. A power supply is utilized to provide necessary input current to MR damper. The force transducer is attached in series with actuator to record displacement and force data.

3.1.2. *Damper selection*

In downhill biking, metal coil springs are usually preferred over air springs. The main reason is due to the non-linear behavior of air springs and the fact that coil springs show both higher and more predictable damping. In this study, three different conventional mountain bicycle dampers with coil spring are tested. The selection of dampers was based on dynamic behaviors. The first tested damper referred to as (D1) in this report is a Fox Van R damper from Fox Corporation shown in Figure 3.4 (a). It has only a rebound circuit with one knob for adjusting the damping force during the rebounds. The second one, referred to as (D2), is a Fox Van RC damper from Fox shown in Figure 3.4 (b). This damper is equipped with both rebound and compress circuits. The two knobs on this damper enable us to regulate the damping force in rebound and compression directions as desired. Finally, the last mountain bicycle damper, referred to as (D3), used in this study is a Double Barrel damper from Cane Creek 2013 shown in Figure 3.4 (c), which is known as one of the most advanced dampers in the market. With its twin tube damping technology, this damper provides highly controllable, independent damping for both compression and rebound strokes. The double Barrel damper has four knobs including low-speed compression, high-speed compression, low-speed rebound, and high-speed rebound knobs; which can be adjusted entirely independent of each other.

The goal of this study is to evaluate whether it is possible to replace the above mentioned conventional dampers with semi-active MR dampers. The first step toward this goal is to provide a preliminary comparison between conventional bicycle dampers and MR dampers available in the market. For the experiments, a commercial RD-8040-1

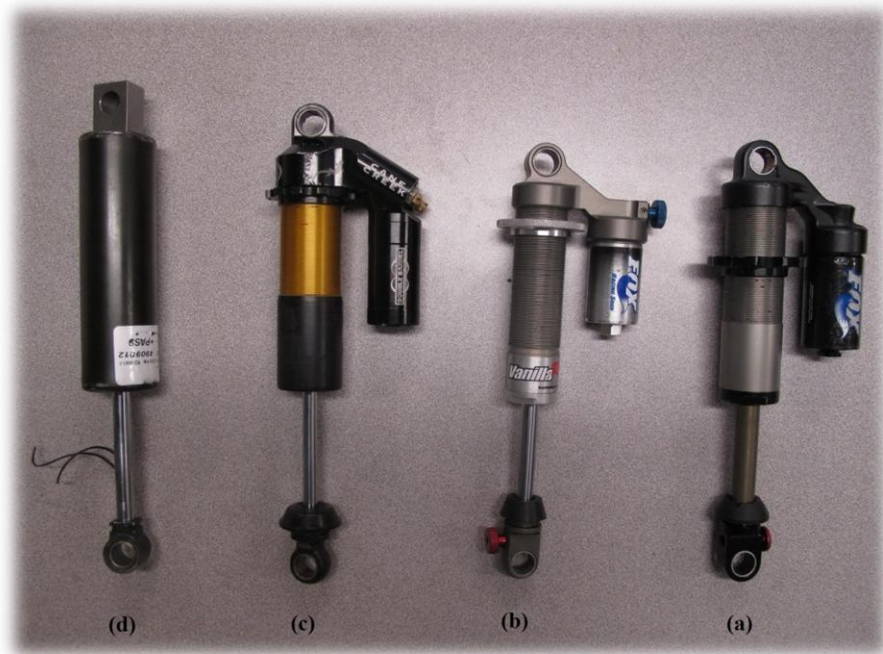


Figure 3.4 Tested Shocks: (a) Fox Van R (D1), (b) Fox Van RC (D2), (c) Cane Creek Double Barrel (D3), (d) Lord Corporation MR damper.

MR damper manufactured by the Lord Corporation was utilized. This damper has almost the same dimensions and stroke length (≈ 56 mm) as the selected bicycle dampers. Figure 3.4 (d) shows the Lord MR damper used in this study.

3.1.3. Test procedure and guidelines

To compare the MR damper with a conventional mountain bicycle shock, a series of tests are conducted to measure the response of the MR damper under various combinations of frequencies $f = \frac{\omega}{2\pi}$, amplitudes of damper stroke x_a , and current supply i_c . The performances of both conventional bicycle dampers and MR dampers can be considerably different if the testing conditions change significantly. For example, it is a well-known fact that the efficiency of dampers drops at high temperature. To avoid unwanted effects and ensure data consistency, the following considerations were taken into account

General Guidelines for testing all the dampers:

- I. The testing is stopped if temperatures exceeded 85° C.
- II. The testing is stopped if the force exceeds 5500 Newton to ensure that the tests will not damage the testing machine. In order to avoid hitting the ends of the strokes and damaging the shocks, the maximum travel of the excitations ($2 \times 23 \text{ mm}$) is set to be less than damper's full stroke ($\approx 2 \times 28 \text{ mm}$).
- III. As recommended by Fox Inc., speed limits should be considered during heavy compression and heavy rebound damping tests. For each of the selected damper settings. Sinusoidal displacement inputs with frequencies of 0.5, 1, 2, 4 and 6 Hertz, and amplitudes of 3, 8, 13, 18 and 23 millimetres, are applied to the dampers which gives us a maximum speed of 0.867 m/s.

Guidelines for testing conventional dampers (D1, D2, and D3):

- I. In order to avoid the cross coupling effect of compression and rebound adjustments, only one circuit is tested at a time (Rebound circuit is set to be fully open when testing the compression circuit and vice versa).
- II. The rebound circuit should never be fully closed (i.e., the rebound knob should always have backed off at least two clicks from the fully closed state). Therefore, each of conventional bicycle dampers are first tested under fully open compression and closed rebound (two clicks out from fully closed). In the next step, they are tested under fully open rebound and compression closed state (two clicks out from fully closed state).

Guidelines for testing the MR damper

- I. The damper coil has a 1 and 2 amperes current limits for continuous (up to 30 seconds) and instant working modes, respectively. Therefore, to prevent the coils from burning up, the damper is tested for current values up to a maximum of 0.80 amperes.
- II. For each frequency-amplitude pairs of displacement excitation, the MR damper is tested under the applied current varying from 0.20 to 0.80 amperes in increments of 0.20 amperes.

For each experiment, the machine controller is programmed to apply 15 complete cycles of sinusoidal excitation to the dampers. The machine's data acquisition system records forces and displacement of the actuators at a rate of 256 Hz. The velocity of the damper piston can also be obtained via a derivative of displacement.

In this research, three different groups of experiments are carried out with the results presented in the following sections. The overall performance of the suspension system is determined by the force contributions of its two main elements: the damper and the spring. Each of D1, D2 and D3 dampers has a parallel coil spring component with different spring constants; however, the MR damper does not have any spring attached to it. Therefore, to have a fair comparison, we decided to cancel the effects of coil springs on the produced forces. In the first series of the experiments, all the coil springs were removed and tests performed on D1, D2, D3 and MR dampers without the springs.

In the first set of experiments, a large number of tests were performed on all four test dampers over wide range of frequencies and amplitudes of input displacement. Table 3.1 shows all test scenarios performed on the dampers. Damper D1 was not tested above 2 Hz and damper D2 was not tested above 4 Hz due to safety precautions and limitation set by the manufacturer. During this group of tests, the damping characteristics of each damper without external spring effect were also evaluated.

Table 3.1 All performed tests, over a wide range of input displacement profiles.

		Amplitude= 3 mm	Amplitude= 8 mm	Amplitude= 13 mm	Amplitude= 18 mm	Amplitude= 23 mm
MR Damper	Current = 0 amp	0.5 Hz	0.5 Hz	0.5 Hz	0.5 Hz	0.5 Hz
	Current =0.2 amp	1 Hz	1 Hz	1 Hz	1 Hz	1 Hz
	Current =0.4 amp	2 Hz	2 Hz	2 Hz	2 Hz	2 Hz
	Current =0.6 amp	4 Hz	4 Hz	4 Hz	4 Hz	4 Hz
	Current =0.8 amp	6 Hz	6 Hz	6 Hz	6 Hz	6 Hz
Fox Van R Old	Fast Rebound	0.5 Hz	0.5 Hz	0.5 Hz	0.5 Hz	0.5 Hz
		1 Hz	1 Hz	1 Hz	1 Hz	1 Hz
	Slow rebound	2 Hz	2 Hz	2 Hz	2 Hz	2 Hz
		-	-	-	-	-
Fox Van R New	Fast Rebound	0.5 Hz	0.5 Hz	0.5 Hz	0.5 Hz	0.5 Hz
	Slow Compression	1 Hz	1 Hz	1 Hz	1 Hz	1 Hz
	Slow Rebound	2 Hz	2 Hz	2 Hz	2 Hz	2 Hz
	Fast Compression	4 Hz	4 Hz	4 Hz	4 Hz	-
Cane Creek	Fast Rebound	0.5 Hz	0.5 Hz	0.5 Hz	0.5 Hz	0.5 Hz
	Slow Compression	1 Hz	1 Hz	1 Hz	1 Hz	1 Hz
	Slow Rebound	2 Hz	2 Hz	2 Hz	2 Hz	2 Hz
	Fast Compression	4 Hz	4 Hz	4 Hz	4 Hz	4 Hz
		6 Hz	6 Hz	6 Hz	6 Hz	6 Hz

The second group of tests were performed using a Fox shock (300lbx3.0). In coil springs the first number represents the spring rate and the second number represents the maximum stroke (or spring compression at shock bind in Fox's case). For the second group of tests, only the MR damper and Cane Creek shock were used as test objects. The objective is to verify whether the MR damper has the capability to match the performance of more advanced shocks. Considering the amount of force that a coil spring adds displacement tests were performed using input sinusoids with amplitudes of 8mm and 13mm and frequencies of 2Hz, and 4Hz, respectively. Table 3.1 shows all second group test scenarios in dark color.

The last group of tests performed at this stage were investigating the result of temperature changes on the performance of the MR damper. Since this effect was not of great value at the initial stages of the project; not too many accurate tests were performed.

3.2. Analysis of results

The force vs. displacement and force vs. velocity plots were used to study the performance of various shocks tested Figure 3.5 shows four key positions of experiments on force vs. displacement curve for a conventional bicycle damper. In this figure, BDC and TDC refer to bottom dead center (maximum damper length) and top dead center (minimum damper length) of the excitation travel, respectively, while the M points during compression and rebound, indicate the point at which the shock reaches peak velocity. The experiments on force vs. displacement and force vs. velocity plots start at zero velocity at BDC. It then follows the curve in counter clockwise and clockwise directions, respectively.

The actuator compresses the shock from low speed (0.0 m/s) at point BDC and then accelerates until the maximum velocity is reached at point M. The compression decelerates from point M to point TDC where shocks reach zero speed again. The shock rebound can be seen on the plot starting at point TDC which accelerates to the maximum speed at the mid-stroke. From here, the shock rebound circuit is under deceleration until BDC is reached.

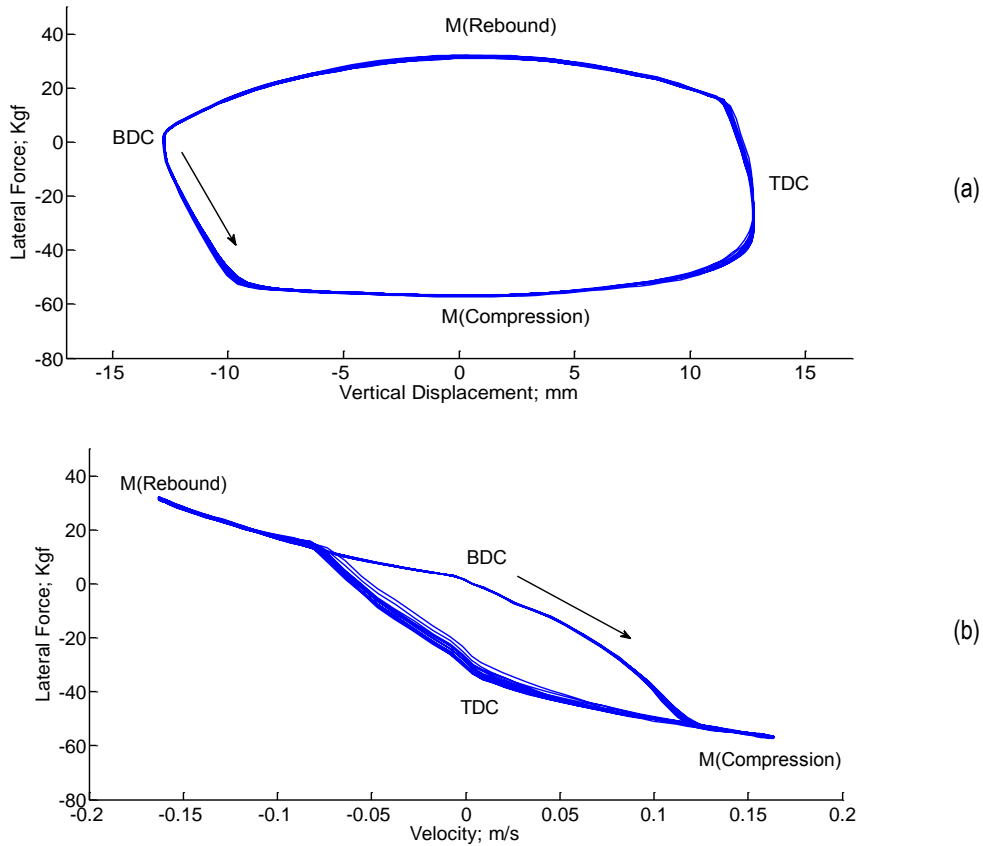


Figure 3.5 Experimental results (a) the force-displacement curve for a conventional bicycle damper (b) the force-velocity curve for a conventional bicycle damper.

3.2.1. Data acquisition and Performance evaluation

After performing the tests, all acquired data were converted and altered into MATLAB format. Using the MATLAB filter toolbox, a low pass filter was designed and applied to the input signal. A code was developed to read appropriate data from relative folders and calculate velocity and obtain the force vs. displacement and force vs. velocity curves. Afterward, a series of different scenarios were chosen to illustrate the performance of the dampers. The results of these scenarios are shown in in Appendix A. A summary of the results obtained are described in the following sections.

Effect of input stimuli amplitude on performance

Generally speaking, a larger input amplitude results in higher damping forces. Increasing the amplitude affects both rebound and compression, resulting in wider force

vs. velocity hysteresis loop. The area inside force vs. displacement loop determines the

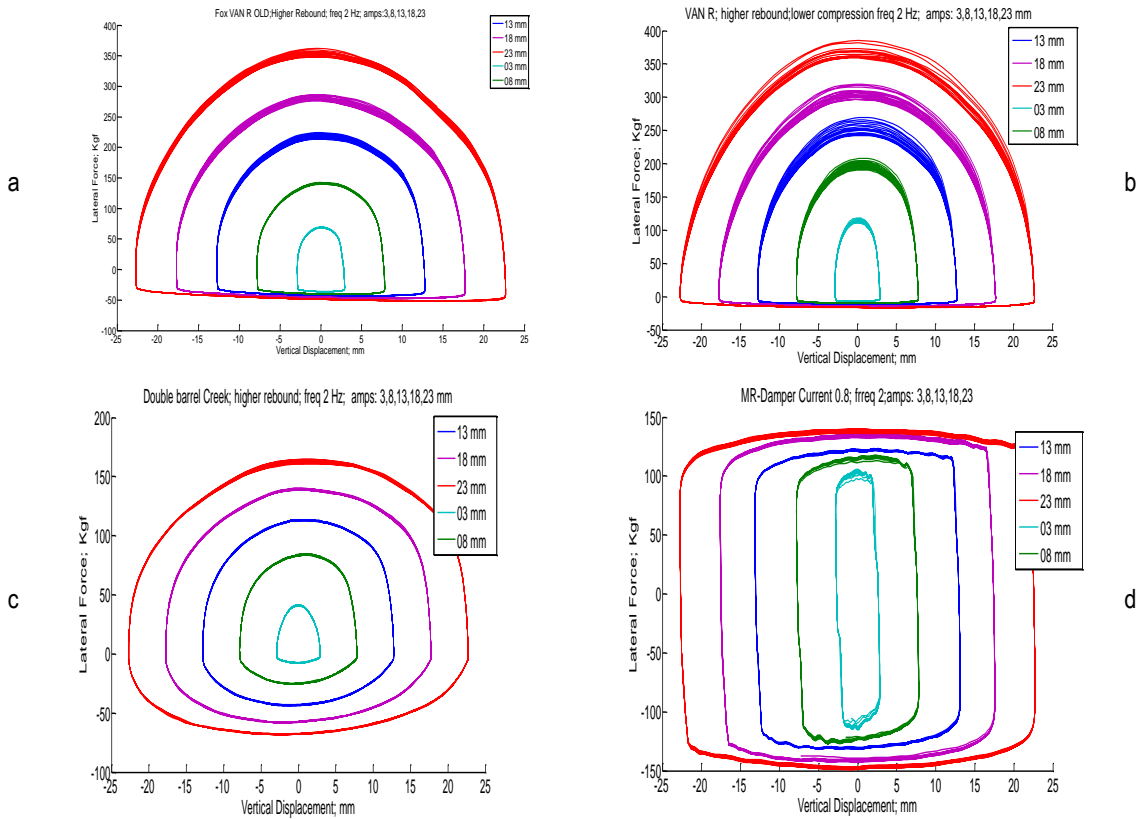


Figure 3.6 Force vs. Displacement in High Rebound (HR)- Low Compression (LR) with 2Hz frequency and different amplitudes: (a) D1 (b) D2 (c) D3 (d) MR damper.

energy dissipation in a damper. Since power is the rate of change of energy in a system; therefore, the area inside force vs. velocity curve represents power consumption. In this section, the forces vs. displacement responses of all four dampers are compared based on amplitude of the input displacement. A comparison of the dampers using a frequency of 2Hz in the high rebound condition and low compression is presented in Figure 3.6. The same comparison for low rebound and high compression and a force vs. velocity for this condition is provided in Appendix A.

Input stimuli frequency effect on performance

As it was mentioned in chapter 2, the velocity of oil flowing through the orifices of a damper has a direct relationship with the amount of damping force created. This

phenomenon can be seen in Figure 3.7, where the performances of D3 and MR damper under the same displacement amplitude of 23mm but different oscillation velocities are presented.

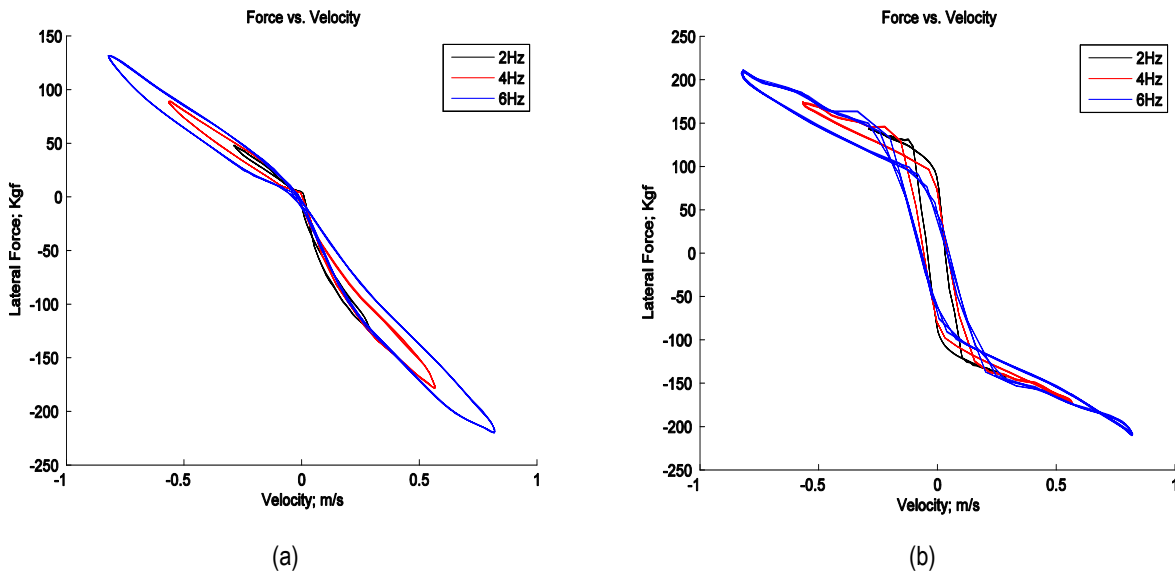


Figure 3.7 (a) F-V curve of D3 damper for different frequencies at 23mm amplitude, (b) F-V curve of MR damper for different frequencies at 23mm amplitude.

Rebound circuit and compression circuit effect on performance

A general understanding is that high rebound is a situation in which the damper tends to quickly return to its normal location, meaning that the amount of damping force during rebound would increase. Higher rebound affects the top half of the displacement curve. On the other hand, the bottom half of displacement curve is related to compression circuit. When on high, a valve that connects the air chamber to the main cylinder closes, making it harder for oil to flow. Consequently, compression produces more damping force. Figure 3.8 exhibits the effect of changing the knob setup on each D1 to D3 dampers.

The damper D1 does not have a compression circuit. Hence, it is only tested under higher and lower rebound adjustments. The flat bottom part of the curve clearly illustrates non variability of the compression. In the meantime, a comparison between (a) and (c) can easily show the effect of the compression circuit. Now the difference between D2 and D3 is very obvious at low speeds (close to the origin). D3 is equipped

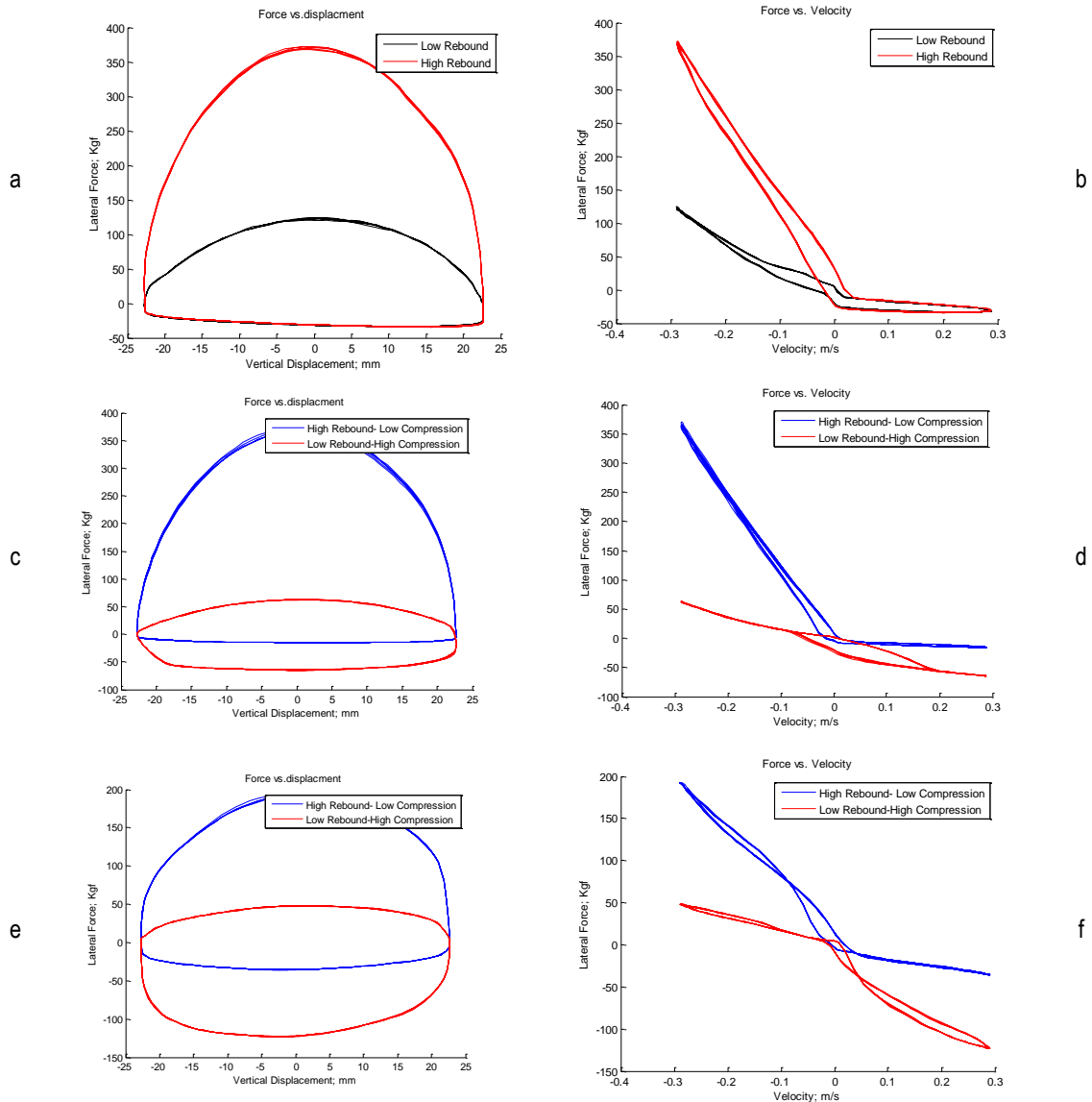


Figure 3.8 Comparison of the effect of knob adjustment: (a) F-D of D1 for LR and HR, (b) F-V of D1 for LR and HR, (c) F-D of D2 for LR and HR, (d) F-V of D2 for LR and HR, (e) F-D of D3 for LR and HR, (f) F-V of D3 for LR and HR.

with two extra knobs for low velocity rebound and high velocity compression, which makes the damper range very wide. Also the characteristic of the damper is almost linear when considering the force vs. velocity curve (a desirable feature in mountain bicycle damper design).

Effect of the Input current on performance

MR dampers do not have any compression or rebound circuits, but instead, their damping force can be regulated by applying different values of currents to the coil. Because of internal design of flow annular, the hysteresis effect of an MR damper is bidirectional. This behavior can be easily modified by applying a controller that can

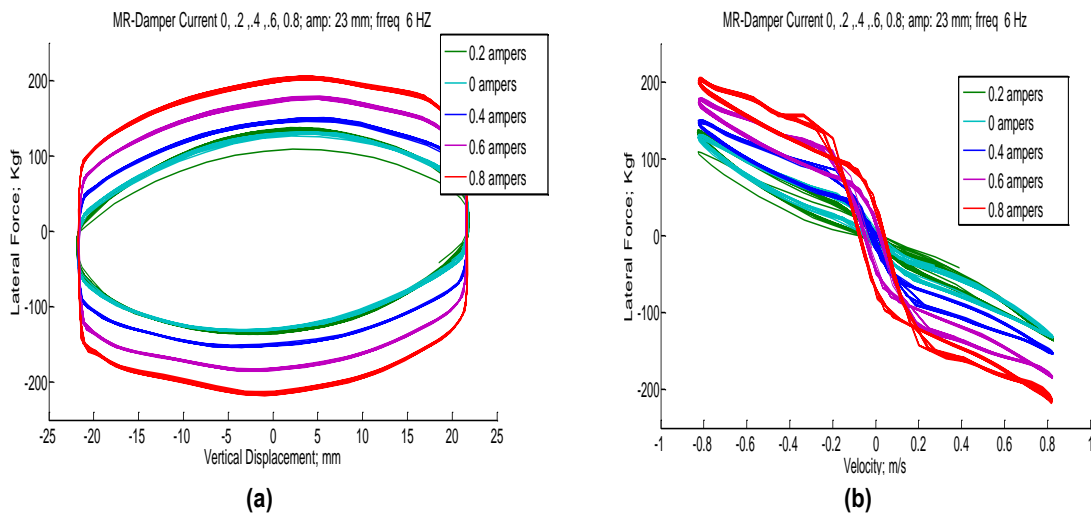


Figure 3.9 MR damper characteristics for different input currents (6Hz, 23mm): (a) F-D curve, (b) F-V curve.

provide current to the MR damper as necessary. Figure 3.9 (a), (b) show changes in MR fluid performance when an input current is applied to the coil of MR fluid. The apparent increase in the damping force can be achieved by increasing the applied current. This property enables the MR damper to achieve a wide range of damping forces and in meantime be able to switch between different curves simultaneously.

Effect of the parallel coil spring on performance

The coil spring does not affect the damping properties since it simply adds an offset spring force to the damping force. Figure 3.10 compares two MR dampers with the

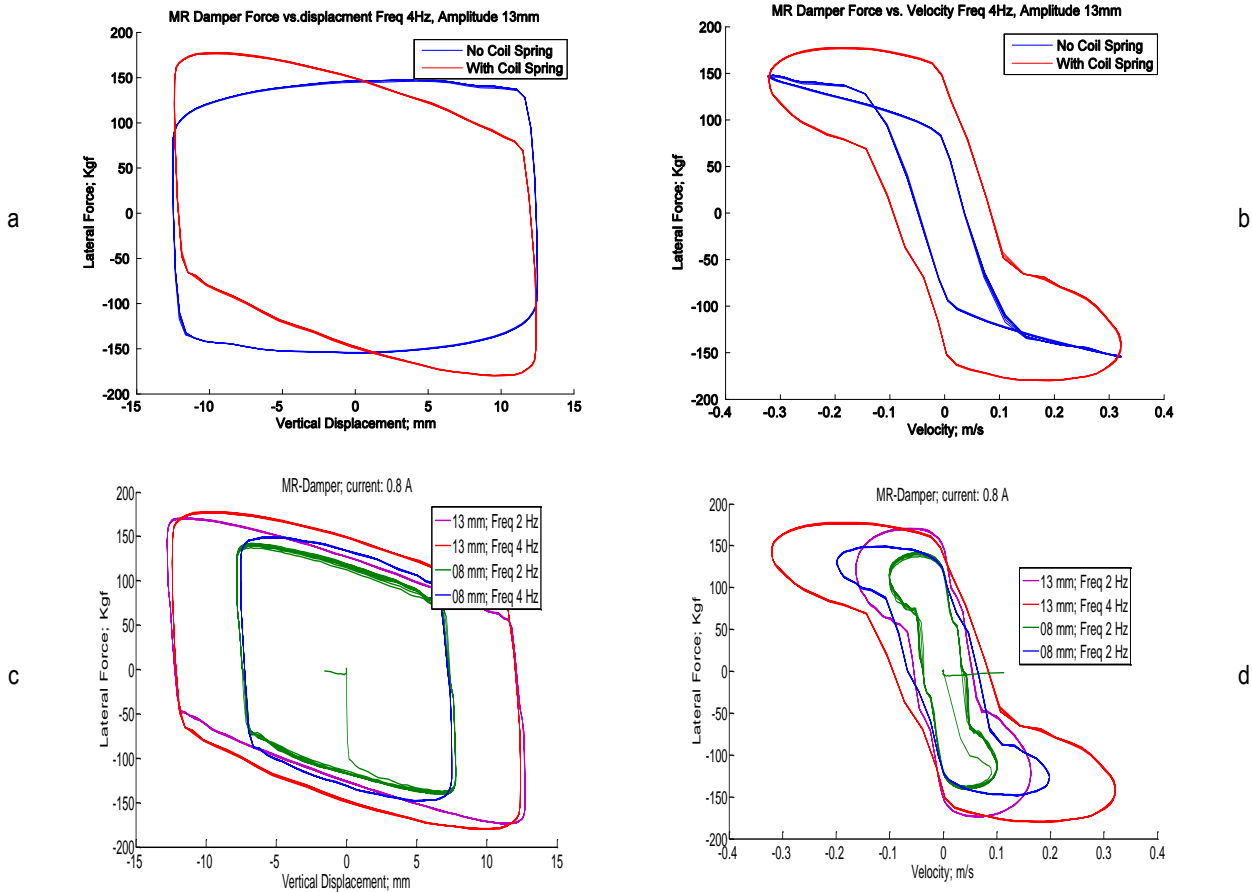


Figure 3.10 Results for MR with spring (current: 0.8 A; amplitude: 08 and 13 mm; frequency: 2 and 4 Hz): (a) F-D characteristic, (b) F-V characteristic. Comparison of MR characteristic with and without spring (current: 0.8 A; amplitude: 13 mm; frequency: 4 Hz): (c) F-D curve, (d) F-V curve.

same input current, frequency, and amplitude, one with coil spring, and the other one without. The results show that the force applied to the sensor at BDC significantly increases because of adding an offset to the force. Changes in the shape of F-D curve are due to the proportionality of spring force with the displacement, i.e. $f = kx$. The same explanation can be given for the case of F-V curve. The amount of spring force just widens the curve, meaning that it adds an offset to the total force, since it releases all the potential energy stored in it. As mentioned before, the area under F-V curve is power. Clearly, implementing a spring increases the level of power consumed. Figure 3.10 shows the effect of adding a spring to the MR damper for different amplitudes and frequencies.

3.2.2. Proof of feasibility

Amongst all the selected conventional dampers, the D3 damper is the most advanced one, Most of the riders prefer to use this model in their downhill bikes. Therefore, if the MR damper can duplicate the damping force of D3 dampers, then it has the capability to replace D3 dampers as well as many other available models in the market. In order to have a meaningful comparison between D3 and MR damper, we selected a specific amplitude-frequency excitation pair (i.e. amplitude: 13 mm; frequency: 4 Hz), and gathered all the results of D3 and MR damper tests for this pair as shown in Figure 3.11.

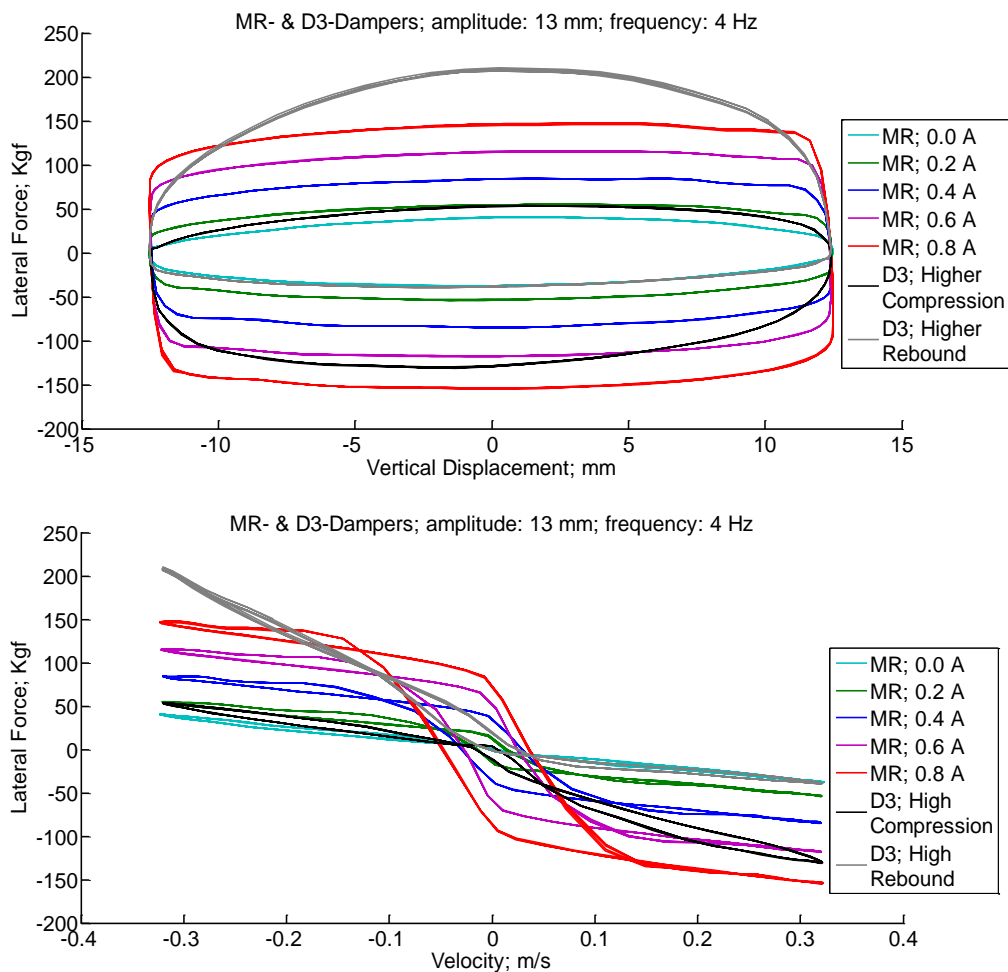


Figure 3.11 Comparison of results for MR and D3 dampers (Without Spring; amplitude: 13 mm; frequency: 4 Hz): (a) F-D curve, (b) F-V curve.

As it can be seen in the figures, the damping force of D3 damper in Higher Compression - Lower Rebound condition, can be easily duplicated if the MR damper applied current is properly controlled. The recorded forces from the MR damper tests do not cover the force range of the D3 damper in the Lower Compression - Higher Rebound condition. This is because we applied electrical currents only up to 0.8 amperes to avoid coils overheating during the long time experiments. In an actual ride, high rebound damping is needed only for short periods of time, which can be produced by applying higher electrical currents (up to 1.5 amperes).

3.3. Conclusion

In this chapter an existing MR damper was tested alongside three conventional mountain bicycle shocks. The objective was to verify the feasibility of such implementation. A mechanism was designed, fabricated, and employed to perform the above comparative tests. A comparison between conventional double barrel damper, by Cane Creek, and MR damper, by Lord Corp, was made. The results indicate the feasibility of using MR dampers to provide the same levels of damping that can be achieved by using conventional mountain bike dampers.

Chapter 4. Design, Simulation, and Optimization

In this chapter, we initially investigate the structure and components of two commercial dampers. Based on these designs and requirements for a mountain bike, a series of design criteria are developed. The magnetic circuits of MR damper valves are further investigated. An Initial model is created in SolidWorks which is imported into the COMSOL Multiphysics software to be analyzed using Finite element Analysis (FEA) techniques. The finite element model is imported into the MATLAB optimization toolbox for design and optimization to achieve the required design criteria.

4.1. Study of two commercial dampers

In this section, we study the conventional Fox Van R shock and Lord 8041-MR dampers in full detail. The idea is to get familiar with the structural configuration of these dampers. These designs can be modified to achieve the required design criteria, for example in terms of weight and size.

Fox Van R Downhill Shock absorber

A downhill conventional shock by Fox, referred to as D2 in the previous chapter disassembled for reverse engineering. In hydraulic dampers, movement of the rod is transferred directly to the piston. The displacement of the piston would result in a pressure change in each chamber. As a result, oil flows from the higher to the lower pressure chamber. In the above path, oil deflects the shims that block the flow orifice. Increasing the thickness using a harder material, and tighter configuration of shims, would increase the pressure drop. As a result, the damper becomes stiffer and consequently the damping force increases. A mathematical model for the damping is proposed in [83].

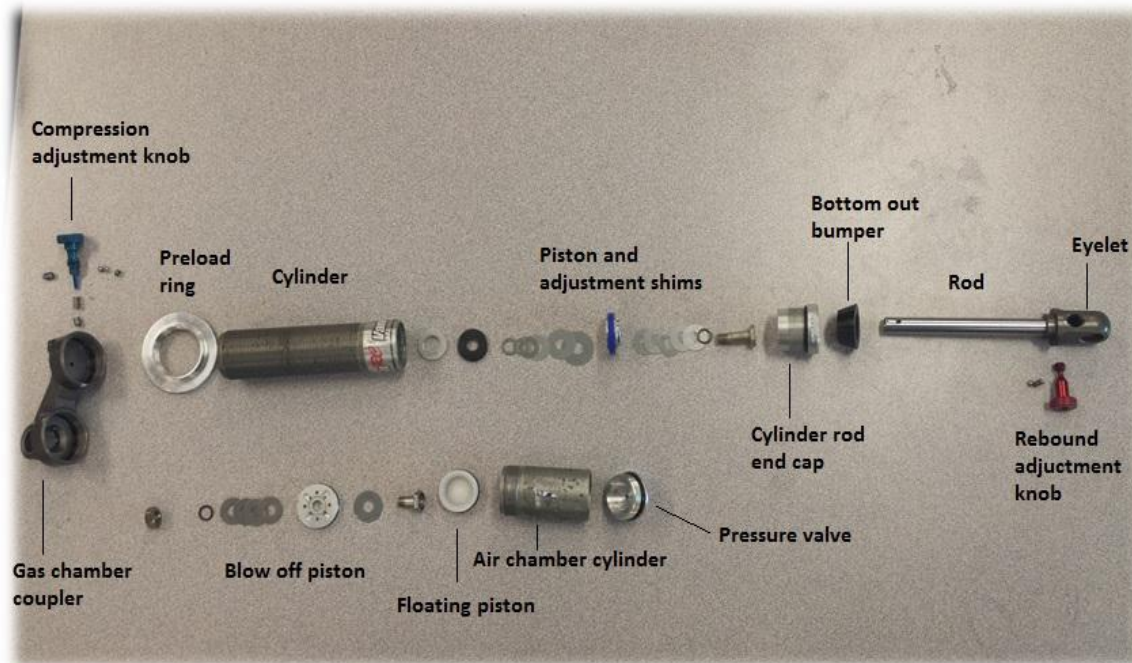


Figure 4.1 Detailed dissection of Fox Van R shock absorber.

A detailed dissection of this damper is shown in Figure 4.1. In order to disassemble the damper, a small hole was drilled in the gas chamber pressure valve to let the air pressure out and prevent any sudden outbreak of oil. After inflation of gas the chamber, a cylinder rod-end cap was opened and hydraulic oil was unfilled carefully. Each part was taken out and cleaned carefully, and role of each component was investigated.

Shaft and Rebound mechanism: Both ends of the shock absorber include Eyelets, which are used to attach the damper to a frame body. The rod is made of anodized steel with an eyelet at one end with the other end attached to the piston. As it was mentioned in chapter 3, a shock absorber is equipped with two adjustment knobs, controlling rebound and compression circuits. The rebound adjustment knob is located at the shaft end. This adjustment mechanism controls the rate at which the shock extends or pulls apart. Turning the knob counter clockwise softens the shock. Figure 4.2(a) displays the rebound circuit mechanism. Increasing the damping force happens as a result of extended needle, blocking the main passage of oil and directing oil through shims. Due to the same mechanism, the rebound phase would be slower, and vice versa [84].

Cylinder rod-end cap: This part is shown in Figure 4.2(b). It is used to close the cylinder on one side and contains sealing and guiding of the shaft. A rod wiper is implemented for the dual purpose of preventing oil leakage and stopping dirt to enter the cylinder. A bushing is utilized to guide the rod and prevent unnecessary non-axial movements. The cap is threaded to be fastened to the cylinder with an O-ring used to seal the device. A bottom out bumper is used to prevent damage in case of sudden and full compression of the damper.

Piston and shim stacks: The piston is comprised of rebound and compression valves and a series of shims, washers, and spacers, attached to each other using a bolt and nut as shown in Figure 4.2(c). One way to achieve different damping characteristics of the damper, in compression and rebound, is that the two sides of the piston have different orifice geometries (see Figure 4.2(d)). An orifice may be large on one side and small on the other, which affects how the oil flows through the piston. Shock tune generally refers to how the shim stacks are laid out on the piston. Different number of shims, shim diameters, and shim thicknesses all contributing to how the shock will react to compression and rebound forces. The overall design of the needle orifice, piston ports, and stacked shims allows damper operation at various shock shaft speeds. The high and low speed compression and rebound forces are affected by this configuration. Also, a valve is used for high speed movements of the piston, called blow-off valve. In case of sudden greater bumps, the blow-off valve opens due to the pressure rise within the damper. This allows the fluid to effectively bypass the more restrictive orifices which are normally at work during damper movement on bump[85].

Cylinder and preload ring: The cylinder is a lightweight aluminum alloy tube. The inside of the cylinder is hard anodized and threaded at the shaft end. To minimize the length, the outside of cylinder is fine threaded and fastened into the gas chamber coupler. Anodizing of the cylinder is important in preventing corrosion and providing a smooth movement of the piston. A preload ring is fastened on the outside of the cylinder which has adjustment capability. Figure 4.2(e) exhibits the cylinder and preload ring. By fastening the preload ring, the coil spring is simply tightened and the rider can apply a preload spring force. Sag is the amount the shock compresses when the rider sits on the bike, usually referred to in terms of distance, or as a percentage of the overall travel.



Figure 4.2 (a) Rod and rebound adjustment mechanism, (b) cylinder cap and bottom out bumper, (c) Piston and shim stacks, (d) compression and rebound valves, (e) cylinder and preload ring, (f) Coupler and compression adjustment knob, (g) gas chamber cylinder and pressure valve, (h) Floating piston.

The more preload, the less the sag will be. Increasing preload also increases the amount of force required to start the shock in motion which reduces small bump sensitivity.

Gas chamber coupler and compression mechanism: Often the oil route to and from the attached reservoir is used for various adjustments to damping characteristics by the addition of separate oil ports with external adjusters. A well designed machined coupler (see Figure 4.2(f)) allows for guiding oil from compression chamber into the gas chamber through a single radial valve. The flow can be controlled by adjusting the compression knob. Turning the knob clockwise tightens the valve, making the shock stiffer to compress. This adjustment is also commonly referred to as the “Bump”.

Gas chamber cylinder and floating piston: The damping oil is placed under pressure by gas and separated by a floating piston. This concept has several advantages. It prevents the chance of cavitations, which happens when the oil cannot move fast enough and become extremely hard. It also provides for better cooling, especially if the shock absorber has an external cylinder. Another advantage is provision of consistent damping, regardless of the shock absorber's working temperature. Furthermore, the durability and lifetime of the shock are improved. The external cylinder creates a larger cooling area and improves performance and durability[85], (see Figure 4.2(g)). The floating piston in Figure 4.3(h) is made of durable plastics and fully sealed to prevent leakage of fluid to the gas section.

Lord 8041 MR Damper

The MR damper 8041 from Lord Corporation is designed for industrial suspension applications. The damper performance was investigated in chapter 3. As discussed in chapter 2, the inside cylinder is filled with MR fluid with a piston dividing the cylinder into two chambers. The damper was dismantled by drilling a small hole in the body of the cylinder to get all the MR fluid out. After drainage of the MR fluid, a section of the cylinder was cut, so that the components of the damper can be studied. Figure 4.3 shows all the components of the MR damper.

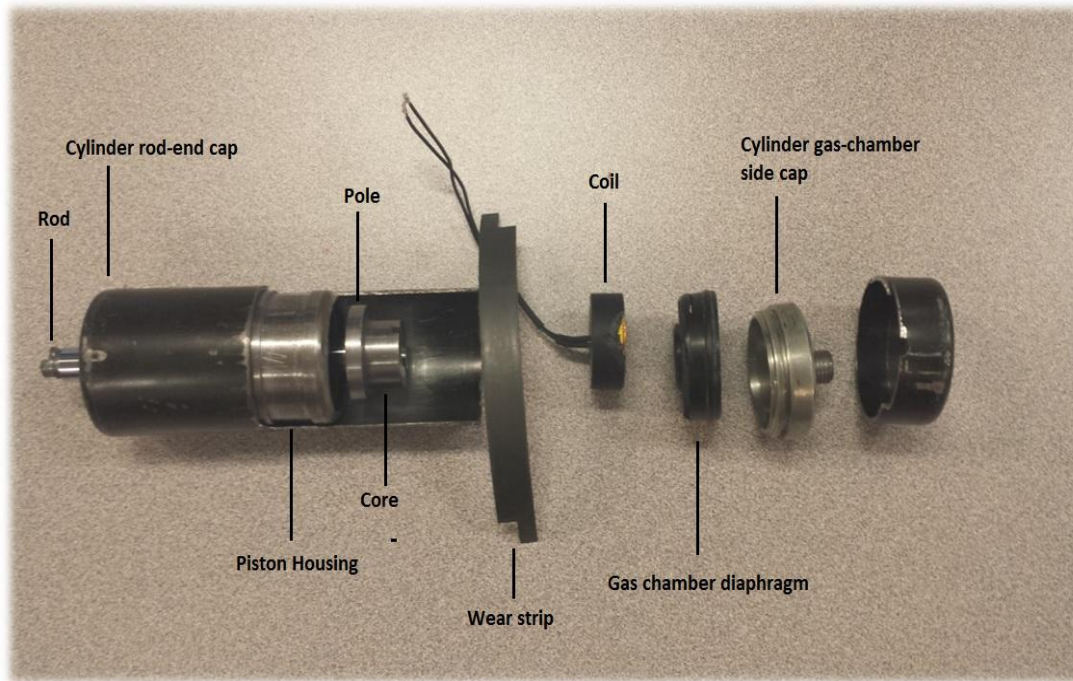


Figure 4.3 Detailed dissection of Fox Van R shock absorber.

Cylinder: The thin cylinder is fabricated from a magnetic material with a black coating. In order to figure out the material, an alloy spectrometry was performed at 4D labs at SFU. The results show that the alloy is a low-carbon steel, which has most likely been used due to its strength, cost, and machinability. Figure 4.4 illustrates the results of alloy spectrometry. The peak element is iron and shorter ones are carbon and oxygen, respectively. Both ends of the cylinder are hard pressed to caps.

Shaft and cylinder rod-end cap: The rod is a hollow hard anodized steel to accommodate wires. There is a handle containing an eyelet and a bushings situated inside of eyelet, enabling the MR damper to be attached to a frame. The end of the rod is further threaded and attached to the handle as shown in Figure 4.5(a). The cap has a mechanism very similar to the Fox damper cap in which a bushing and a rod wiper are placed inside the cap to seal the cylinder and guide the rod.

Piston housing and piston guides: A low-carbon magnetic steel is used in fabrication of the tube shaped piston housing, which fits inside the main cylinder. There is a slot machined on the outer surface of the piston housing, where a Teflon wear strip is fitted. A wear strip is used to prevent wearing of the piston housing and inside of the

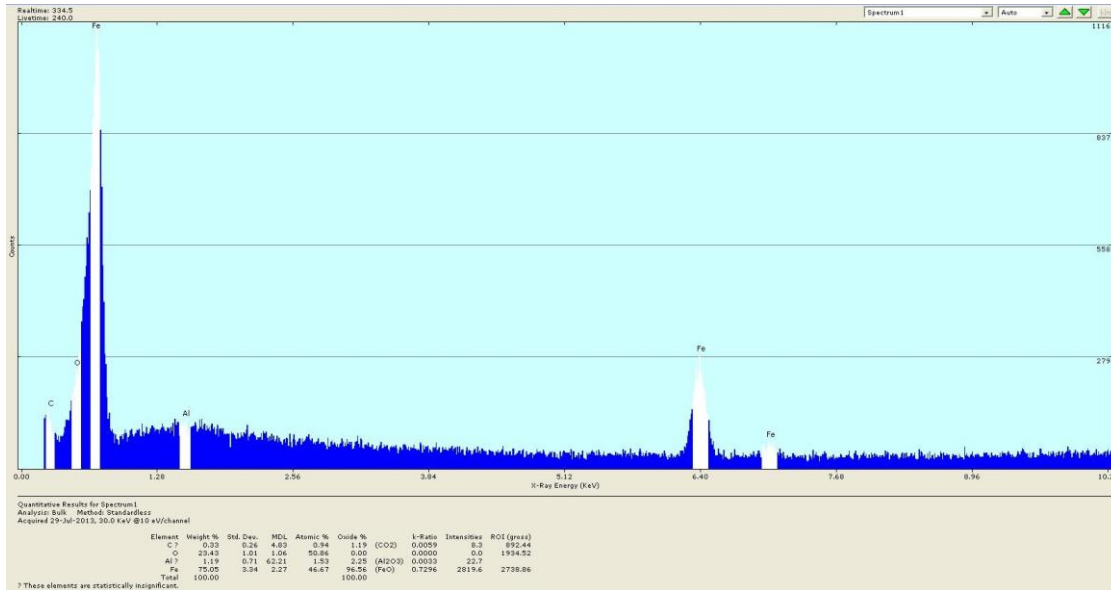


Figure 4.4 Spectrometry result for cylinder material (peaks showing Fe, O, C).

cylinder, as well as stopping any transition of MR fluid in between the housing and cylinder. To allow for a proper MR fluid gap between the piston poles and housing, poles and core need to be perfectly centered inside the housing. To achieve that, a thin piece of metal, shown in Figure 4.5(b), is pressed to the piston housing and held inside the piston aligned at the center.

Piston core, piston poles, and coil: These parts include a magnetic core with a through hole at the center for passing wire and a slot for installing the coil. Two magnetic poles are pressed on both sides of the core, in order to complete the magnetic path shown in Figure 4.5 (d) (showing core and one pole). Finally, a coil wound with non-magnetic cover fits around the core and between the two poles (see Figure 4.5(c) showing coil with a Teflon cover). The main wires pass through the hollow gap inside the core, pole, and rod. As mentioned in chapter 2, the diameter and length of core, lengths of poles, MR fluid flow gap, and cross section of coil determine the number of turns and cross section of the wire. These parameters are important factors that determine the value of the induced magnetic.. Figure 4.5(f) shows the MR fluid flow gap.

Gas chamber mechanism: The Lord 8041 MR damper is not equipped with a variable gas chamber or floating piston. The gas chamber consists of a rubber diaphragm which divides the fluid from gas. The only purpose of using an air chamber is

to compensate for the rod volume entering the cylinder. The cylinder gas chamber-end cap is made of steel to endure high pressures. The damper caps are pressed to the cylinder body and cannot be opened easily. Figure 4.5(e) displays the diaphragm and cap.



Figure 4.5 (a) Rod handle with bushing and wires, (b) Piston housing, wear strip, and guides, (c) Coil, (d) Magnetic pole and hollow core with coil slot, (e) Rubber diaphragm and cap, (f) MR fluid flow gap filled with MR fluid.

4.2. Optimal design of an MR damper

Various designs which were investigated in chapter 2 have the potential to be implemented in a mountain bicycle application. In this thesis, we study an initial design based on the Lord Corp RD-8040-1 MR damper. The objective is to redesign the damper based on criteria such as weight and size dictated by the mountain bike application.

This section presents further details of the design process for our MR damper using FEA analysis. The materials utilized in the damper design are investigated followed by an analysis of the magnetic field in MR valve. A finite element simulation of the MR valve in Comsol Multiphysics is presented next. A constrained optimization problem is formulated and solved by integrating MATLAB optimization toolbox and Comsol Multiphysics.

4.2.1. *Material selection*

A main step in the design process is to obtain the requirements in a mountain bicycle application. Such requirements include having a wide dynamic range, quick time response, small power consumption, and most importantly a smaller weight than conventional dampers. An important consideration is the choice of the materials to be used. In particular, the materials should withstand the induced forces and pressure, be corrosion resistant, provide the desired magnetic properties, and have a small mass density.

The first group of components studied were the cylinder, cylinder caps, and the shaft. One of the reasons to choose above configuration is that the magnetic circuit is formed between the core, poles, and piston housing. Therefore, the cylinder does not need to be of magnetic material, hence it can be substituted by less dense materials. An important consideration in this case is the strength of materials under pressure. It should be noted that most of the applied force is axial. As mentioned before, the cylinder in Lord Corp MR damper is made of carbon steel, which is a high density material. Furthermore, the shaft is made of high carbon anodized steel and the caps are made of high strength steel. Table 4.1 shows various alternatives for carbon steel which are compared in terms of density, tensile stress, and material yield point.

Table 4.1 Material available for Cylinder body.

Material	Density (g/cm ³)	Tensile stress (psi)	Yield point (psi)
Carbon Steel 1018	7.7	64,000	54,000
Aluminium 6061	2.7	45,000	40,000
Aluminium 6063	2.7	27,000	21,000
Aluminium 7075	2.7	83,000	73,000
Carbon Fiber Tube	1.75	87,000	80,000

Aluminum is a widely available material, easily machinable, fairly light, and high strength in high grading. On the other hand, carbon fibre (CF) has high stiffness and tensile strength, low weight, high chemical resistance, high temperature tolerance, and low thermal expansion. The above characteristics make carbon fibre a favorable choice in this application. However, high cost and hard machinability are the shortcomings of this material. For the first prototype, Aluminum 7075 which is a strong zinc alloy is utilized. This material has strength comparable to many steels, has a good fatigue strength, and average machinability. The shaft is made of the same material with a hard anodized finish to prevent corrosion.

Materials for core, poles, and piston housing are made of cold rolled carbon-steel 1018, a low carbon steel with high machinability, a fairly high relative magnetic permeability of 1000, and good strength. Cold rolling increases tensile strength, yield strength, torsional strength, surface hardness, and wear resistance. Nguyen and Choi [19] employed silicon steel as the magnetic body. Silicon steel is a specialty steel tailored to produce certain magnetic properties such as a small hysteresis area (small energy dissipation per cycle, or low core loss), high relative permeability of 4000, and high saturation up to 1.5 T. However, silicon steel is usually manufactured in the form of cold-rolled strips less than 2 mm thick, called laminations, stacked together to form a core, but is hard to machine. Another main consideration for the magnetic body material in DC applications of the damper is permeability and saturation magnetization [3]. Based on the above considerations, the cold rolled carbon steel 1018 was utilized in the design.

The diaphragm used in Lord MR damper was substituted with a floating piston, made of TM Delrin [®] acetal resin, with high mechanical strength and rigidity, toughness, high resistance to repeated impacts, long-term fatigue endurance, excellent resistance to moisture, gasoline solvents, and many other neutral chemicals.

The last component in an MR damper is the MR fluid. Lord Corp have not disclosed the MR fluid used in their damper. In general, there are a few MR fluids available in market. Table 4.2 compares important properties of some of the available commercial MR fluids in the market. The properties of a good MR fluid in mountain bike applications are low mass density, low off state viscosity, high maximum shear stress, small thermal dependency, near neutral pH (Non-corrosive carrier and additives), and having appropriate additives to prevent oxidation.

In order to reduce the weight, MRF-122EG was initially chosen. However, after simulation and optimization of the design, it was concluded that the chosen MR fluid cannot provide enough shear stress for produced magnetic field. Therefore, MRF 132DG was replaced with the previous MRF which met the optimization constrains. Appendix C provides datasheets from Lord Corp. on characteristics of the MR fluids.

Table 4.2 Commercial MR fluid available.

	Producer	Density g/cm ³	Solids Content Weight, %	Max Shear stress (Kpa) @ 0.7 T	Off-State Viscosity Pa.s
MRF-122EG	Lord	2.28-2.48	72	~33	0.042 ± 0.020
MRF-132DG	Lord	2.95-3.15	81	~45	0.112 ± 0.02
MRF-140CG	Lord	3.54-3.74	85	~55	0.280 ± 0.070
BASF 2040	BASF	2.47	N/A	~38	0.5 ± 0.04
BASF 5030	BASF	4.12	N/A	~70	0.41 ± 0.03

4.2.2. Magnetic field analysis of MR damper

The MR fluid flow gap is one of the links in the magnetic circuit of an MR damper, along with the magnetic poles and piston housing, Figure 4.6 shows all links and the magnetic field path passing through the device. Using Kirchoff's law magnetic circuit for an axisymmetric model can be written as:

$$\sum H_k l_k = 2H_{mr} t_g + H_c (l_c + l_p) + H_p (2R_{pole} + W_{op}) + H_{op} (l_c + l_p) = NI \quad 4.1$$

where H_k is the magnetic field intensity in the k th link of the circuit, l_k is the overall effective length of that link. Also, N is the number of turns of the valve coil, I is the applied current, and H_c, H_p, H_{op}, H_{mr} are the magnetic field intensity of core, pole, outside piston or piston housing, and MR fluid gap, respectively. The magnetic flux conservation rule of the circuit is given by:

$$\phi = B_k A_k \quad 4.2$$

where ϕ is the magnetic flux of the circuit [webers] passing through A_k the cross-sectional area [m^2], with B_k magnetic flux density of the k th link, respectively. Magnetic flux in all links are equal. B_k is the number of flux lines per unit area [tesla] and increases in proportion to the magnetic intensity H_k as mentioned in chapter 2 [12]:

$$B_k = \mu_0 \mu_k H_k \quad 4.3$$

Here μ_0 is the magnetic permeability of vacuum ($\mu_0 = 4\pi * 10^{-7} T m A^{-1}$) and μ_k is the relative permeability of the k th link material. Generally, the B-H curve is nonlinear due to entering saturation, or a decrease in polarization capability when magnetic field intensity is increased [12]. By using equations 4.1, 4.2, and considering that magnetic flux everywhere is equal, and after some simplification, the magnetic field intensity in an MR fluid gap can be approximated by [12]:

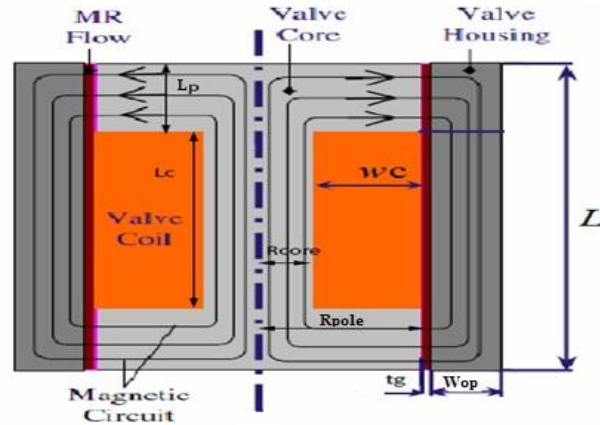


Figure 4.6 MR valve magnetic links and magnetic path.

$$H_{mr} = \frac{NI}{2tg} \quad 4.4$$

in which N , t_g and I represent the number of coil turns, the gap size, and electrical current to the coil, respectively. The electromagnetic force is proportional to the product of the number of turns around the core in which the flux is induced. By increasing number of turns or input current, the magnetic field in the gap can be increased. Since the cross section of the coil is limited, a higher number of turns should be used to reduce the wire cross section, which allows less current. That necessitates the optimization of the magnetic circuit for this damper. From the above equation, it can be concluded that the relationship between I and H_{MR} is linear. This level of simplification can reduce the accuracy of results [12], [53]. Therefore, the finite element method has been used to achieve an accurate result.

4.2.3. Finite element simulation

Initially, a detailed CAD model of the Lord 8041 damper in SolidWorks was developed as shown in Figure 4.7(a). In order to set the start point of simulations, The LiveLink by Comsol Multiphysics was employed to import a CAD model into Comsol as shown in Figure 4.7(b). The imported model was a 3D model which made calculations extremely time consuming. Since the geometry of MR valve structure is axisymmetric, and to reduce the computational cost, a 2D axisymmetric model with the same

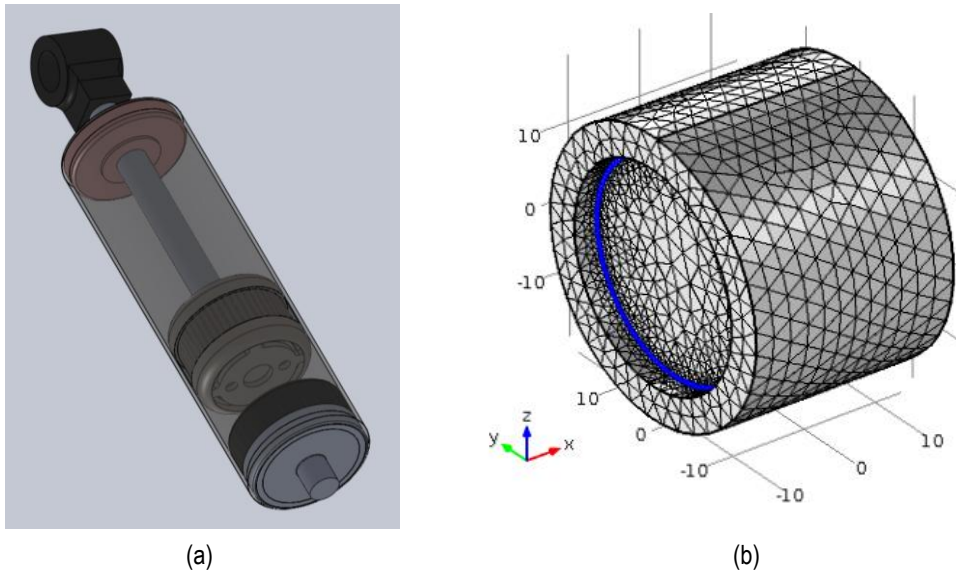


Figure 4.7 (a) SolidWorks CAD model of the Lord 8041 MR damper, (b) Imported 3D model using LiveLink, (c) 2D model in Comsol.

dimensions as 3D model was developed. Subsequently, the finite element was used to model the valve for the purpose of electromagnetic analysis. Furthermore, magnetic flux density B , and magnetic field intensity H , in different valve regions were calculated for a constant 1 Amp input current (operational current of Lord MR damper for continuous operation), and a coil with 400 wire turns.

Approach and Assumptions

Design variables (DV) which are chosen for valve optimization are assigned as global parameters in Comsol. Figure 4.8 illustrates the optimization parameters: core radius R_s , gap size t_g , thickness of piston housing wall w_{op} , core length L_c , and pole length L_p , chosen as design variables. The Comsol AC-DC module was utilized in simulation of the magnetic valve. A stationary magnetic field (mf) was assumed in Comsol. The magnetic core material, poles, and outside piston was chosen as soft iron with losses to account for magnetization, remnant flux density, and saturation. The coil was defined as copper from materials library with general Ampere's law applied to magnetic field calculations. Finally, the MR fluid was created as a new material using data provided in the datasheet of Lord MR fluids MRF122EG and MRF132DG.

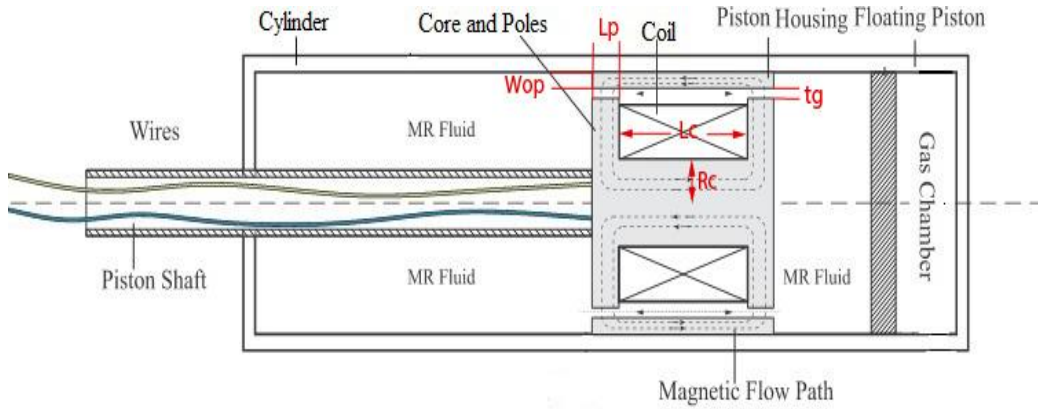


Figure 4.8 MR damper selected design with DVs.

A multi-turn coil was implemented as the magnetic intensity inducer. The multi-turn coil node is a lumped model for a bundle of tiny wires tightly wound together but separated by an electrical insulator. In this scenario, the current flows only in the direction of the wires and is negligible in other directions. For the coil current applied in simulation is static (DC), current density is calculated using:

$$J = \frac{NI}{A} \quad 4.5$$

where N is the number of coil turns, I is input current, and A is the cross sectional area of the coil [12]. Therefore, from equation 4.1 it can be inferred that current density of coil wire is equal to gradient of magnetic field intensity:

$$J = \nabla \times H \quad 4.6$$

In simulation study, we assumed that the outside boundaries are fully insulated from the surroundings with no magnetic leakage happening. Magnetic insulation adds a boundary condition that sets the tangential components of the magnetic potential to zero at the boundary. The magnetic field intensities are calculated in nodal points for the core, poles, MR fluid, and the piston housing. In order to apply magnetic losses for both iron and MR fluid, an alternative Ampere's law is used. In the second Ampere law, the constitutive relation is based on HB curve. Consequently, using a polynomial

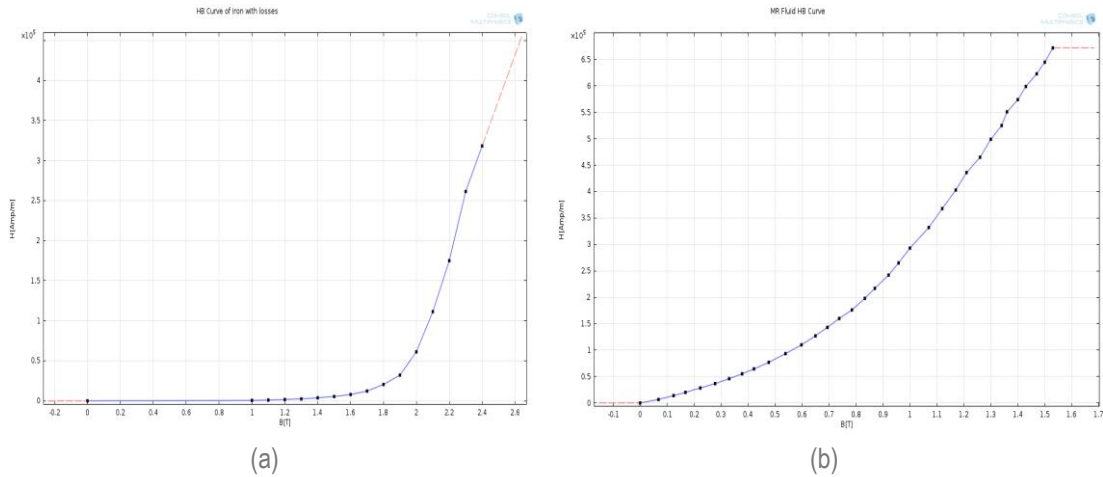


Figure 4.9 (a) HB curve of Comsol materials library, (b) MR fluid HB curve from Comsol obtained from datasheet.

interpolation and soft iron HB curve with losses (see Figure 4.9(a)) flux density is calculated. In case of MR fluid, the HB curve was acquired from datasheet using graph converting software (see Figure 4.9(b)). Note that the saturation flux of iron is around 1.8 [T] and for the MR fluid it is around 1.6 [T].

Mesh nodes enable the discretization of the geometry into small units of simple shapes, referred to as mesh elements. As it is well known, using finer meshes results in more accurate results. However, a smaller meshing size results in an increase in the computational cost. Different meshing sizes and attributes were applied, and finally a fine free triangular meshing was chosen for the entire geometry, except for the MR fluid gap, which is meshed using extremely fine free triangular meshes. From simulations, it was observed that at the edges of each solid part, inconsistencies happen. Thus to increase accuracy at solid part borders, an edge type mesh was applied to borders of MR gap and the border line between coil and core. Meshing of the model is exhibited in Figure 4.11. The dimensions could change during the optimization process and model was rebuilt. Comsol automatically changes the meshing properties during each run.

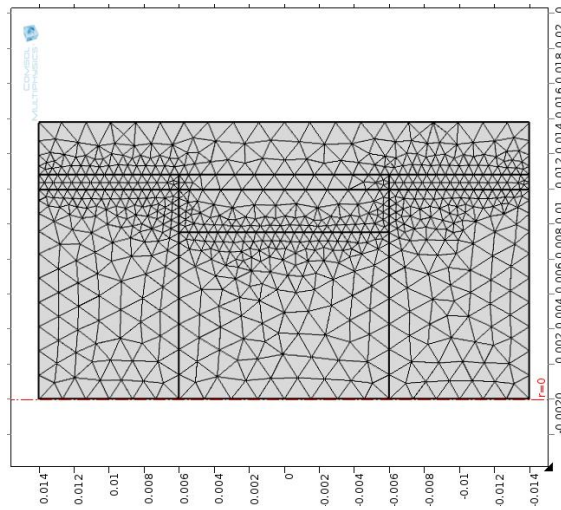


Figure 4.11 Customised meshing used for FEA simulation.

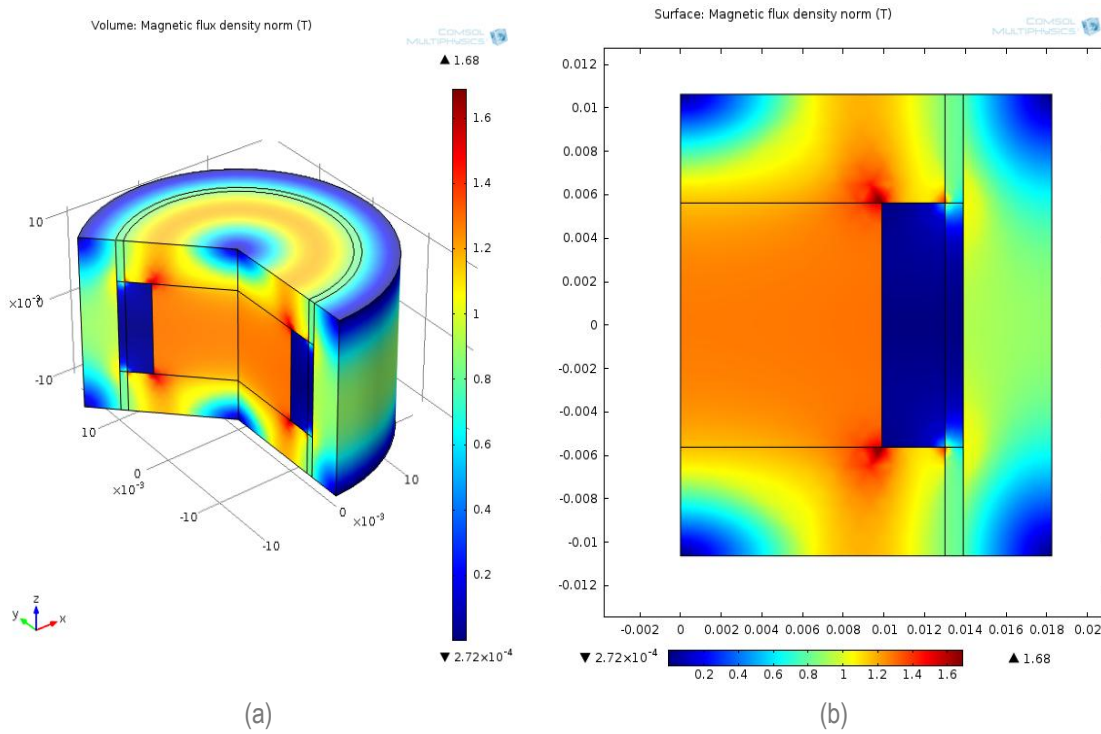


Figure 4.10 (a) 3D simulation to study x density for Lord MR damper, (b) 2D simulation of flux density for Lord MR damper.

Output data

In this study, the finite element method was used to investigate magnetic field intensity and magnetic flux density in different domains of valve, during changes in geometrical dimensions. The obtained results were further utilised in the optimization of magnetic valve. The geometrical model of Lord MR damper was simulated at first to investigate the flux density distribution. Design variable dimensions for this model are shown in Table 4.3. The resulting 3D model is shown in Figure 4.10(a) and the 2D model is shown in Figure 4.10(b).

The magnetic field intensity H and the magnetic flux density B of nodes are not constant all around various domains. Thus an averaging method, such as nodal summation or nodal integration over surface, was performed to obtain the average flux density and field intensity in different domains. For the purpose of design optimization, the average values across the MR valve gap have been used as shown in Table 4.3 contains study results for Lord MR damper.

Table 4.3 Design parameters of Lord MR damper.

PARAMETER	VALUE	PARAMETER	VALUE
Piston outside radius	18.25 [mm]	MR average field intensity	1.07.91 [<i>kAmp/m</i>]
Gap size	9 [mm]	Iron average flux density	1.1702 [T]
Radius of core	9.9 [mm]	MR average flux density	0.58887 [T]
Width of outer piston wall	4.35 [mm]	Iron max flux density	1.85371 [T]
Length of core	11.25 [mm]	MR max flux density	0.9546 [T]
Length of pole	5 [mm]		

4.2.4. Optimization using finite element analysis

The main goal of optimization is to find optimal internal dimensions for an MR damper magnetic valve, considering an objective function, while a desired output damping force is provided, mass of the MR damper is minimized, and a desired dynamic range is obtained. For the design of the MR damper, a series of assumptions need to be made. First, particles are distributed evenly in the MR fluid without any concentrations.

Further, linear velocity distribution conditions with no slip govern overflow velocity of the MR damper. The thermodynamic and inertial effects of the MR fluid are neglected as well as the frictional force[48].

The flowchart below indicates all the steps in the optimization procedure. In the last section, creating the Comsol geometry model was introduced.

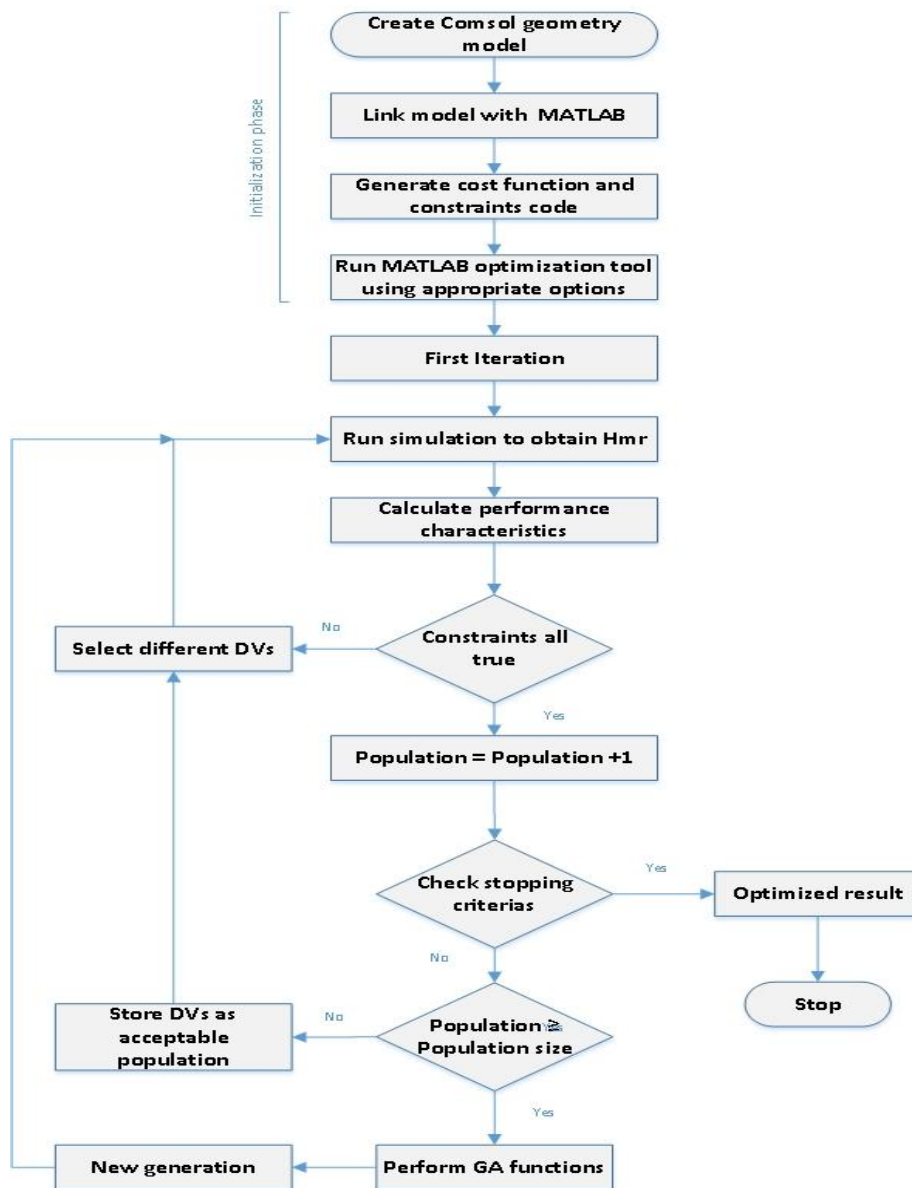


Figure 4.12 Optimization procedure flow chart.

Optimization objectives

In a mountain bicycle suspension system application, a high damping force is required to minimize the suspension travel, prevent bob pedalling, and reduce high amplitude bumps. Hence, a low damping level is favorable to increase ride comfort. As a result, a large dynamic range is needed. Also, minimization of MR damper mass is of the highest priority due to the requirement of mountain bikes to be as lightweight as possible.

As it was discussed in chapter 2, the main performance indexes of MR damper which can be incorporated into the objective function are the damping force, dynamic range, and total mass. The total damping force of an MR damper is a combination of forces produced by the gas accumulator F_g , viscouse force due to pressure drop along the piston valve F_η , and active force or shear stress related the MR force F_{mr} . In the absence of a magnetic field, the only forces available are F_g, F_η , which generate the passive force for MR damper. On the other hand, F_{mr} is responsible for active orcontrollable portion of the forces.

$$F_g = A_s P_0 \left(\frac{V_0}{V_0 + A_s x_p} \right)^\gamma, F_\eta = \frac{12\eta L}{\pi R_d t_g^3} (A_p - A_s)^2 \dot{x}, F_{mr} = 2 \frac{c L_p \tau_y}{h} (A_p - A_s) \quad 4.7$$

$$F_{passive} = F_\eta + F_g \quad 4.8$$

$$F = F_{passive} + F_{active} \quad 4.9$$

where P_0 and V_0 are the initial pressure and volume of the accumulator, γ is the coefficient of thermal expansion (ranging from 1.4 to 1.7 for adiabatic expansion), x_p is the piston displacement, and A_p and A_s are he piston and piston-shaft effective cross-sectional area, respectively, τ_y is the yield stress of the MR fluid induced by the applied magnetic field, η is the post yield viscosity of MR fluid equal to 0.092, L is the length of the piston, L_p is the length of the magnetic pole, R_d and t_g are the average radius and gap of the annular duct, c is the coefficient which depends on flow velocity profile and here is equal to 3 [86]. In our optimization, in order to match previous experimental data,

$F_{MR_{max}}$ is the yield stress force with the maximum applied current of 1 [Amp] at max piston velocity of 0.8 [m/s]. The max velocity selection is to match the maximum tested velocity for experimental data of chapter 3. The MRF 132DG datasheet provides shear stress vs magnetic field intensity curve. (equation 4.10 was developed using curve fitting in MATLAB, which shows the induced yield stress of the MR fluid and can be expressed as a function of the magnetic field intensity at the poles active area (H_{mr}):

$$\tau_y = p(H_{mr}) = C_0 + C_1 H_{mr} + C_2 H_{mr}^2 + C_3 H_{mr}^3 \quad 4.10$$

The units for τ_y and H_{mr} are kPa and kAm^{-1} , respectively. The coefficients $C_0, C_1, C_2,$ and C_3 are identified from curve fitting as follows: 0.3, 0.42, -0.0012 and 1.05e-6.

The dynamic range of MR damper can be expressed as a ratio of the total peak force under maximum applied current to the passive force in the absence of current. The overall performance of an MR valve can be expressed by the dynamic range. A larger dynamic range is indicator of a wide control range, which is highly desirable. Since the gas accumulator force is constant in both states, we can omit that. Therefore, the dynamic range can be expressed as [12].

$$\lambda_d = \frac{F_\eta + F_{mr}}{F_\eta} \quad 4.11$$

The total mass is a critical issue in mountain bikes which introduces another important index in the optimization function. The damper device mass is a mass function of volumes of each component multiplied by density of the material used for that piece. Mass function can be expressed as follows:

$$M = \pi \rho_{mr} \left((R_{ic}^2 - R_s^2) Stroke \right) + 2t_g L_{piston} + \dots$$

$$\pi \rho_{iron} \left((R_{ic}^2 - R_{inp}^2) L_{piston} \right) + (2R_p^2 L_p) + (R_c^2 L_c) + \dots \quad 4.12$$

$$\pi \rho_{cooper} ((R_p^2 - R_c^2)L_c))$$

$$\pi \rho_{aluminum} * ((R_s^2 - R_{sh}^2)L_s + (2R_{ic}^2L_{cap}) + ((R_{oc}^2 - R_{ic}^2)L_{cylinder}))$$

The mass of MR fluid can be calculated by multiplying density in volume where the MR fluid exists. The term $\pi(R_{ic}^2 - R_s^2)Stroke$ represents the volume of inside the cylinder minus shaft. The term $\pi(R_{ic}^2 - R_s^2)Stroke$ deals with flow gap. The iron mass of the damper is given by L_{piston} which presents piston outer piston, $\pi(2R_p^2L_p)$ accounts for two magnetic poles, and $\pi(R_c^2L_c)$ expresses magnetic core of the mass of electromagnetic coil is given by $\pi(R_p^2 - R_c^2)L_c$. Finally, an Aluminum piston rod which was used to reduce weight is with its volume given by $\pi(R_s^2 - R_{sh}^2)L_s$. The cylinder caps have volume $\pi(2R_{ic}^2L_{cap})$ and the cylinder tub volume is given by $\pi((R_{oc}^2 - R_{ic}^2)L_{cylinder})$.

The dynamic range and weight are both important indexes for optimization. In this case, a multi-objective function is proposed. The proposed objective function tends to increase dynamic the range while minimizing weight is expressed as:

$$OBJ = w_m \left(\frac{M}{M_{desired}} \right) + w_\lambda \left(\frac{\lambda_{desired}}{\lambda} \right) \quad 4.13$$

where, M, λ are the mass and dynamic range, and $M_{desired}, \lambda_{desired}$ are the desirable values for mass and dynamic range, and finally w_m, w_λ are the weight factors for mass and dynamic range ($w_m + w_\lambda = 1$). The weight factors can be modified to change the performance of damper. The objective function was thus selected as follows:

$$OBJ = 0.7 \left(\frac{M}{0.8} \right) + 0.3 \left(\frac{4}{\lambda} \right) \quad 4.14$$

Table 4.4 Constants and intermediate variables.

Constant or intermediate variable	Description	Value or expression	Unit
<i>Roc</i>	Radius of outside of cylinder	0.019 (1-1/2)	Meter (inch)
<i>Ric</i>	Radius of inside of cylinder	0.015875 (1-1/4)	Meter (inch)
<i>Rs</i>	Radius of rod	0.00476 (3/8)	Meter (inch)
<i>Rsh</i>	Radius of rod hole	0.00225	Meter
<i>Rop</i>	Radius of outside of outer piston	<i>Ric</i>	Meter (inch)
<i>Lgc</i>	Length of gas chamber	0.038 (1.496)	Meter (inch)
<i>PO</i>	Initial pressure of gas chamber	4e5 (58)	Pascal(psi)
<i>VO</i>	Initial volume of gas chamber	3e-5	square meter
<i>Rp</i>	Radius of pole	<i>Ric - Wop - tg</i>	Meter
<i>Lpiston</i>	Length of piston	<i>Lc + 2Lp</i>	Meter
<i>Wcoil</i>	Width of coil area	<i>Rp - Rc</i>	Meter
<i>Lcap</i>	Length of cylinder caps	0.08	Meter
<i>Lf</i>	Length of floating piston	0.08	Meter
<i>Rd</i>	Average radius of annular duct	<i>Rp + (tg/2)</i>	Meter
<i>Stroke</i>	Maximum stroke length	55 (2.16)	Meter (inch)
<i>Ls</i>	Length of shaft	<i>Stroke + Lcap + .02</i>	Meter
<i>Lcoil</i>	Length of coil	<i>Lcore</i>	Meter
<i>Acoil</i>	Cross sectional area of coil	<i>Lcoil * Wcoil</i>	square meter
<i>Riop</i>	Inner radius of outer piston	<i>Ric - Wop</i>	Meter
η	Plastic viscosity	0.092	Pa.s
<i>Imax</i>	Maximum current	1	Ampere
<i>Vmax</i>	Maximum velocity of piston head	0.8	m/s
<i>c</i>	coefficient of flow velocity profile	3.00	NA
γ	coefficient of thermal expansion	1.4	NA
ρ_{mr}	Density of MR fluid	2450	Kg/m3
ρ_{copper}	Density of copper	8690	Kg/m3
ρ_{iron}	Density of pure iron	7800	Kg/m3
$\rho_{Aluminum}$	Density of aluminum	2700	Kg/m3
<i>Fdesired</i>	Desired passive force	400	Newton

Nguyen *et al.* [40] indicate that the wire gauge itself does not affect the magnetic field induced. Therefore, the cross section of coil is obtained. Section 4.2.5 is dedicated to finding the best wire gauge. The term B_{Max} stands for maximum flux density induced in the magnetic circuit, which should not exceed saturation limitation of the magnetic material. Finally, we need a minimum dynamic range from the damper and values less than that do not provide acceptable performance.

Table 4.5 Design variables and parameters constraints.

<i>Parameter</i>	<i>Value</i>	<i>Parameter</i>	<i>Value</i>
R_c	$0.005m \leq R_c \leq 0.008m$	A_{coil}	$25mm^2 \leq A_{coil}$
L_c	$0.008m \leq R_c \leq 0.02m$	L_{piston}	$0.05m \leq L_{piston}$
L_p	$0.003m \leq L_p \leq 0.015m$	B_{max}	$B_{max} \leq 2 \text{ T}$
t_g	$0.0005m \leq t_g \leq 0.0015m$	<i>Dynamic range</i>	$3 \leq \text{Dynamic range}$
W_{op}	$0.003m \leq W_{op} \leq 0.0045m$	$F_{passive}$	$0.9 F_{desired} \leq F_{passive} \leq 1.1 F_{desired}$

Genetic algorithm for optimum design

Numerous optimization algorithms have been proposed including non-derivative methods such as Simplex, Genetic algorithm (GA), and neural networks. These methods have less complexity, but their convergence is not as accurate as more complex methods [19]. GA algorithms are stochastic search optimization methods, in which random number generation in different computational steps is used. The function evaluation methods are not important, since algorithms use function values in search process. GA algorithms are easy to employ, but may require a large computational time to converge [12].

As it was explained in the optimization flowchart, GA starts by assigning random initial values within boundaries that are provided for design variables. Optimization uses FEA simulation to obtain average magnetic field intensity at active area of poles (H_{mr}) for each population. Population is the set of design points at current iteration [12]. For current population, all the constraints are checked. A population can be considered as fit and be used in a parent generation that satisfy all constraints. In the optimization problem under study, due to high number of constraints the number of acceptable

populations are limited. Therefore, population size which is the number of members that a generation should perform GA functions was chosen as low as 10. This number is by default $15 * \text{number of DVs}$. In case the constraints are not met, the selected values are disposed and new values are randomly selected.

A few stopping criteria are defined for GA, including the number of generations, which has the default value of 100. Since obtaining so many feasible generations are out of reach, number of generations are reduced to 20. Function tolerance is another stopping criterion which monitors changes in the value of fitness function. The fitness function represents the relative importance of a design with higher fitness value meaning better design [12]. Depending on what order the fitness function is, an appropriate function tolerance need to be assigned. The default value is $1e - 6$ which was changed to $1e - 4$ to be in the order of magnitude of the fitness function changes. Another stopping criterion is the nonlinear constraint tolerance. Similar to function tolerance, the value of this parameter was changed to $1e - 4$. The smallest tolerance that has an effect in the physical model is 0.1 mm , with anything less than that unnecessary due to computational complexity. Other stopping criteria are time limit, fitness limit, stall generation, and stall time limit, none of which is related to this optimization study and therefore left as default value.

Once enough members of a generation are gathered, GA functions such as mutation and cross over are performed in order to increase the average fitness function of new born generation in comparison to parents. The optimization cycle continues until one of the stopping criteria is met and then the optimized value achieved. A reported shortcoming of GA is that the result is not guaranteed to be the global optimum [12].

Results analysis

An initial point is selected for the optimization procedure. The performance parameters and Comsol simulation results for this initial point are then obtained and compared to optimized values Table 4.6. The optimization found 1450 feasible populations, until the cost function tolerance reached set limits, after which the optimization stopped. Different function values were gathered for each population such as maximum damping force, maximum magnetic field intensity in active region of MR fluid, volume of MR fluid used in the damper, maximum flux density in the magnetic

circuit and MR fluid, and weight of the whole damper. Table 4.6 exhibits the results and performance indexes. Figure 4.14 displays the flux density distributions for the initial design and consequently for the optimal design. Effect of the optimal design on each criteria is investigated here:

Magnetic field intensity and magnetic flux density: Based on equation 4.7, one of the main factors that can increase shear stress and consequently increase the damping force is to enlarge the poles active area while avoiding magnetic saturation. The length of the core was increased to prevent magnetic saturation, i.e., 1.8 T in iron and 1.6 T in MR fluid. Table 4.6 shows that an increase in H_{mr}, B_{mr}, B_{iron} with the maximum flux density restricted to below saturation levels.

Table 4.6 Optimization results for design variables and main properties.

Design Variables			Characteristics		
Parameter	Initial Value	Optimal Value	Parameter	Initial Value	Optimal Value
R_c	0.008 m	0.0089 m	Max damping force F_{total}	1310 N	1750 N
L_c	0.012 m	0.0145 m	Average B_{mr}	0.559 T	0.849 T
L_p	0.008 m	0.0051 m	Max $B_{total}, Max B_{mr}$	2.11 T, 1.14 T	1.96 T, 1.57 T
t_g	0.001 m	0.0008 m	Dynamic range λ	6	4.6
W_{op}	0.004 m	0.0042 m	Weight M	980 g	785 g
			Max H_{mr}	99 kH	210 kH
			Volume V	215 cc	159 cc

Dynamic range and maximum damping force: It appears that the optimization failed to increase the dynamic range. It should be kept in mind that in problems with so many constraints trade-offs are necessary. The reason for reduction in dynamic range is an increase in the length of the piston core and a reduction in the magnetic poles length. These changes increase the viscous component of damping and decrease the MR effect. However, the maximum damping force has increased more than 30%, which

shows that each component of the damping force has increased individually, even though the ratio is reduced. Figure 4.15 (a), (b) present changes of maximum damping force and dynamic range in different iterations.

Weight and volume of MR fluid: The optimization problem is targeted to reduce the weight. Hence, all attempts were made to reduce the MR fluid volume to reduce weight. As a by-product, the volume of MR fluid is also reduced. Figure 4.15 (a), (b) shows changes in the weight and volume of MR as the optimization procedure progresses. The total weight was reduced by 200 grams in comparison to the initial design, and was reduced 300 grams more than the Lord MR damper.

Other constraint are all satisfied in this design such as the minimum cross sectional area of coil (26 mm^2), dynamic ratio more than 3, and viscose force within 10% of 400 Newton which was set to control the amount of passive force.

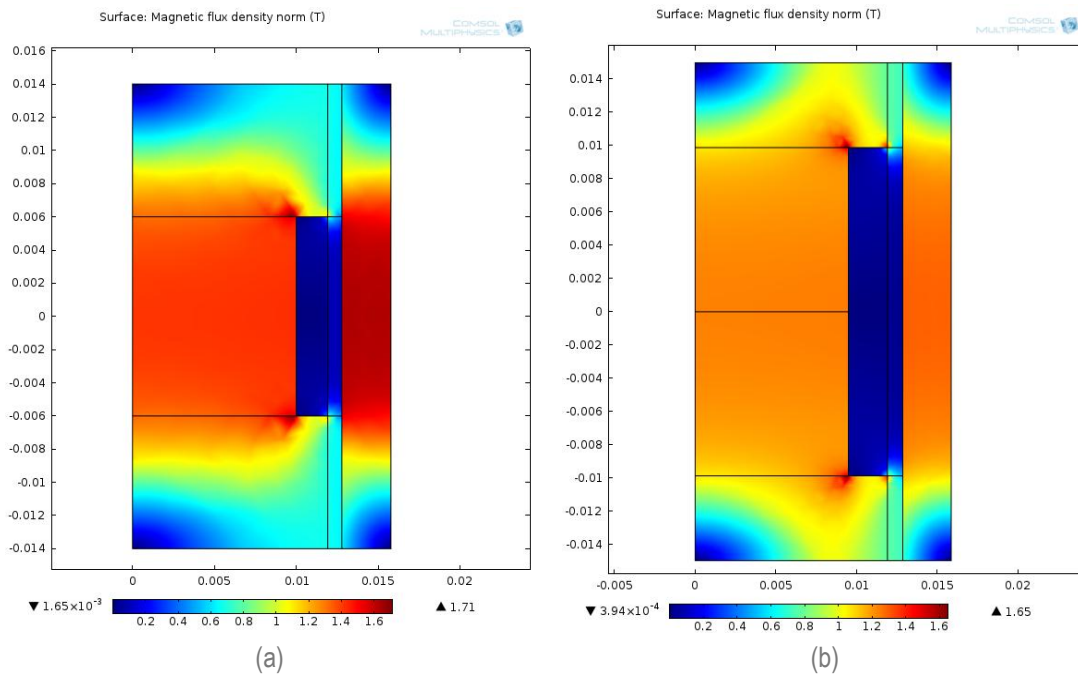


Figure 4.14 (a) Flux density distribution for initial values, (b) Flux density distribution for optimized values.

4.2.5. Coil wire selection

As it was mentioned earlier, cross sectional area of coil A_{coil} in the finite element simulation is highly important. However, there are important performance criteria in MR dampers such as inductive time response and control energy consumption of the valve, which are dependent on the properties of the wire used in the coil. Parameters such as cross sectional area of wire A_w and resistance of coil wire r_w can significantly affect performance in terms of time response.

In order to select an appropriate wire size, a series of standard American wire gauge (AWG) wires were investigated in terms of their time constant and power consumption, by calculation of the number of turns and maximum current that can pass through the wires. Table 4.7 shows wires AWG 24-30 which can be used in this application. All wires are covered with an insulation layer made of materials such as plastic, rubber-like polymers, or varnish. The diameter of wires are provided by manufacturers that can be used to calculate number of possible layers of wire wounds that can be used for given coil width:

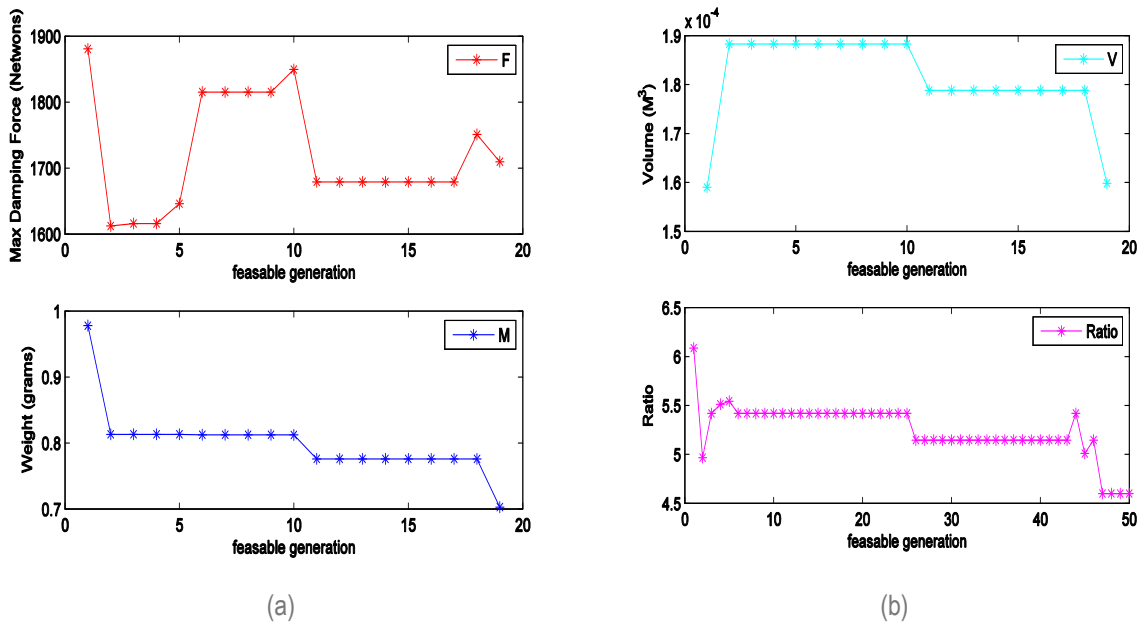


Figure 4.15 (a) The maximum damping force in optimization generations, (a) bottom weight values in different iterations (b) top Volume of MR used in damper in different generations (b) bottom, dynamic ratio in generations.

$$Layers = \frac{w_{coil}}{D_{wi}} \quad 4.16$$

where, w_{coil} is the width of the coil calculated in the optimization process, and D_{wi} is the diameter of wire with insulation. Most importantly, since wire wound starts from one end of the core and needs to be finished at the same side, the number of layers need to be a positive, real, and even number. Therefore, the number is rounded down to the nearest even number. Afterward, by knowing how many layers the coil has, the number of coil turns can be calculated from:

$$N_c = \frac{A_{coil}}{A_w} \quad 4.15$$

where, A_{coil} is the cross sectional area of the coil, and A_w is cross sectional area of wire. The same process as layers need to be applied to make sure wires are physically woundable. The next calculation is the length of wire which is wound around the core for different wire gauges, by adding up length of wire used in wounding each layer:

$$L_w = \sum_{i=0}^{layers-1} ((2\pi R_c + (2j+1)\pi D_{wi}) \frac{L_c}{D_{wi}}) \quad 4.18$$

where, $2\pi R_c$ is the circumference of magnetic core that wire is wounded around, L_c is the length of core, and D_{wi} is the diameter of insulated wire. Resistance of the coil wire which can be described as:

$$R_w = L_w r_w \quad 4.17$$

Resistance of standard wire r_w , and maximum current capacity I_{max} of each wire is provided in wire datasheet, and length was just calculated. Using acquired data, coil power consumption or valve control energy P can be expressed as:

$$P = R_w I_{max}^2 \quad 4.19$$

As mentioned in section 4.2.3, for simulation purposes the number of coil turn was set to 400 with a current of 1 Ampere. Now that we calculated number of turns for each wire size, and maximum current is given, we can simply run the simulation and calculate the average flux density in the middle of the magnetic core. The magnetic flux of the valve, then can be calculated from:

$$\varphi = B_c A_c = B_{mr} A_{mr} = 2\pi R_c B_c = 2\pi R_d B_{mr} \quad 4.20$$

where B_c, A_c are the magnetic core flux density and cross sectional area B_{mr}, A_{mr} are the MR gap flux density and cross sectional area, R_c is the radius of magnetic core and R_d is radius of center of gap. Since B_c is obtained from Comsol simulation, φ can be easily calculated. Inductance of the coil L_{in} can then be computed using all calculated values:

$$L_{in} = \frac{N_c \varphi}{I_{max}} \quad 4.21$$

Finally, inductive time constant of valve T can be calculated using Inductance, and resistance of coil [12], [87]:

$$T = \frac{L_{in}}{R_w} \quad 4.22$$

In order to evaluate performance of different wires, a performance index $N_c I_{max}$ is introduced which presents the inductance of coil per wire. Due to the fast nature of mountain biking, limited supply of energy, and high damping force requirements an optimal wire for mountain bicycle application should have a high inductance, as well as, a small time constant and low power consumption. Therefore a weighted, non-dimensional evaluation criterion is introduced as follows:

$$Eval = w_p \left(\frac{P - P_{avg}}{P_{max} - P_{min}} \right) + w_T \left(\frac{T - T_{avg}}{T_{max} - T_{min}} \right) + w_{IND} \left(\frac{IND_{avg} - IND}{IND_{max} - IND_{min}} \right) \quad 4.23$$

where, $IND = N_c I_{max}$ is maximum ability of coil to induce magnetic field, w_p, w_T, w_{IND} are weight factors related to power consumption, time constant, and maximum ability of coil to induce magnetic field. Since all the above criteria are equally important, all weights are considered to be 1 in calculation. The smaller the number, the better the performance will be. Based on the calculated evaluation factor, an AWG of 25 is the most suitable function implemented in the fabrication.

Table 4.7 AWG wire properties and calculated performance.

	AWG 24	AWG 25	AWG 26	AWG 27	AWG 28	AWG 29	AWG 30
D_{wi} Diameter with insulation(m)	.00054 1	.000483	.000431	.000387	.000347	.000312	.000251
D_{woi} Diameter without insulation(m)	.00051	.000454	.000403	.000360	.000320	.000287	.000254
r_w Resistance of wire(Ω /m)	.0841	.1061	.1338	.1688	.2128	.2684	.3384
I_{max} Max current (A)	3.5	2.7	2.2	1.7	1.4	1.2	.86
Layers of wire	4	4	4	6	6	6	8
N_c Max wire turns	146	204	223	306	342	436	571
L_w Length of wire (m)	5.36	5.88	6.47	11.39	12.44	13.59	21.03
R_w Resistance of coil(Ω)	.449	.622	.869	1.90	2.64	2.88	7.09
P Power consumption (W)	5.50	4.53	4.2	5.50	5.18	4.15	5.24
L_{in} Inductance(H)	.004	.0075	.0096	.0175	.023	.0353	.0631
T Time constant(Sec)	.009	.0121	.0111	.0092	.0087	.0122	.0089
$N_c I_{max}$	511	550.8	490.6	520.2	478.8	523.2	491
Eval	0.0871	0.29845	0.00750	0.01649	0.21160	0.16803	0.14374

4.1. Conclusion

In this chapter the design, simulation, and optimization of magnetic valve components were discussed in full detail. Initially, in section 4.1 a conventional shock absorber by Fox, and a MR damper by Lord Corp, were analyzed and each component was investigated. Study of existing shocks provided us with a better understanding of practical designs and necessary considerations in designing our prototype. Afterward, an optimization index was defined and the materials required were. Furthermore, the magnetic field for MR valve was analysed and a finite element analysis simulation model was developed from existing Lord MR damper. Moreover, an optimal design approach using FEA was utilized. A weighted objective function was introduced to optimise weight, and dynamic damping force range of MR damper. Optimization results for geometrical design were investigated. After obtaining geometrical design, coil area dimensions were used to inspect different wire gauges available.

Chapter 5. Fabrication and testing of a prototype MR damper

In this chapter, the fabrication procedure of MR damper for mountain bicycle application was explained and some of the challenges, limitations, and important considerations in the fabrication process were pointed out. A SolidWorks model was developed base on the optimization results of Chapter 4 section 2. Additionally , the materials for the components were selected and components were fabricated and assembled. Also, a series of experiments were performed on the prototype model to evaluate the performance. The details of the prototyping and testing are presented in the following sections.

5.1. Materials, sealing, CAD design, and prototyping

The prototyping began by using the result of the optimization process in chapter 4 section 2. One point that we did not considered was that we used Metric units in the optimization while for fabrication in machine shops the preference is in Imperial units. That imposed some modifications and changes in the design and dimensions. The property of the material was identified form the optimization however the real challenge was to find exact materials as suggested by the simulation. For the Aluminum parts, one important consideration was anodization of the surfaces that were in contact with MR fluid to avoid wear and corrosion. Table 5.1 shows the list of the materials used in the prototype, and their relative sizes. Figure 5.1 displays a detailed sectional view of the proposed MR damper and the bill of material was also included. More CAD designs were provided in Appendix B.

Cylinder: As it was mentioned in chapter 4, the size of the cylinder of damper was fixed during optimization. For this application, three diameter sizes of aluminum tubes, with outer diameters of $1\frac{3}{4}$, $1\frac{1}{2}$, $1\frac{1}{4}$ (Inch) and wall thickness of $\frac{1}{8}$ (Inch), were

Table 5.1 List of components utilized in prototype.

COMPONENT	MATERIAL	SIZE	VALUE
Cylinder	Aluminum 7075 tube	Outer diameter	1-1/2 [in], 38.10 [mm]
		Wall thickness	1/8 [in], 6.35 [mm]
Cylinder caps	Aluminum 7075 bar	Diameter	1-1/2 [in], 38.10 [mm]
Shaft	Aluminum 7075 rod	Diameter	3/8 [in], 9.525 [mm]
Magnetic core , poles, outer piston	AISI 1018 mild carbon steel bar	Diameter	1-1/2 [in], 38.10 [mm]
Bushing	Steel	Inner diameter	3/8 [in], 9.525 [mm]
H-wiper	PTFE	Inner diameter	3/8 [in], 9.525 [mm]
O-Ring	PTFE	Outer diameter	1-7/16[in], 36.51[mm]
Quad-ring	PTFE	Outer diameter	1-1/2 [in], 38.10 [mm]
Wear strip	Teflon	Outer diameter	1-1/2 [in], 38.10 [mm]

considered and optimization was performed for all. Results showed that the smallest size cannot satisfy the dynamic force range, and largest size increases weight of the

damper significantly, therefore medium size was selected. For the material of cylinder, shaft, and the caps, Aluminum 7075 alloy is chosen because of its high strength, i.e. close to steel, as well as high machinability, and light weight (the density is very close to other aluminum alloys). The cylinder was threaded inside from both sides, and the caps were threads on their circumferences to close the cylinder. To ensure there will be no leak PTFE O-ring is placed between the caps and cylinder. A challenging part there was to peak the right tolerances for the O-rings. Fabricated cylinder is displayed in Figure 5.2 (a).

Shaft and rod-end cylinder cap: the shaft was cut from an anodized rod of the same aluminum alloy as the cylinder. A through hole was drilled in the shaft to pass the wires. As it can be seen in the CAD model of Figure 5.1 the shaft hole was threaded so it can be fastened to the piston to hold it in place as well as the piston guide. Rod-end

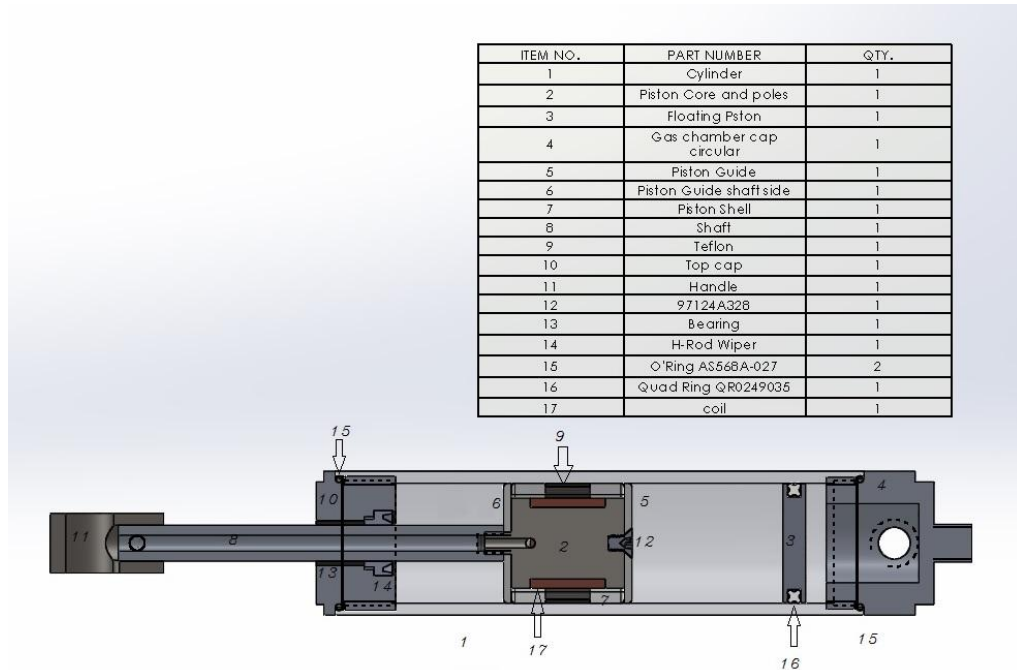


Figure 5.1 Detailed SolidWorks CAD design of proposed damper.

cylinder cap was sealed using a combination of rod wiper and bushing. A PTFE H-type rod wiper, i.e. similar to two U-cops was used to prevent leakage and stop dust penetrating inside the damper. Also a linear self-lubricating shaft bushing is utilized to align the inner piston with the outer body and prevent any lateral movements. The shaft and piston can slide along shaft axis. Figure 5.2 (b) displays the rod-end cylinder cap with the H-wiper, and the bushing.



Figure 5.2 Prototype (a) Cylinder and caps (b) Rod-end cylinder cap.

Gas chamber cylinder cap and floating piston: As it was mentioned before, a floating piston was separating MR fluid from air inside the air chamber. This design was different from the Lord MR damper since a high pressure valve was placed at the cap to enable us to adjust the pressure of the gas chamber. The adjustable air chamber is common in high end conventional mountain bike dampers to give rider higher spring force if desired. It should be noted that we used pipe threads, since they provide good seal for high pressure pneumatic applications. The floating piston was also made of same aluminum alloy as the cylinder. Also, we used a quad-ring which was a seal used for sliding application, for the floating piston to prevent MR fluid from entering gas chamber. Floating piston was one of the most tolerance sensitive parts in my design, because if the ring slot was not perfectly fitting with the quad-ring it can either cause leakage, or lots of friction. Figure 5.3 (a), (b) were showing gas chamber cap, and floating piston.

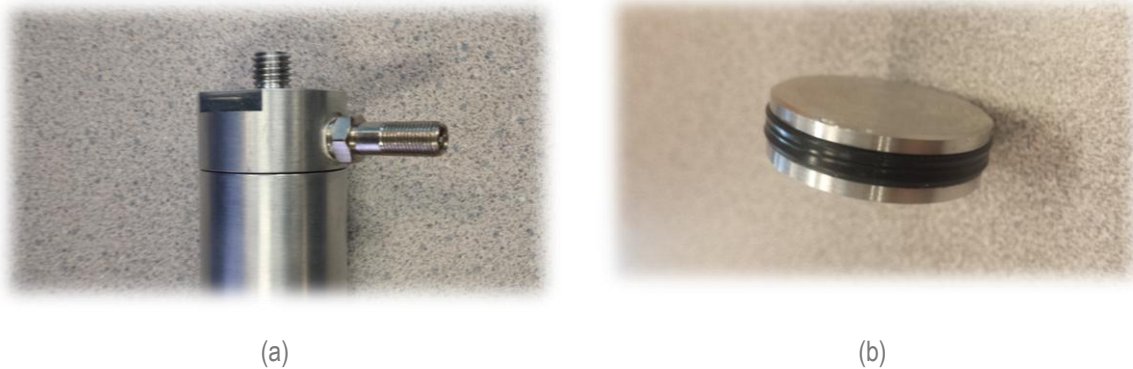


Figure 5.3 Prototype (a) Gas chamber-end cylinder cap with high pressure valve (b) Floating piston.

Piston and coil: the piston in Figure 5.4 (a) was consists of a bobbin shape magnetic body, which was consist of a magnetic core with the poles attached to each other. The coil was wounded around the core. It also included a cylindrical piston housing, with an outer diameter very close to the inside diameter of cylinder to prevent the fluid pass between them. Two piston guides were placed, to keep the MR fluid flow gap constant at all times, and moving the inner piston and outer piston together. Figure 5.4 (b), depicts the top view of the piston which shows cross-shaped piston guide, attaching inner piston to outer piston. One of the piston guides was attached to the core

using a 4 [mm] long aluminum screw with M4 threads, while the other piston guide is fastened between rod and pole. A slot was machined on piston to accommodate the wear strip which is a Teflon seal that prevents the MR fluid leak between the cylinder and the outer piston. Wear strip needs to be closely fit to minimize friction, while preventing the wear of the cylinder. Another design consideration was where to place coil winding wires that need to be connected to power source. Wires can get damaged in contact with MR fluid. To pass the wire, as illustrated in Figure 5.6, couple of small holes were made perpendicular to each other, one to the hollow shaft, and the other to get wire to the surface of the core. Hollow threaded tip attached to pole was used to attach the piston to the rod and guide the wire through the shaft.

As it was recommend by the optimization, two hundred turns of wire was wounded around core using AWG 25 coil wire. A layer of insulation was used to prevent short circuit due to potential wire damages. Also, a layer of insulation was used to prevent the wire to be exposed to MR fluid. Figure 5.4 (a) displays the wounded coil.

Figure 5.5 (a), (b) illustrate assembled prototyped MR damper. The weight of damper without MR fluid was 500 grams. Approximately 150 g MR fluid was used to fill the damper and the final weight of the Damper is measured at 650 grams. Considering this as the first prototype, a 30% weight reduction in comparison to Lord MR damper was achieved, only by material modification and design optimization, which is satisfactory.



Figure 5.4 Prototype (a) wounded coil (b) Assembled piston.



Figure 5.5 Prototype MR damper (a) Assembled part without cylinder (b) Assembled MR damper.

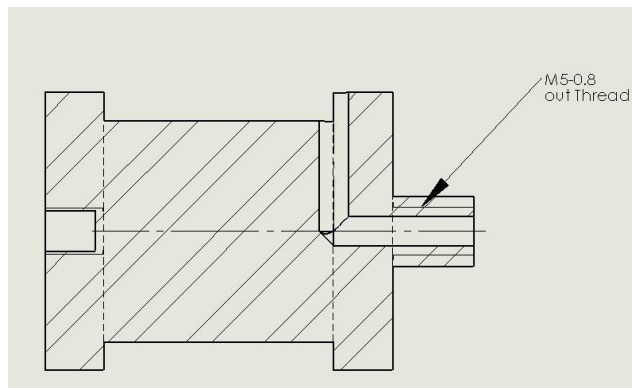


Figure 5.6 Magnetic core and poles design.

5.2. Experimental performance testing

In order to evaluate the performance of prototype MR damper same test mechanism was utilized. The input was sinusoidal displacement applied to the shaft and the damping force was measured using force transducer. Similar to previous tests, different input frequencies, amplitudes, and currents were applied to the MR damper. Various comparisons were performed to show the performance of developed prototype.

5.2.1. Effect of displacement amplitude

Increasing of the amplitude of input displacement resulted in increasing the damping force as expected. Figure 5.7 shows three different amplitudes of input displacement. Since the results are for input current zero, effect of gas chamber forces were totally noticeable in rebound circuit of force vs. velocity graphs.

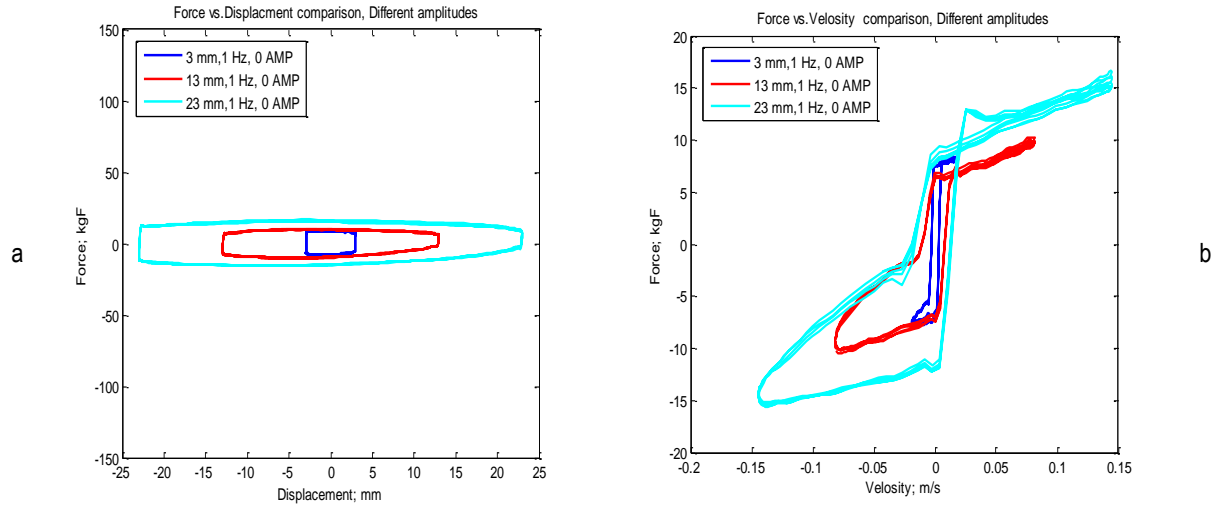


Figure 5.7 Amplitude change effect for prototype MR damper (a) FD curves (b) FV curves.

5.2.2. Effect of displacement frequency

Tests was done for frequencies of 1 Hz and 6 Hz. A major change in the amount of damping force was observed between these frequencies. Since input current is zero, the forces are passive and highly sensitive to change in velocity of piston head movement.

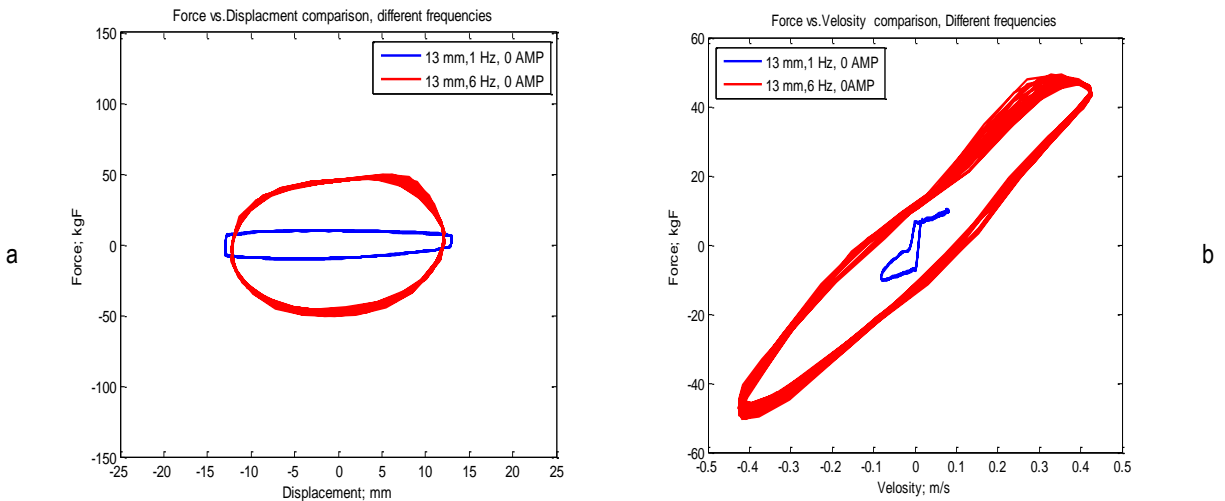


Figure 5.8 Frequency effect for prototype MR damper (a) FD curves (b) FV curves.

5.2.3. Effect of input current

Input current had a significant effect on variations in amount of damping force. Since the objective was to have low passive forces and high dynamic range of forces, the amount of MR related force is relatively high. Figure 5.9 shows the effect of input current on damping force. As mentioned earlier, an increase in the input current may cause saturation. When a 3 Amp input current was applied to MR damper, as shown in black curve, the amount of damping force did not change respectively, showing that magnetic valve have reached saturation.

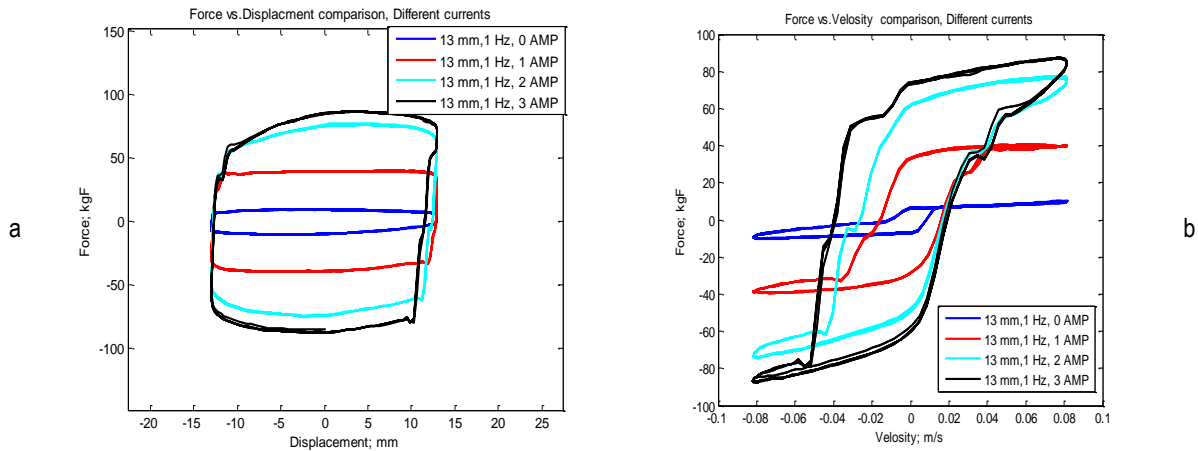


Figure 5.9 Input current effect for prototype MR damper (a) FD curves (b) FV curves.

5.2.4. Comparison of parallel plate model and experimental data

As mentioned in chapter 4, parallel plate quasi-static model was used to predict behavior of MR damper. Model is an approximation and is neglects some forces such as friction. Also, model is not considering effect of high velocities on performance of damper. Therefore, results of predicted model and experimental data can vary in high velocities. Figure 5.11 (a) compared maximum damping force for each input current at low piston velocity of $0.018 [m/s]$. Differences between two results are relatively small, 11% tolerance, which was mainly due to negligence of friction. Hence, in high velocity of $0.867 [m/s]$, proposed model failed to predict the experimental results. Figure 5.11 (b) displayed difference between predicted model and experimental data.

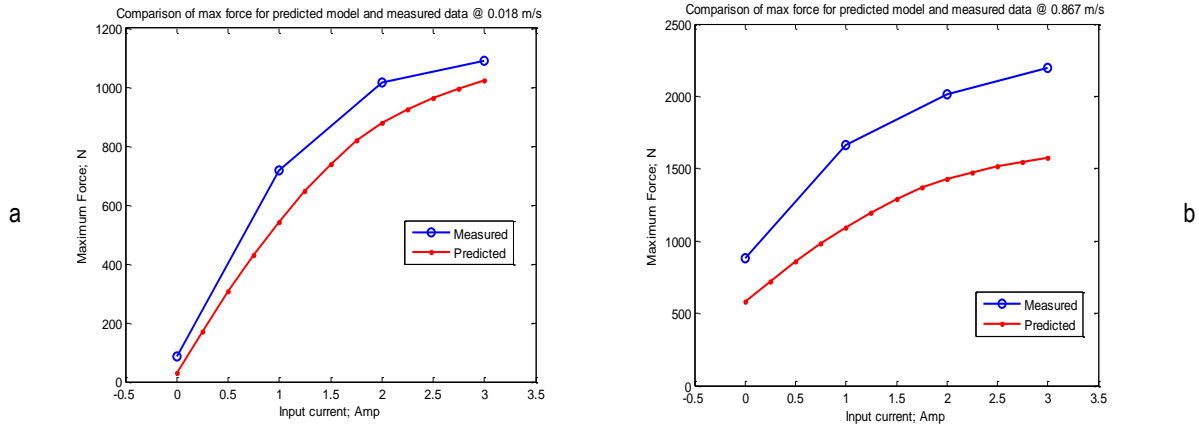


Figure 5.10 Comparison of max damping force for predicted model and experimental data (a) low velocity @ 0.018 (m/s) (b) high velocity @ 0.867 (m/s).

5.2.5. Comparison of Lord MR damper and prototype MR damper

A comparison of performances of Lord MR damper and fabricated MR damper was needed to evaluate the validation of design. Figure 5.11 (a), (b) were plotted to compare passive forces of two dampers. As it can be observed, passive force of prototype is less than MR damper, as designed. Figure 5.11 (c), (d) showed total damping forces of dampers at same power consumption level. Worth mentioning that since wires used in coil winding of two dampers had different internal resistance, input current was not a suitable criterion to compare. Although Lord Mr damper showed higher damping force for same power consumption, but main objectives of prototype design were dynamic range and weight. Both objectives were achieved with this design. Table 5.2 displays a comparison between dampers to illustrate shortcoming of prototype damper to achieve maximum force. Weight and diameter of damper had decreased, which directly affected damping force.

Table 5.2 Parameter comparison of Lord MR damper and prototype.

Material	Passive Force (N)	Max damping force @ 1 Hz 13 mm (N)	Weight (g)	Dynamic range
Lord MR 8041	150	1200	900	8
Prototype	100	900	650	9

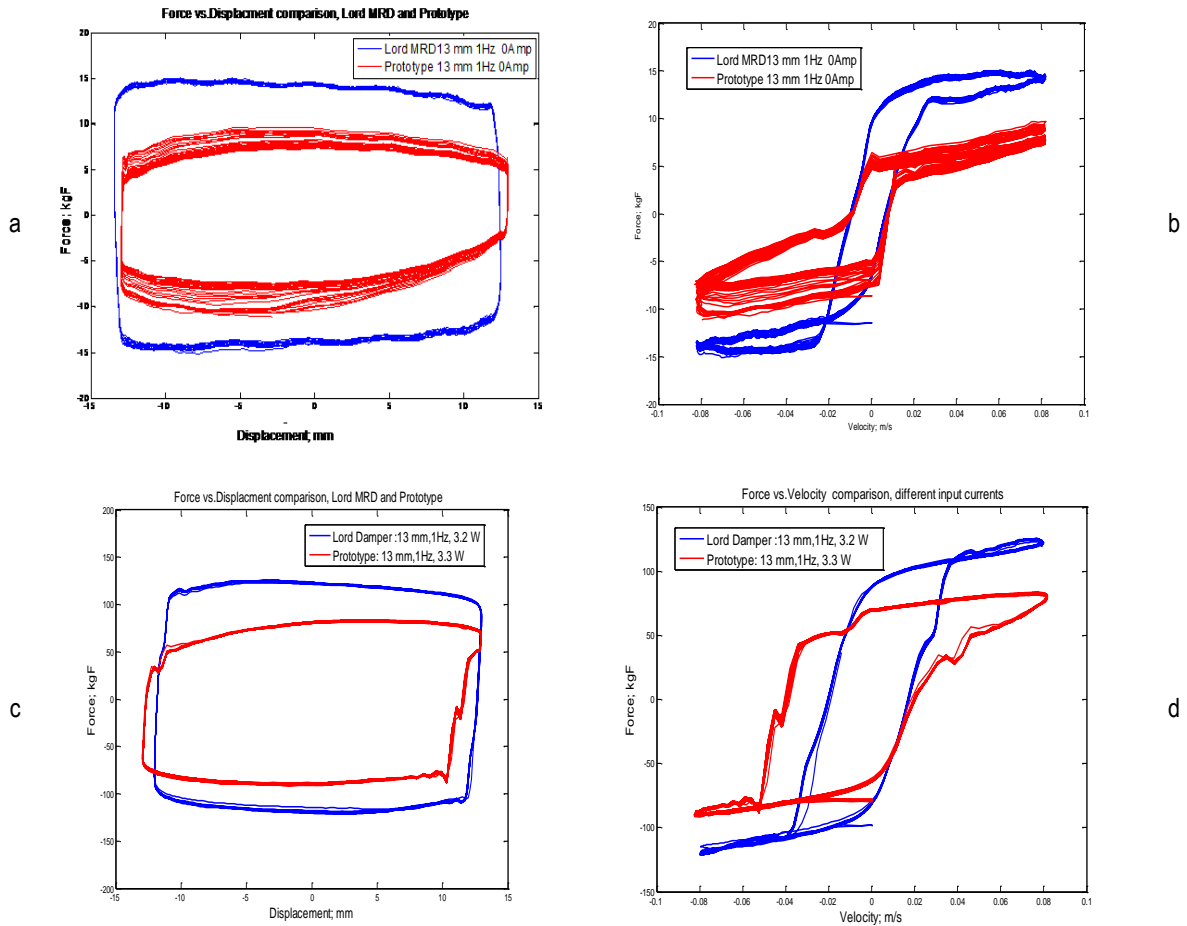


Figure 5.11 Comparison of Lord MR damper and prototype (a) FD curve showing passive force comparison (b) FV curve showing passive force comparison (c) FD curve showing total force comparison (d) FV curve showing total force comparison

5.3. Conclusion

This chapter, presented the MR damper fabrication procedure. Chapter includes material selection for each component based on properties and availability; selection of appropriate seals, in order to prevent fluid leakage and minimize friction. The Solidworks CAD designs with necessary design considerations were also presented in this chapter. Experiments were performed to show performance of the prototyped damper and results were compared with predicted model and the Lord MR damper.

Chapter 6. Summary and future works

The Last chapter of this thesis was dedicated to a summary of this work and to illustrate some of its highlights and contributions to the field. Moreover, some recommendations for future work have been provided.

6.1. Research summery

This work was mainly focused on optimal design and fabrication of a light weight, semi-active, controllable MR damper for mountain bicycle application; considering dynamics of application, behaviour of MR substance, and structure of existing practical dampers for this application. Since, author's work was the beginning of an ongoing collaboration with the industrial partner of the project (Rocky Mountain), the main design criteria was to fabricate a simple and light functional MR damper, which can be easily disassembled to change parts and configurations.

The first part of this study was dedicated to demonstrate the feasibility of the application of MR damper in mountain bicycles. This task was delivered by performing a series of experiments using an existing Lord Corp 8041 MR damper and three conventional mountain bicycle shock absorbers. The performance of those dampers were studied, using force-velocity curves at various input frequencies and amplitudes. A wide range of data was obtained and it was eventually concluded that the MR damper has the capability of producing damping forces similar to conventional dampers.

Next, the dampers were dismantled to better understand the details of internal components design, and assemblies. It was found that conventional shock absorbers utilize a complicated shim stack assembly and adjustable orifices to control passage of oil flow. They also incorporate floating piston and gas chamber, and occasionally an alternative high speed piston to control damping properties. It was concluded that although MR dampers can control damping forces by adjusting input current, some

modification in their valve and orifices" alignments and design is necessary to achieve the same behaviour as high end conventional dampers.

The experimental data and the investigation of components of existing dampers helped us clarified our approach and objectives. Low weight and high dynamic range of damping forces were chosen as main design objectives. Different materials were investigated to substitute existing structural materials. We used high strength aluminum instead of carbon steel in cylinder body, and originally employed MRF 122EG which has less solid content weight percentage in the design. Unfortunately, enough shear stress could not be achieved by using low density MR fluid, therefore, MRF132DG which was a medium density MR fluid was finally implemented.

Furthermore, SolidWorks CAD designs were developed and imported to Comsol Multiphysics for finite element simulations. Since, simulation time and complexity for 3D model was too high, and damper is cylindrical, a 2D axisymmetric model was developed and used in the simulations. ACDC module in Comsol is utilized to perform magnetic studies of the valve. In order to improve the accuracy of the simulations, various considerations were made. Saturation magnetisation of MR fluid and magnetic material were taken into account by using B-H curves of material from datasheets. A multi turn coil with 400 turns and 1 amp current was used as source of magnetic field. The active regions of MR fluid channel, which refers to regions attached to magnetic poles, were selected separate from all areas of channel to calculate more accurate flux density in MR fluid. Finally all outside boundaries are assumed to be isolated magnetically from outside.

The simulation model was linked to MATLAB to conduct optimization using genetic algorithms. A series of optimization assumption and stopping criteria were utilized. MR damper governing formulas; geometrical and performance constraints were selected carefully. An initial point was selected within constraints to start optimization process. An objective function was selected to minimize weight, and maximize dynamic range, with more focus on light design. During each population evaluation, selected sizes within constraint were simulated by obtaining magnetic field intensity and magnetic flux density. The results were returned to optimization tool to evaluate performance

criteria and the process continued until optimization stopping parameters were satisfied and optimal answer was obtained.

Since optimization in finite element was using current density, selection of coil wire could not be investigated. In order to find the most suitable coil wire for this application, available AWG wires were selected and the performance of each case in terms of maximum magnetic field intensity, time constant, and power consumption were evaluated. A non-dimensional objective function was developed for easier evaluation of wires performance. Finally AWG25 was chosen as the best wire for the design.

Finally, detailed SolidWorks CAD designs with the consideration of fabrication standards were generated. Materials, and appropriate seals were obtained. The parts were fabricated and assembled to be tested. Total weight of damper was reduced by 30% in comparison to Lord MR damper. Experiments were performed for various input frequencies, amplitudes, and input currents using same test mechanism that was used before. Results were presented and effect of each criterion was investigated. Furthermore, a comparison between predicted model and experimental data was done and model shortcoming was investigated. Finally results for prototype and Lord MR damper were compared to show that objectives of design were met, although maximum damping force could not be achieved. .

6.2. Recommendations for future work

As mentioned before, this work is the beginning of a long term project. In near future, series of tests will be needed to find experimental data, and compare those results with simulation. Also some modifications will be needed for improving performance of damper since the current configuration may not be able to reach all performance indexes necessary for mountain biking. A few modifications that can be recommended are:

- Since weight is the most sensitive issue in this application, design need to be focused to minimize the volume of MR fluid. This can be achieved by using a combination of gas and MR fluid, or by passing MR fluid from an outside tube. Another approach can be the application of air springs instead of coil spring. The unpopularity of air spring is due to its non-linearity, and thermal dependency. The controllability of MR damper can possibly compensate for those shortcomings.

- Works need to be done to increase shear stress either by increasing active area, utilizing valves with multiple coils, valves with perpendicular coil axis; or by changing annular valves to radial valves.
- Attention has to be given to reduce power consumption by implementation of permanent magnet in magnetic core and poles.

References

- [1] G. F. Breese DG, "Semi-active, fail-safe magneto-rheological fluid dampers for mountain bicycles," *Int. J. Veh. Des.*, vol. 33, no. 1–3, pp. 128–138, 2004.
- [2] A. Ashfak, A. Saheed, K. K. A. Rasheed, and J. A. Jaleel, "Design , Fabrication and Evaluation of MR Damper," *world Acad. Sci.*, vol. 53, pp. 358–363, 2009.
- [3] S. A. Bin Mazlan, "The behaviour of Magnetorheological fluid in squeeze mode," Dublin city university, 2008.
- [4] J. D. J. L. R. Morales-menendez, J. C. Tud, and F.-S. M. H, "Control Strategies for an Automotive Suspension with a MR Damper," 2011.
- [5] B. F. Damgaard, N. C. Bloch, G. W. Svendsen, R. B. Nielsen, J. Morsbol, and J. Kann, "Modelling and Dimensioning the Rear Suspension of a Mountain Bike," Aalborg University, 2009.
- [6] H. Nielens and T. Lejeune, "Bicycle shock absorption systems and energy expended by the cyclist.," *Sports Med.*, vol. 34, no. 2, pp. 71–80, Jan. 2004.
- [7] F. Gordaninejad and S. P. Kelso, "Fail-Safe Magneto-Rheological Fluid Dampers for Off-Highway, High-Payload Vehicles," *J. Intell. Mater. Syst. Struct.*, vol. 11, no. 5, pp. 395–406, May 2000.
- [8] J. Poynor, "Innovative Designs for Magneto-Rheological Dampers," 2001.
- [9] M. Seong, S. Choi, and K. Sung, "Control Strategies for Vehicle Suspension System Featuring Magnetorheological (MR) Damper," 2006.
- [10] D. G. Breesea and F. Gordaninejad, "Semi-active field-controllable magneto-rheological fluid dampers for mountain bicycles," *Smart Mater. Struct.*, vol. 3991, no. 2000, pp. 775–784, 2000.
- [11] D. C. Batterbee and N. D. Sims, "Magnetorheological platform dampers for mountain bikes," *Proc. SPIE*, vol. 7290, p. 72900B–72900B–11, 2009.
- [12] A. Hadadian, "Optimal Design of Magnetorheological Dampers Constrained in a Specific Volume Using Response Surface Method," Concordia University Montreal, Quebec, Canada, 2011.
- [13] N. B. Ekreem, "An investigation of Electromagnetic Rigenerated strong magnetic fields," Dublin City University, 2009.

- [14] K.-G. Sung, Y.-M. Han, and S.-B. Choi, "Geometric Optimization of Controllable Magnetorheological Shock Absorber for Commercial Passenger Vehicle," vol. 6928, p. 69280Q–69280Q–11, Mar. 2008.
- [15] M. R. Jolly, J. W. Bender, J. D. Carlson, and G. Drive, "Properties and Applications of Commercial Magnetorheological Fluids," *SPIE 5th Annu. Int. Symp. Smart Struct. Mater.*, no. 1, 1998.
- [16] a. G. Olabi and a. Grunwald, "Design and application of magneto-rheological fluid," *Mater. Des.*, vol. 28, no. 10, pp. 2658–2664, Jan. 2007.
- [17] a. Grunwald and a. G. Olabi, "Design of magneto-rheological (MR) valve," *Sensors Actuators A Phys.*, vol. 148, no. 1, pp. 211–223, Nov. 2008.
- [18] J. de Vicente, D. J. Klingenberg, and R. Hidalgo-Alvarez, "Magnetorheological fluids: a review," *Soft Matter*, vol. 7, no. 8, p. 3701, 2011.
- [19] Q. Nguyen and S. Choi, "Optimal Design Methodology of Magnetorheological Fluid Based Mechanisms," in *Smart Actuation and Sensing Systems – Recent Advances and Future Challenges design*, 2012, pp. 347–382.
- [20] R. Tao, "Super-strong magnetorheological fluids," *IOPscience*, vol. 979–999, no. 13, p. 979, 2001.
- [21] S. a Mazlan, N. B. Ekreem, and a G. Olabi, "Apparent stress–strain relationships in experimental equipment where magnetorheological fluids operate under compression mode," *J. Phys. D. Appl. Phys.*, vol. 41, no. 9, p. 095002, May 2008.
- [22] M. H. Eltawahni, "Characterization and Finite Element analysis for soft magnetic materials used in automotive applications," Dublin City University, 2006.
- [23] R. M. German, ", Powder Metallurgy Science, Princeton, N. J; Metal Powder Industries Federation," *Powder Metall. Sci. Princeton, N. J*, 1984.
- [24] F. T. Ulaby, *Fundamentals of Applied Electromagnetics*, Fourth edi. Prentice Hall, Upper Saddle River, New Jersey, 1997, p. 407.
- [25] O. D.Paz, "DESIGN AND PERFORMANCE OF ELECTRIC SHOCK ABSORBER," Universidad del Zulia, 2004.
- [26] J. . Kraus, *Electromagnetics*, 4th ed. Singapour, 1991.
- [27] W. D. Callister and J. Wiley, *Materials Science and Engineering*, 7th ed. Utah, Iowa: John Wiley & Sons, 1994, p. Chapter 20.
- [28] J. R. Lloyd, M. O. Hayesmichel, and C. J. Radcliffe, "Internal Organizational Measurement for Control of Magnetorheological Fluid Properties," *J. Fluids Eng.*, vol. 129, no. 4, p. 423, 2007.

- [29] S. Genc and pradeep Phule, "Rheological properties of magnetorheological fluids," *Smart Mater. Struct.*, vol. 140, no. 11, pp. 140–146, 2002.
- [30] F. M. White, *Fluid Mechanics*, 4th ed. University of Rhode Island: WCB McGraw-Hill, pp. 325–381.
- [31] T. C. Papanastasiou, "Flows of Materials with Yield Flows of Materials with Yield," *J. Rheol. (N. Y. N. Y.)*, vol. 385, no. 31, p. 385, 1987.
- [32] A. V. Srinivasan and D. M. McFarland, "Smart Structures: Analysis and Design," *Meas. Sci. Technol.*, vol. 13, no. 9, pp. 76–85, 2002.
- [33] K. D. Weiss and J. D. Carlson, "A growing attraction to magnetic fluid," in *Machine design*, 15th ed., 1994, pp. 61–64.
- [34] G. Bossis, S. Lacis, a Meunier, and O. Volkova, "Magnetorheological fluids," *J. Magn. Magn. Mater.*, vol. 252, pp. 224–228, Nov. 2002.
- [35] Z. Leicht, H. Urreta, a Sanchez, a Agirre, P. Kuzhir, and G. Magnac, "Theoretical and experimental analysis of MR valve," *J. Phys. Conf. Ser.*, vol. 149, p. 012070, Feb. 2009.
- [36] G. a. Dimock, J.-H. Yoo, and N. M. Wereley, "Quasi-Steady Bingham Biplastic Analysis of Electrorheological and Magnetorheological Dampers," *J. Intell. Mater. Syst. Struct.*, vol. 13, no. 9, pp. 549–559, Sep. 2002.
- [37] Q. H. Nguyen, S. B. Choi, and K. S. Kim, "Geometric optimal design of MR damper considering damping force, control energy and time constant," *J. Phys. Conf. Ser.*, vol. 149, p. 012076, Feb. 2009.
- [38] G. R. Burgos and V. Andreas N. Alexandrou, Entov, "On the determination of yield surfaces in Herschel–Bulkley fluids," *J. Rheol. (N. Y. N. Y.)*, vol. 43, p. 463, 1999.
- [39] Q.-H. Nguyen and S.-B. Choi, "Optimal design of a vehicle magnetorheological damper considering the damping force and dynamic range," *Smart Mater. Struct.*, vol. 18, no. 1, p. 015013, Jan. 2009.
- [40] R. . Philips, *Engineering Applications of Fluids with a Variable Yield Stress*. 1969.
- [41] X. Zhu, X. Jing, and L. Cheng, "Optimal design of control valves in magnetorheological fluid dampers using a nondimensional analytical method," *J. Intell. Mater. Syst. Struct.*, vol. 24, no. 1, pp. 108–129, Oct. 2012.
- [42] G. Yang, B. F. Spencer, J. D. Carlson, and M. K. Sain, "Large-scale MR fluid dampers: modeling and dynamic performance considerations," *Eng. Struct.*, vol. 24, no. 3, pp. 309–323, Mar. 2002.
- [43] R. H. Cavey, "Design and Development of a Squeeze-Mode Rheometer for Evaluating Magneto-Rheological Fluids By Design and Development of a

Squeeze-Mode Rheometer for Evaluating Magneto-Rheological Fluids,” Blacksburg, Virginia : USA, 2008.

- [44] a. Farjoud, M. Craft, W. Burke, and M. Ahmadian, “Experimental Investigation of MR Squeeze Mounts,” *J. Intell. Mater. Syst. Struct.*, vol. 22, no. 15, pp. 1645–1652, Oct. 2011.
- [45] A. Farjoud, R. Cavey, M. Ahmadian, and M. Craft, “Magneto-rheological fluid behavior in squeeze mode,” *Smart Mater. Struct.*, vol. 18, no. 9, p. 095001, Sep. 2009.
- [46] S. F. Ali and A. Ramaswamy, “Testing and Modeling of MR Damper and Its Application to SDOF Systems Using Integral Backstepping Technique,” *J. Dyn. Syst. Meas. Control*, vol. 131, no. 2, p. 021009, 2009.
- [47] Y.-J. Nam and M.-K. Park, “Electromagnetic Design of a Magnetorheological Damper,” *J. Intell. Mater. Syst. Struct.*, vol. 20, no. 2, pp. 181–191, Jun. 2008.
- [48] X. Zhu, X. Jing, and L. Cheng, “Magneto-rheological fluid dampers: A review on structure design and analysis,” *J. Intell. Mater. Syst. Struct.*, vol. 23, no. 8, pp. 839–873, Mar. 2012.
- [49] B. Ebrahimi, “Development of Hybrid Electromagnetic Dampers for Vehicle Suspension Systems,” 2009.
- [50] H. . Ly, F. Reitich, M. . Jolly, H. . Banks, and K. Ito, “Simulations of Particle Dynamics in Magnetorheological Fluids,” *J. Comput. Phys.*, vol. 155, no. 1, pp. 160–177, Oct. 1999.
- [51] N. Eslaminasab, “Development of a Semi-active Intelligent Suspension System for Heavy Vehicles,” Waterloo, Canada, 2008.
- [52] S. Sassi, K. Cherif, L. Mezghani, M. Thomas, and A. Kotrane, “An innovative magnetorheological damper for automotive suspension: from design to experimental characterization,” *Smart Mater. Struct.*, vol. 14, no. 4, pp. 811–822, Aug. 2005.
- [53] M. Ahmadian and J. a. Norris, “Experimental analysis of magnetorheological dampers when subjected to impact and shock loading,” *Commun. Nonlinear Sci. Numer. Simul.*, vol. 13, no. 9, pp. 1978–1985, Nov. 2008.
- [54] D. H. Wang, H. X. Ai, and W. H. Liao, “A magnetorheological valve with both annular and radial fluid flow resistance gaps,” *Smart Mater. Struct.*, vol. 18, no. 11, p. 115001, Nov. 2009.
- [55] H. Bose and J. Ehrlich, “Magneto-rheological dampers with various designs of hybrid magnetic circuits,” *J. Intell. Mater. Syst. Struct.*, vol. 23, no. 9, pp. 979–987, Jan. 2012.

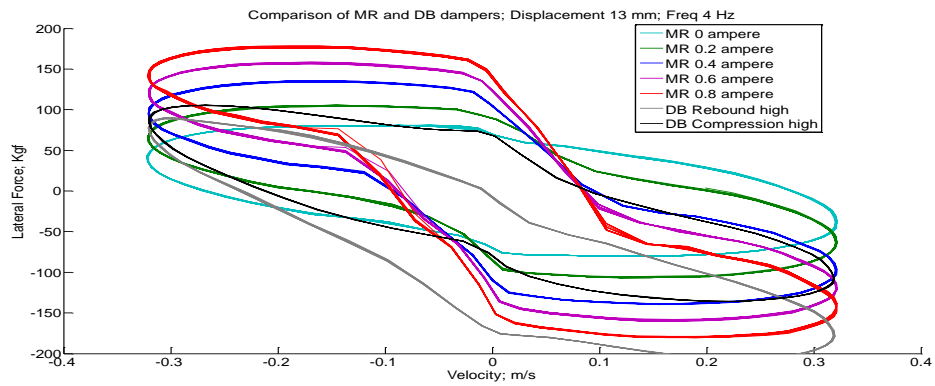
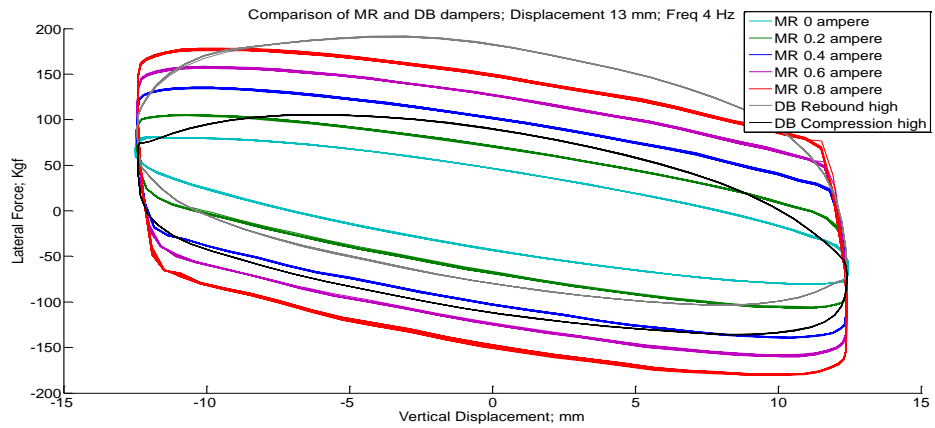
- [56] F. D. Goncalves, "Characterizing the Behavior of Magnetorheological Fluids at High Velocities and High Shear Rates," Blacksburg, Virginia, 2005.
- [57] X. C. Guan, P. F. Guo, and J. P. Ou, "Modeling and Analyzing of Hysteresis Behavior of Magneto Rheological Dampers," *Procedia Eng.*, vol. 14, pp. 2756–2764, Jan. 2011.
- [58] W. W. Chooi and S. O. Oyadiji, "Design, modelling and testing of magnetorheological (MR) dampers using analytical flow solutions," *Comput. Struct.*, vol. 86, no. 3–5, pp. 473–482, Feb. 2008.
- [59] H. X. Ai, D. H. Wang, and W. H. Liao, "Design and Modeling of a Magnetorheological Valve with Both Annular and Radial Flow Paths," *J. Intell. Mater. Syst. Struct.*, vol. 17, no. 4, pp. 327–334, Apr. 2006.
- [60] N. M. Wereley and P. Li, "Nondimensional analysis of semi-active electrorheological and magnetorheological dampers using approximate parallel plate models," *Smart Mater. Struct.*, vol. 7, no. 5, pp. 732–743, Oct. 1998.
- [61] H. H. Zhang, C. R. Liao, M. Yu, and S. L. Huang, "A study of an inner bypass magneto-rheological damper with magnetic bias," *Smart Mater. Struct.*, vol. 16, no. 5, pp. N40–N46, Oct. 2007.
- [62] G. Aydar, "A new magneto-rheological fluid (MRF) washing machine damper and a novel two-way-controllable MRF valve.," University of Nevada, 2007.
- [63] S. M. Savaresi, S. Bittanti, and M. Montiglio, "Identification of semi-physical and black-box non-linear models: the case of MR-dampers for vehicles control," *Automatica*, vol. 41, no. 1, pp. 113–127, Jan. 2005.
- [64] D. H. Wang and W. H. Liao, "Magnetorheological fluid dampers: a review of parametric modelling," *Smart Mater. Struct.*, vol. 20, no. 2, p. 023001, Feb. 2011.
- [65] N. M. Wereley, L. Pang, and G. M. Kamath, "Idealized Hysteresis Modeling of Electrorheological and Magnetorheological Dampers," *J. Intell. Mater. Syst. Struct.*, vol. 9, no. 8, pp. 642–649, Aug. 1998.
- [66] G. M. Kamath, M. K. Hurt, and N. M. Wereley, "Analysis and testing of Bingham plastic behavior in semi-active electrorheological fluid dampers," *Smart Mater. Struct.*, vol. 5, no. 5, pp. 576–590, Oct. 1996.
- [67] H. p. Gavin, "Design method for high-force electrorheological dampers," *Smart Mater. Struct.*, vol. 7, no. 5, pp. 664–673, Oct. 1998.
- [68] X. Wang and F. Gordaninejad, "Flow Analysis of Field-Controllable, Electro- and Magneto-Rheological Fluids Using Herschel-Bulkley Model," *J. Intell. Mater. Syst. Struct.*, vol. 10, no. 8, pp. 601–608, Aug. 1999.

- [69] D.-Y. Lee, Y.-T. Choi, and N. M. Wereley, "Performance Analysis of ER/MR Impact Damper Systems Using Herschel-Bulkley Model," *J. Intell. Mater. Syst. Struct.*, vol. 13, no. 7–8, pp. 525–531, Jul. 2002.
- [70] N. M. Wereley, J. U. Cho, Y. T. Choi, and S. B. Choi, "Magnetorheological dampers in shear mode," *Smart Mater. Struct.*, vol. 17, no. 1, p. 015022, Feb. 2008.
- [71] X. Song, "Modeling Magnetorheological Dampers with Application of Nonparametric Approach," *J. Intell. Mater. Syst. Struct.*, vol. 16, no. 5, pp. 421–432, May 2005.
- [72] H. A. Metered, "MODELLING AND CONTROL OF MAGNETORHEOLOGICAL DAMPERS FOR VEHICLE SUSPENSION SYSTEMS," University of manchester, 2010.
- [73] N. D. Sims and R. Stanway, "Modelling of force–velocity hysteresis in smart fluid dampers," *J. Sound Vib.*, vol. 300, no. 1–2, pp. 429–431, Feb. 2007.
- [74] J. B. F. Spencer, S. J. Dyke, M. K. Sain, and J. D. Carlson, "Phenomenological Model of a Magnetorheological Damper," pp. 1–23, 1996.
- [75] W. H. Li, G. Z. Yao, G. Chen, S. H. Yeo, and F. F. Yap, "Testing and steady state modeling of a linear MR damper under sinusoidal loading," *Smart Mater. Struct.*, vol. 9, no. 1, pp. 95–102, Feb. 2000.
- [76] a. Dominguez, R. Sedaghati, and I. Stiharu, "Modeling and application of MR dampers in semi-adaptive structures," *Comput. Struct.*, vol. 86, no. 3–5, pp. 407–415, Feb. 2008.
- [77] M. K. Sain and B. E. Spencer, "Nonlinear blackbox modeling of MR-dampers for civil structural control," *IEEE Trans. Control Syst. Technol.*, vol. 13, no. 3, pp. 345–355, May 2005.
- [78] R. Stanway, J. L. Sprostonz, and E.-W. A.K, "Applications of electrorheological fluids in vibration control a survey.," *Smart Mater. Struct.*, vol. 5, pp. 464–482, 1996.
- [79] B. Sapinski and J. Filus, "ANALYSIS OF PARAMETRIC MODELS OF MR LINEAR DAMPER Bogdan Sapiński Jacek Filuś," *J. Theor. Appl. Mech.*, vol. 41, no. 2, pp. 215–240, 2003.
- [80] S.-B. Choi, S.-K. Lee, and Y.-P. Park, "a Hysteresis Model for the Field-Dependent Damping Force of a Magnetorheological Damper," *J. Sound Vib.*, vol. 245, no. 2, pp. 375–383, Aug. 2001.
- [81] D. H. Wang and W. H. Liao, "Modeling and control of magnetorheological fluid dampers using neural networks," *Smart Mater. Struct.*, vol. 14, no. 1, pp. 111–126, Feb. 2005.

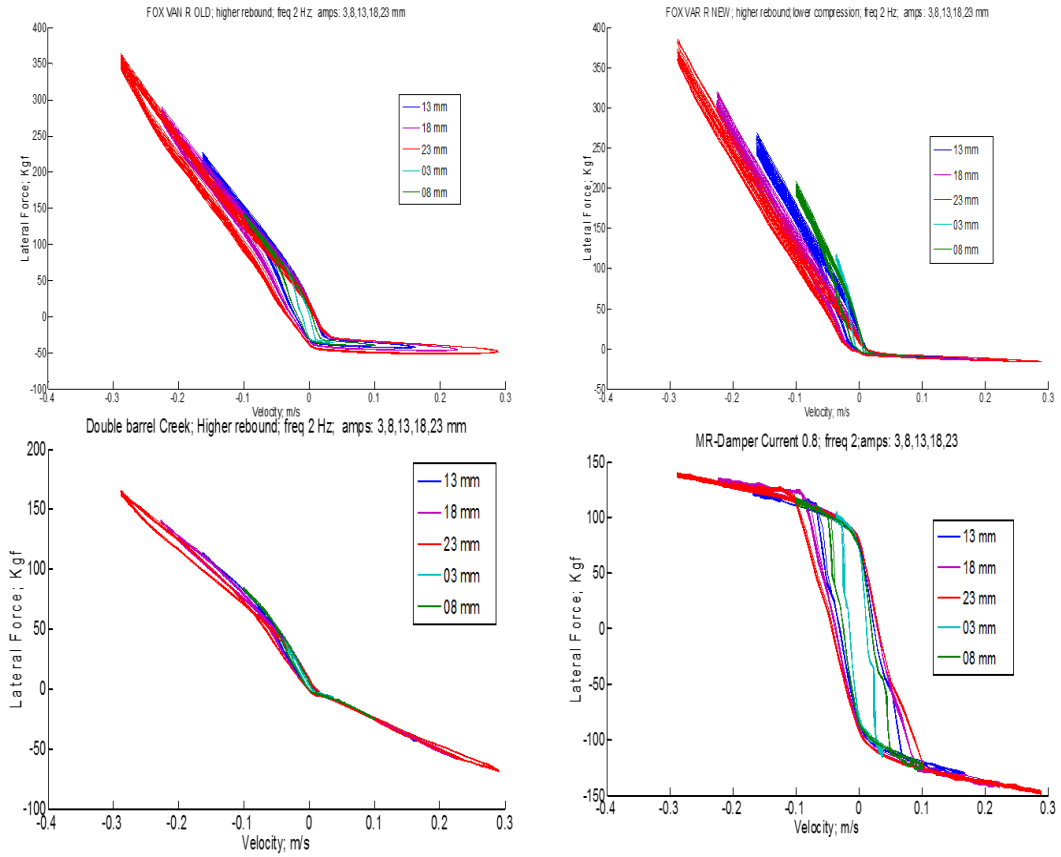
- [82] V. S. Atray and P. N. Roschke, "Neuro-Fuzzy Control of Railcar Vibrations Using Semiactive Dampers," *Comput. Civ. Infrastruct. Eng.*, vol. 19, no. 2, pp. 81–92, Mar. 2004.
- [83] A. Farjoud, M. Ahmadian, M. Craft, and W. Burke, "Nonlinear modeling and experimental characterization of hydraulic dampers: effects of shim stack and orifice parameters on damper performance," *Nonlinear Dyn.*, vol. 67, no. 2, pp. 1437–1456, Jun. 2011.
- [84] J. Morris, "United States Patent [19]," 5,988,3301999.
- [85] J. C. Dixon, *The Shock Absorber Handbook*. Chichester, UK: John Wiley & Sons, Ltd, 2007.
- [86] H. Gavin, J. Hoagg, and M. Dobossy, "OPTIMAL DESIGN OF MR DAMPERS," *U.S.-Japan Work. Smart Struct. Improv. Seism. Perform. Urban Reg.*, no. August, pp. 225–236, 2001.
- [87] Q.-H. Nguyen, S.-B. Choi, and N. M. Wereley, "Optimal design of magnetorheological valves via a finite element method considering control energy and a time constant," *Smart Mater. Struct.*, vol. 17, no. 2, p. 025024, Apr. 2008.
- [88] M. Unsal, "SEMI-ACTIVE VIBRATION CONTROL OF A PARALLEL PLATFORM MECHANISM USING MAGNETORHEOLOGICAL DAMPING," University of florida, 2006.

Appendix A.

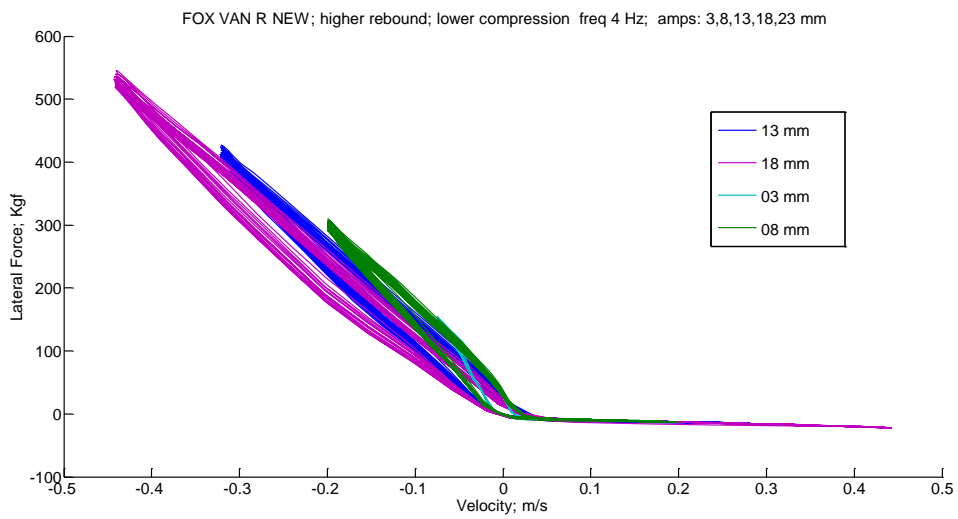
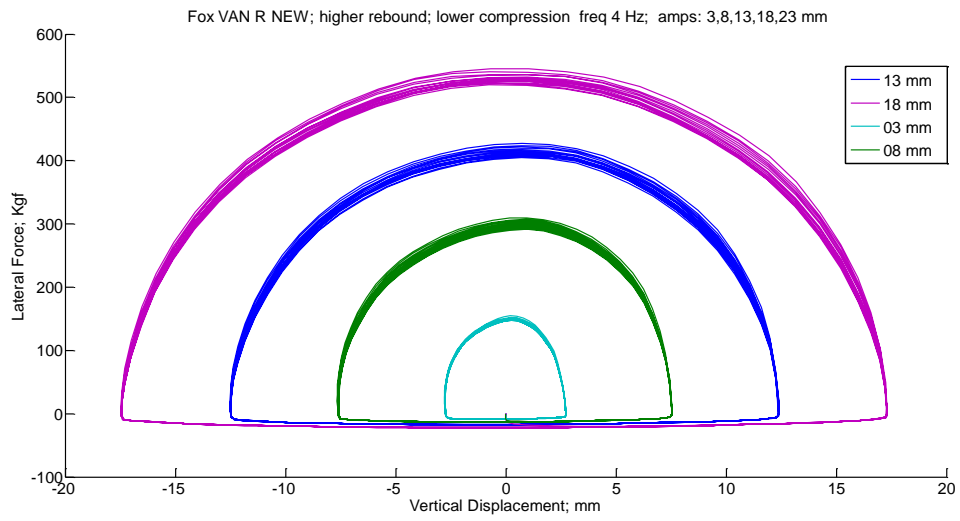
Experimental test results for four tested shocks



Top Force Vs. Displacement, bottom Force Vs. Velocity comparison of MR damper and D3 with spring.



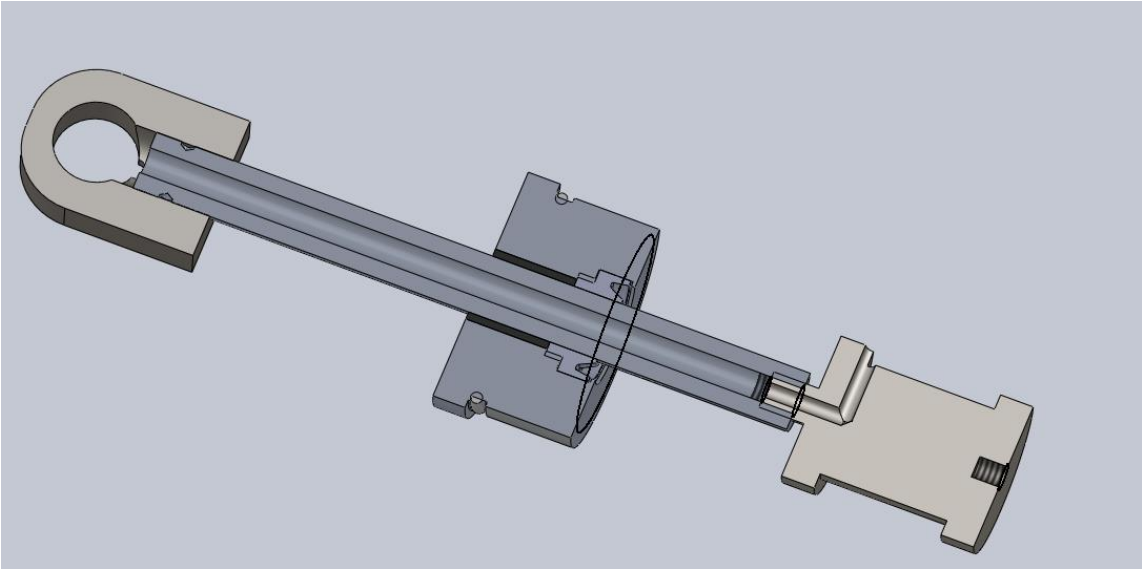
Force Vs. Velocity in High Rebound- Low Compression with 2Hz frequency and all amplitudes (a) top left D1 (b) top right D2 (c) bottom left D3 (d) bottom right MR dam



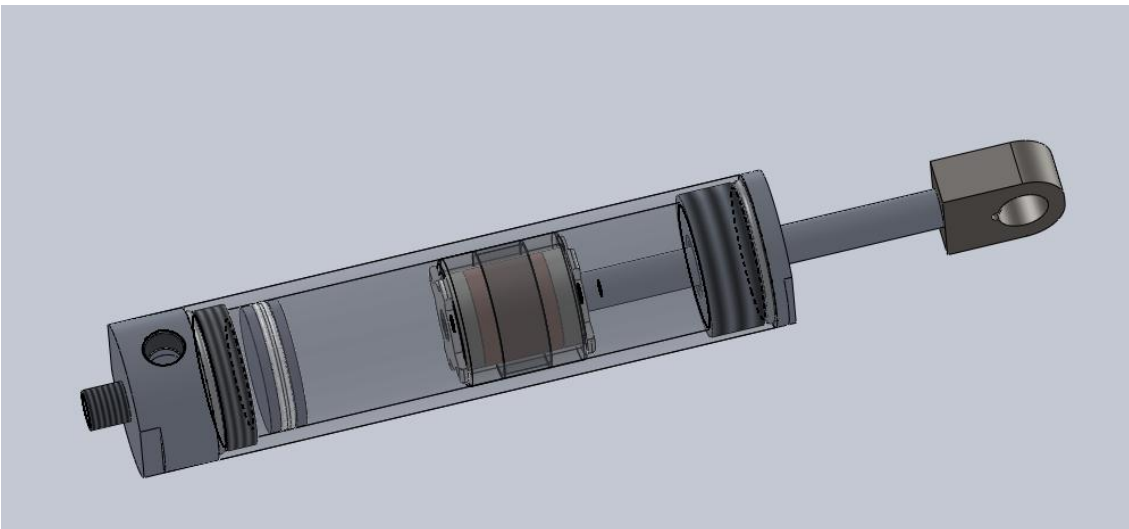
Top Force Vs. Displacement, bottom Force Vs. Velocity in 4Hzfrequency for D2

Appendix B

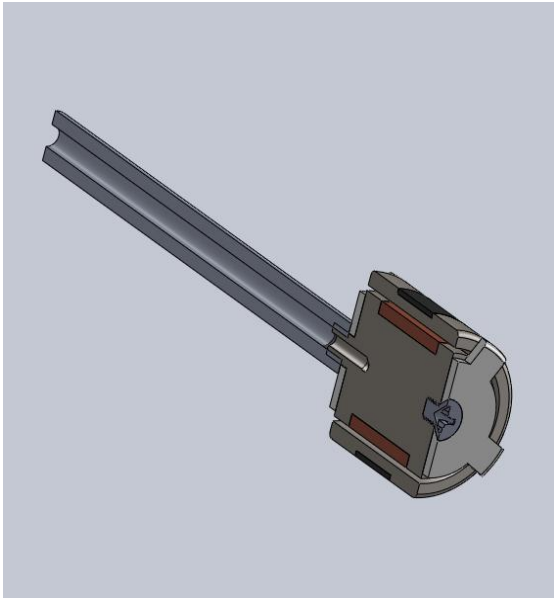
SolidWorks drawings of prototype.



Sectional view of wire passage and rod-end cap sealing



A detailed assembly of finished part

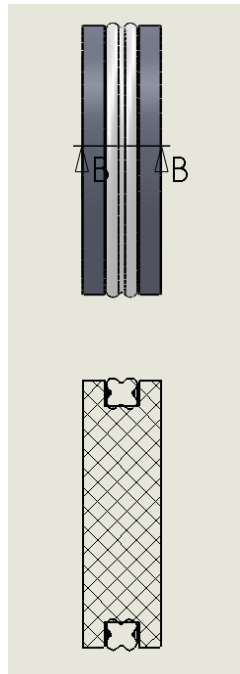


(a)



(b)

Piston and shaft CAD drawing and fabricated prototype



Floating piston and Quad-ring

Appendix C

MRF132DG Datasheet

LORD TECHNICAL DATA

MRF-132DG Magneto-Rheological Fluid

Description

LORD MRF-132DG fluid is a hydrocarbon-based magneto-rheological (MR) fluid formulated for general use in controllable, energy-dissipating applications such as shocks, dampers and brakes.

MRF-132DG fluid is a suspension of micron-sized, magnetizable particles in a carrier fluid. When exposed to a magnetic field, the rheology of MRF-132DG fluid reversibly and instantaneously changes from a free-flowing liquid to a semi-solid with controllable yield strength. Altering the strength of the applied magnetic field precisely and proportionally controls the consistency or yield strength of the fluid.

MRF-132DG fluid can be used in *valve mode* (fluid flowing through an orifice) or in *shear mode* (fluid shearing between two surfaces). In the absence of a magnetic field, MRF-132DG fluid flows freely or allows free movement. Upon application of a magnetic field, the fluid's particles align with the direction of the field in chain-like fashion, thereby restricting the fluid's movement within the gap in proportion to the strength of the magnetic field.

Features and Benefits

Fast Response Time – responds instantly and reversibly to changes in a magnetic field.

Dynamic Yield Strength – provides high yield strength in the presence of a magnetic field and very low yield strength in the absence of a magnetic field; allows for a wide range of controllability.

Temperature Resistant – performs consistently throughout a broad temperature range, meeting the requirements of demanding applications such as automotive shock absorbers.

Hard Settling Resistant – provides high resistance to hard settling; easily redispersed.

Non-Abrasive – formulated to not abrade the devices in which the MR fluid is used.

Application

Mixing – Under common flow conditions, no separation is observed between particles and the carrier fluid. However, a degree of separation may eventually occur under static conditions. If needed, use a paint shaker to redisperse the particles into a homogeneous state prior to use.

Storage

Keep container tightly closed when not in use.

Typical Properties*

Appearance	Dark Gray Liquid
Viscosity, Pa-s @ 40°C (104°F) Calculated as slope 800-1200 sec ⁻¹	0.112 ± 0.02
Density	
g/cm ³	2.95-3.15
(lb/gal)	(24.6-26.3)
Solids Content by Weight, %	80.98
Flash Point, °C (°F)	>150 (>302)
Operating Temperature, °C (°F)	-40 to +130 (-40 to +266)

*Data is typical and not to be used for specification purposes.

LORD
AskUsHow™

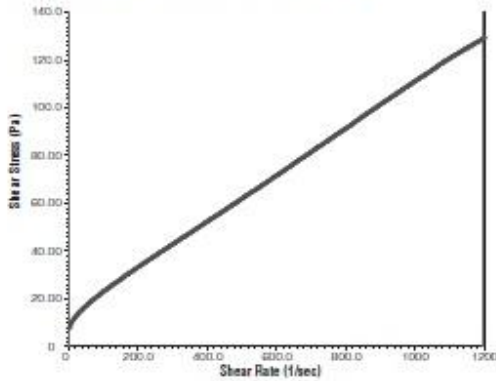
LORD TECHNICAL DATA

Cautionary Information

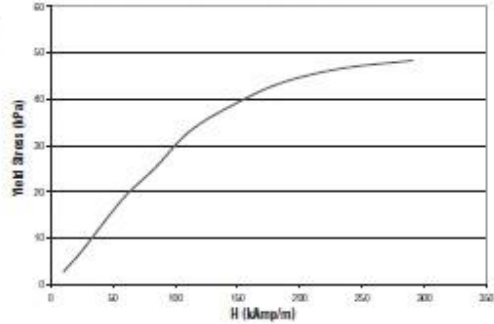
Before using this or any LORD product, refer to the Material Safety Data Sheet (MSDS) and label for safe use and handling instructions.

For industrial/commercial use only. Not to be used in household applications. Not for consumer use.

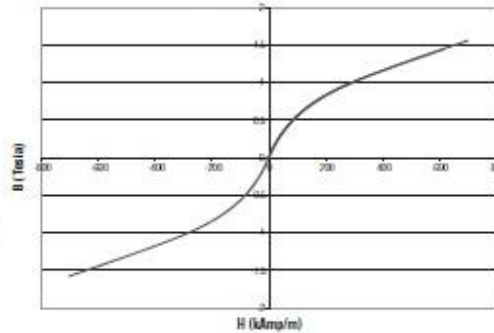
Shear Stress as a function of Shear Rate with no Magnetic Field applied at 40°C (104°F)



Yield Stress vs. Magnetic Field Strength



Typical Magnetic Properties



Values stated in this technical data sheet represent typical values as not all tests are run on each lot of material produced. For formalized product specifications for specific product end uses, contact the Customer Support Center.

Information provided herein is based upon tests believed to be reliable. In as much as LORD Corporation has no control over the manner in which others may use this information, it does not guarantee the results to be obtained. In addition, LORD Corporation does not guarantee the performance of the product or the results obtained from the use of the product or this information where the product has been repackaged by any third party, including but not limited to any product end-user. Nor does the company make any express or implied warranty of merchantability or fitness for a particular purpose concerning the effects or results of such use.

Ask Us How is a trademark of LORD Corporation or one of its subsidiaries.

LORD provides valuable expertise in adhesives and coatings, vibration and motion control, and magnetically responsive technologies. Our people work in collaboration with our customers to help them increase the value of their products. Innovative and responsive in an ever-changing marketplace, we are focused on providing solutions for our customers worldwide ... Ask Us How.

LORD Corporation World Headquarters

111 Lord Drive
Cary, NC 27511-7923
USA

Customer Support Center (In United States & Canada)

+1 877 ASK LORD (275 5673)

www.lord.com

For a listing of our worldwide locations, visit LORD.com.

©2011 LORD Corporation. OD 05/10 (Rev. 2 11/11)

LORD
AskUsHow™